INSTITUTO DE FÍSICA
Universidade Federal Fluminense

An analysis on the one- and two-nucleon transfers induced by ^{16}O in ^{27}Al and ^{28}Si

Caroline da Costa Seabra

Supervisor: Prof. Dr. Roberto Linares

Universidade Federal Fluminense

Niterói-RJ

July 17th, 2023

Ficha catalográfica automática - SDC/BIF
Gerada com informações fornecidas pelo autor

S438a Seabra, Caroline da Costa
An analysis on the one- and two-nucleon transfers induced by 16O in 27Al and 28Si / Caroline da Costa Seabra. - 2023.
95 f.: il.

Orientador: Roberto Linares.
Dissertação (mestrado)-Universidade Federal Fluminense, Instituto de Física, Niterói, 2023.

1. Física Nuclear. 2. Reações Nucleares. 3. Íons pesados. 4. Produção intelectual. I. Linares, Roberto, orientador. II. Universidade Federal Fluminense. Instituto de Física. III. Título.

CDD - XXX

Bibliotecário responsável: Debora do Nascimento - CRB7/6368

INSTITUTO DE FÍSICA
Universidade Federal Fluminense

CURSO DE PÓS-GRADUAÇÃO EM FÍSICA
RUA GAL MILTON TAVARES DE SOUZA, SN
24210-346 – NITERÓI - RIO DE JANEIRO
TEL: (21)2629-5878 - FAX: 2629-5887
E-MAIL: cpg@ if.uff.br

Ata dos trabalhos finais da Comissão Examinadora da dissertação apresentada por **Caroline da Costa Seabra**. No décimo sétimo dia do mês de julho de dois mil e vinte e três, às quatorze horas, reuniram-se remotamente os membros da Comissão Examinadora constituída pelos professores doutores Roberto Linares (IF/UFF), Djalma Rosa Mendes Júnior (IF/UFF) e Leandro Romero Gasques (USP); sob a presidência do primeiro, para prova pública de apresentação da dissertação intitulada ***"An analysis on the two-nucleon transfers induced by ^{16}O in ^{27}Al and ^{28}Si"***, tendo em vista as exigências do Regulamento Específico do curso de Física relacionadas com a conclusão do Mestrado em Física pela Universidade Federal Fluminense. A dissertação foi elaborada sob a orientação do professor Roberto Linares. Após a exposição do trabalho, a aluna respondeu às questões formuladas pelos integrantes da Comissão Examinadora, que apresentou parecer no sentido de aprová-la. Para constar, foi lavrada a presente ata, que vai assinada pelos membros da Comissão Examinadora e pela mestranda.

Niterói, dezessete de julho de dois mil e vinte e três.

Dr. Roberto Linares _____

Dr. Djalma Rosa Mendes Júnior _____

Dr. Leandro Romero Gasques _____

Caroline da Costa Seabra _____

Acknowledgements

I am thankful to my parents Leila and Sergio, who have been supportive of my choice of becoming a researcher even in such hard times for the science in Brazil.

I am deeply grateful to my supervisor, Dr. Roberto Linares, for the dedication, patience and caring for me. Thank you for believing in me in times that I did not myself.

I would like to thank my friends Luiza, Bruna, Sônia, Cauê, Yutao, Marianne, André and my boyfriend Bruno for their love and support during this process. Without them, this journey would not have been completed.

I would also like to thank both the IAEA Marie Sklodowska-Curie Fellowship Program and the Graduation Program in Physics at Institute of Physics in Universidade Federal Fluminense for the financial support during my Master's Program.

I would like to extend my gratitude to all collaborators in this study, in special Dr. Jesus Lubian, Dr. Vinicius Zagatto and Dr. Jonas Ferreira for the theoretical results presented in this work.

Finally, I would like to thank Dr. Djalma Mendes and Dr. Leandro Gasques for accepting to be examiners for this Master's thesis.

The good thing about science is that it's
true whether or not you believe in it.

Neil deGrasse Tyson

Abstract

Transfer reactions are powerful tools to probe single particle configuration as well as correlations of nucleons inside atomic nuclei. Advances in theoretical models and increasing of the computational power have allowed to achieve a good description of transfer reactions induced by heavy ions and to study details in the two-nucleon transfers. In such process, the particles can be transferred in a simultaneous, in which the di-nucleon system is transferred in a single step, and sequential processes, in which the two nucleons are independently transferred. Comparisons between high-quality angular distribution of the experimental cross-sections suggest that the process by which the two particles are transferred depends on the target nucleus, as seen in previous collaborators works [1, 2].

In this work, experimental results for the deuteron pick-up and two-proton pick-up transfer in the ^{16}O+^{28}Si system at $E_{\text{lab.}} = 240$ MeV are presented. The deuteron transfer reaction populates states of the ^{26}Al target-like nucleus, and the two-proton transfer populates states of the ^{26}Mg. In the same experimental campaign we also measured the single particle transfers ^{28}Si(^{16}O,^{17}F)^{27}Al, ^{27}Al(^{16}O,^{17}O)^{26}Al and ^{27}Al(^{16}O,^{17}F)^{26}Mg at the same beam energy. These measurements were performed at the Istituto Nazionale di Fisica Nucleare - Laboratori Nazionali del Sud, Catania, Italy, and analyzed by the MAGNEX spectrometer. Elastic and inelastic scattering were also measured during this experimental campaign, which allowed a good definition of the optical potential parameters for these systems [3]. Angular distributions for the two-proton pickup and both one-proton pickup transfers are presented and compared with Coupled Reactions Channel (CRC) calculations using spectroscopic amplitudes from three different shell-model interactions and single-particle model spaces. The three processes were described within the same methodology. For the processes analyzed in this work, the one-nucleon transfers favor the population of ground-to-ground transfer reactions and contrasts with the results of the two-nucleon transfers, which does not favor the ground state population.

Keywords – Nuclear Physics, Nuclear Reactions, Heavy Ions

Resumo

Reações de transferência são ferramentas poderosas para estudar a configuração de partícula única e as correlações de nucleons dentro do núcleo atômico. Avanços dos modelos teóricos e aumento do poder computacional permitiram alcançar uma boa descrição de reações de transferência induzidas por íons pesados e estudar detalhes da transferência de dois-nucleons. Nesses processos, as partículas podem ser transferidas simultaneamente, onde um sistema di-nucleon é transferido num único passo, e sequencialmente, onde os dois nucleons são transferidos independentemente. Comparações entre distribuições angulares das seções de choque experimentais sugerem que o processo no qual as partículas são transferidas depende do núcleo-alvo, como visto em trabalhos anteriores de colaboradores [1, 2].

Neste trabalho, encontram-se resultados experimentais para a transferência de deuteron e dois-prótons no sistema ^{16}O+^{28}Si com $E_{\text{lab.}} = 240$ MeV. A transferência de deuteron popula estados do núcleo ^{26}Al, enquanto a transferência de dois-prótons popula estados do ^{26}Mg. Na mesma campanha experimental também foram medidas as transferências de partícula única ^{28}Si(^{16}O,^{17}F)^{27}Al, ^{27}Al(^{16}O,^{17}O)^{26}Al e ^{27}Al(^{16}O,^{17}F)^{26}Mg com os mesmos feixe e energia. Essas medidas foram realizadas no Istituto Nazionale di Fisica Nucleare - Laboratori Nazionali del Sud, Catania, Itália, e analisadas pelo espectrômetro MAGNEX. Espalhamentos elásticos e inelásticos também foram medidos nessa campanha experimental, que resultaram numa boa definição dos parâmetros do potencial óptico para esses sistemas [3]. Resultados para as distribuições angulares das seções de choque da transferência de dois-prótons e de ambas transferências de um-próton são apresentados e comparados com cálculos de CRC (Coupled Reactions Channel, em inglês) usando amplitudes espectroscópicas de três modelos diferentes para a interação no modelo de camadas e modelos espaciais de partícula única. Os três processos foram descritos utilizando a mesma metodologia. Para os processos estudados nesse trabalho, a transferência de um-nucleon favorece a população das transferências de estado fundamental para estado fundamental e contrasta com os resultados da transferência de dois-nucleons, que não favorece a população do estado fundamental.

Palavras-chave – Física Nuclear, Reações Nucleares, Íons pesados

Contents

List of Figures

List of Tables

1 Introduction and motivation

The atomic nucleus is a complex system of highly interacting particles in a tiny volume and the balance between protons and neutrons (usually referred as nucleons) is crucial to the nuclear stability. As a matter of fact, about 300 atomic nuclei are stable whereas more than 3000 are unstable nuclei [4], that most of these unstable nuclei have half-life shorter than 1μs. In this context, the nucleon-nucleon interaction is a key ingredient to understand the nuclear stability and the processes by which unstable nuclei spontaneously decay.

From the quantum mechanical standpoint, the atomic nucleus is a challenging system in which pertubative approaches, that successfully apply to atomic and molecular entities, do not hold. Starting with the most fundamental perspective, currently the best description of the particles and the interactions between them is described by quantum chromodynamics (QCD). Its fundamental degrees of freedom are quarks (matter fields) and gluons (force carriers). Quarks appears in six flavors but the ordinary matter (protons and neutrons) are composed by two light quarks: *up* and *down*. The resulting nuclear forces that are responsible for the nuclear binding are residual forces, much like the van der Waals forces between neutral molecules [5]. However, a quantitative connection between nuclear force and quark-quark interaction is still a topic of investigation due to the intrinsic difficulty of carrying out QCD calculations at the low energies, where nuclear physics lies.

To describe the complexity of the theoretical description of the nuclear forces, it is instructive to discuss the scales arising in this type of problem. The phenomenological potential between two nucleons consist of a highly repulsive, at distances shorter than ≈ 0.4 fm, followed by an attractive range. For what follows in this dissertation, we are not probing the nuclear interactions at such distances.

Properties of deuteron, the simplest bound nucleus, and the *pp* and *pn* scattering data provide substantial information about the nuclear forces at the level of nucleon-nucleon interaction. Currently we understand that it is:

- a spin dependent, meaning that its strength depends on the $S = 0$ (*singlet*) and $S = 1$ (*triplet*);

- has a tensor term (noncentral component), meaning that the ground-state wavefunction of deuteron is a combination of S- and D-waves;
- nearly charge independent, meaning that the interaction between pp, pn and nn are almost the same.

In the 90s, high-precision potentials have been developed to fit a large amount of *pp* and *pn* elastic scattering data, such as the charge-dependent Bonn nucleon-nucleon potential [6] and the Argonne V18 potential [7]. While these potentials give accurate description of most deuteron properties, the simplest bound nucleus, the situation becomes less satisfactory when it comes to heavier systems, when the typically small three-nucleon forces become necessary to describe the nuclear binding and energy levels. A three-nucleon force is one which is felt only when there are at least three particles present, such as triton or a ^{3}He.

1.1 Towards effective approaches: the mean field

The preceding paragraphs give a brief overview on the theoretical challenges on the way to describe properties of the atomic nucleus. In this context, the effective field theory (EFT) is a general approach to calculate low-energy properties of physical systems by exploiting relevant energy scales in it [8]. Usually requires high performance computers and refined algorithms to include not only the leading order but also the next-to-leading order and, eventually, next-to-next-to-leading order. Mean-field theories, on the other hand, provide a basic tool to study nuclear structure in which the interactions between nucleons, that constitute a given nucleus, are replaced by the interaction of each nucleon with a mean field. In other words, it is an independent-particle approximation with a mean field that represents the average nucleon-nucleon interactions.

The concept of mean field is very important to nuclear physics, as it provides grounds to understand the appearance of shell structures in nuclei. The shell structure is clear in atoms, since electrons move in the central Coulomb field of a small but massive charged nucleus, and the earlier evidences of the shell structure were shown in [9]. In the nucleus itself, where the central field is self generated by the nucleons, it came as a big surprise. Interpretation of experimental data in shells was strongly contested at the beginning. An important feature of nuclear shell structure is provided by the separation energies. For

instance, one-neutron separation energy (S_n) of a nucleus with atomic mass A and atomic number Z is defined as:

$$S_n(A, Z) = B(A, Z) - B(A-1, Z) \tag{1.1}$$

where $B(A, Z)$ and $B(A-1, Z)$ are the binding energies of the nucleus with atomic mass A and $A-1$, respectively. A systematic analysis of the one-neutron separation energies for isotopes shows that more energy is required to remove one neutron when the number of neutrons is initially even. The effect on the nuclear radii as the subshells are filled and the energy level discrepancy of the first 2^+ excited state in even-even nuclei are other examples of nuclear properties that points towards nuclear shells, specially when comparing these characteristics with its neighboring nuclei. More information on this topic can be found in Section 5.1 of [10].

The shell structure in nuclei suggests that the nuclear Hamiltonian, that describe the nucleons and their interactions, contains a dominant independent-particle component. The solution of the time-independent Schrödinger equation for this "pure" independent-particle Hamiltonian gives the single-particle states. In this "pure" version of the nuclear Hamiltonian, the single-particle states are either occupied or empty. This simple scheme gives a quite reasonable prediction for the J^π of the low-lying states in many even-odd nuclei, such as the ^{17}O, for which the ground state $5/2^+$ is interpreted as a valence neutron interacting with the nuclear core. In some case, one must add a residual interaction to the independent-particle Hamiltonian to improve accuracy of the model. This may result in single-particle states fractionally occupied.

Another important feature of the nuclear field is the pairing interaction. This is the coupling of nucleons in pairs to form states of zero angular momentum, and is responsible for the 0^+ as ground state in all even-even nuclei. The tendency of Fermi particles to form $J = 0$ coupled pairs is well known in solid state, in which the superconductivity in macroscopic systems appears due to pairs of electrons, that are commonly called Copper pairs [11]. In the atomic nuclei, the short-range attractive force between favours this pairing. It must be reminded that Pauli principle do not allow two identical Fermi particles to occupy the same state. In the case of proton-proton and neutron-neutron pairing, that are both spin-1/2 particles, they are constrained to have opposite spin

projections.

The single-particle and nucleon pairs do not cover the intrinsic nature of nuclear states. Some states exhibit properties that are interpreted as collective states. These are states in which the nucleus is portrayed as a droplet of nuclear matter that can vibrate and rotate. The key ingredient are the shape degrees of freedom. This picture is exactly the opposite plot designed by the single-particle approach. However, there is no fundamental incompatibility between these two approaches since the shell model, with the inclusion of residual interactions between nucleons, is, in principle, capable of explaining the nuclear structure.

The most general of nuclear states $|\Psi\rangle$ can be decomposed into a single-particle $|\Psi_{\text{single}}\rangle$, a pairing $|\Psi_{pair}\rangle$, a collective $|\Psi_{\text{col.}}\rangle$ and further components. This can be written as follows:

$$|\Psi\rangle = C_{\text{single}}\,|\Psi_{\text{single}}\rangle + C_{\text{pair}}\,|\Psi_{pair}\rangle + C_{\text{col.}}\,|\Psi_{\text{col.}}\rangle + ... \tag{1.2}$$

where C_x ($x \equiv$ single, pair and col.) are the amplitudes for each component.

1.2 Transfer reactions as a tool to nuclear states

Nuclear reactions are an important source of information of the intrinsic nature of nuclear states. Some reactions allow shedding light to a specific component of the states. For instance, a simple way to identify single-particle states in a nucleus is by means of one-nucleon transfer reactions. A transfer reaction is an interaction between projectile and target nuclei which result in a transfer of nucleons between them. In a pickup transfer reaction, nucleons are removed from the target nucleus and added to the projectile. In the stripping transfer reaction, nucleons are added to the target nucleus.

The one-nucleon pickup and stripping transfer are particularly important to infer the occupation probabilities of single-particle states. Thus, to the extent that the single-particle state is occupied, it can give up a nucleon in a pickup reaction, leaving behind a residual nucleus in a *hole state*. Alternatively, if the single-particle state is empty, it can accept a nucleon in a stripping reaction, creating a residual nucleus in a particle state. This information is usually quantified by spectroscopic factors (SFs) or asymptotic normalization coefficients (ANCs), which are the norm of the overlap function between a

nucleus (A+1) in a state i with a nucleus A in a state f. Measurements of the transfer cross-sections are related to these SFs and ANCs, although the connection between them is not straightforward [12, 13].

In the past, a vast majority of studies were carried out using the (d,p), (p,d), (^{3}He,d) and (d,^{3}He) probes. Reasons for choosing light projectiles are twofold. From the experimental standpoint, measurements of light ejectiles typically attain high energy resolution, good particle identification and a clear distinction between low-lying states of the residual nuclei. From the theoretical standpoint, reaction dynamic is usually treated within the distorted-wave Born approximation (DWBA), which basically assumes that elastic scattering is the most relevant reaction channel and couplings to individual non-elastic channels are weak and not strongly correlated with each other.

Some recent works have addressed the importance of a three-body approach to interpret the (d,p) data [14, 15], and the nonlocality of the nucleon-nucleus interactions [16]. The first point means that the projectile must be explicitly treated as a two-body particle interacting with the target nucleus. The nonlocality of the nucleon-nucleus potential means that a reaction channel (elastic scattering, for instance) can take place at one point $\vec{r}$ and reappear at a further point $\vec{r'}$. In practice, the nonlocal potential can be replaced by a suitable local equivalent potential.

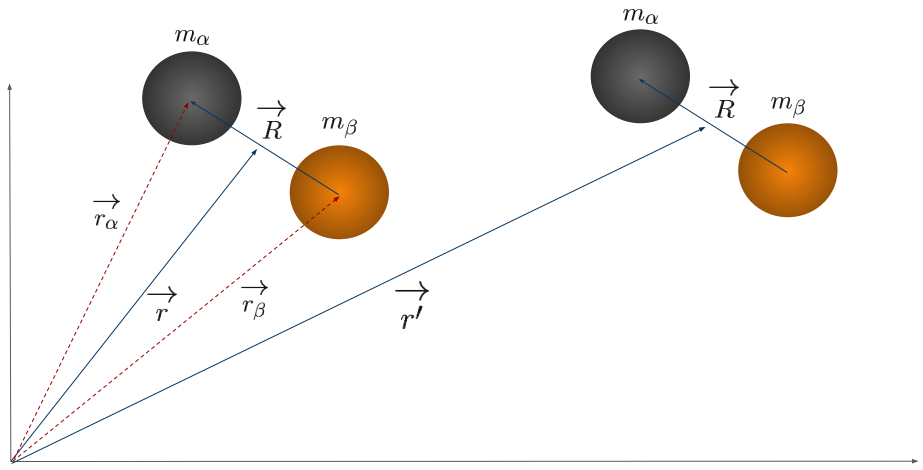

Figure 1.1: Diagram for the nonlocality of the nuclear potential. $\vec{r}$ and $\vec{r'}$ represent the positions in which a reaction channel can occur, in the center of mass frame of reference. $\vec{r_\alpha}$ and $\vec{r_\beta}$ are the positions of the individual nuclei of masses m_α and m_β, and $\vec{R}$ is the relative position between the particles.

When reaction and structure models are in place, a good agreement between experimental and theoretical cross-sections is usually achieved. The ratio of experimental to theoretical cross-sections is usually adopted as experimental estimation for the SFs. It has been shown these estimates, extracted within the adiabatic distorted-wave approximation (ADWA) for the (d, p) reaction in many target nuclei, give a remarkable good agreement with SFs obtained from large-scale shell models [17]. Transfer with the (d, p) reaction is indeed an useful tool for spectroscopic studies of unstable nuclei and Ref. [18] gives a clear overview.

1.3 Motivation for this work

Pairing interaction is of paramount importance to the nuclear structure. Recent works are mostly dedicated to study the structure of neutron-rich exotic nuclei, such as ^{6}He and ^{11}Li [19, 20], whose ground states can partially be interpreted as a dineutron system interacting with a nuclear core. This is also responsible for the existence of the tetraneutron as a resonant state, just recently observed in a knock-out reaction with the ^{8}He. The ^{8}He nucleus has the pronounced cluster structure of an α-core (^{4}He) and four valence neutrons. A sudden removal of the α-particle, in a inverse reaction ^{8}He(p,p^{4}He), give a clear indication of the correlated free four-neutron system [21].

Pairing may also play a role in two-nucleon transfer reactions. This reaction may proceed through two processes:

- sequential transfer: in which the two nucleons are transferred independently and populate states of an intermediary mass partition;
- simultaneous transfer: in which the two nucleons are transferred in one-step, as a single entity.

It has been recognized that two-neutron transfer reactions are sensitive to the pairing correlation [22]. The probability for the simultaneous two-neutron transfer process is enhanced as compared to a naive expectation of sequential transfer process, that is, the square of one-neutron transfer probability [23]. This enhancement has been attributed to the pairing effect, such as the surface localization of a Cooper pair [24].

The (t,p) is the main source of data on the two-neutron transfers. However, use of triton

beams have been strongly limited to match radiation safety procedures in laboratories. On the proton side, the (^{3}He,n) reaction demands measurement of the neutron ejectiles with high intrinsic efficiency and energy resolution. Just for reference, liquid scintillators are often used for neutron detectors and have intrinsic efficiency of about 10% at most.

Transfer induced by heavy ions offers an alternative to the use of light projectiles. Moreover, modern experimental setups have been made possible to achieve good energy resolution and high-quality particle identification for heavy-ions. Most of these setups use large acceptance spectrometers and multiparameter detection systems. Though theoretical calculations involving heavy ions add the challenge of explicitly including non-elastic reaction channels, since its couplings are often strong, nowadays is a feasible task with current computational power.

In recent publications in our research group [25–29], a systematic analysis exploring heavy ions and a consistent reaction models has been done. Optical potential parameters and strengths of the couplings to inelastic channels are constrained using the cross-sections for the elastic and inelastic scattering. Nuclear structure information and SFs are obtained through shell model calculation, assuming explicitly that they are independent of the reaction. It is crucial to consider the limitations of the optical model and coupling schemes when drawing conclusions. Reliable interpretations of reaction mechanisms are obtained through comparison between experimental data and theoretical predictions.

The two-neutron transfer can be studied in the (^{18}O,^{16}O) reaction. The ^{18}O can be interpreted as a two-neutron valence particle bound to a ^{16}O core. The strong selectivity of transfer reaction induced by heavy ions has been observed by M. Cavallaro et al. [1]. In this work, states in the ^{14}C nucleus has been populated by the one-neutron ^{13}C(^{18}O,^{17}O) and the two-neutron ^{12}C(^{18}O,^{16}O) reactions. The experimental excitation energy relative to the ^{14}C ground state is shown in 1.2. It must be noted that the ground state in ^{14}C is suppressed in the two-neutron compared to its intensity in the one-neutron transfer. This is an indication that this is nuclear state has a predominant single-particle nature. On the other hand, the 10.74 MeV state has a strong neutron pairing character, since this state is observed in the two-neutron channel and is negligible in the one-neutron reaction. Calculations also indicate the dominance of the simultaneous process in the two-neutron reaction, despite the typical large angular momenta transfers in nuclear reactions with

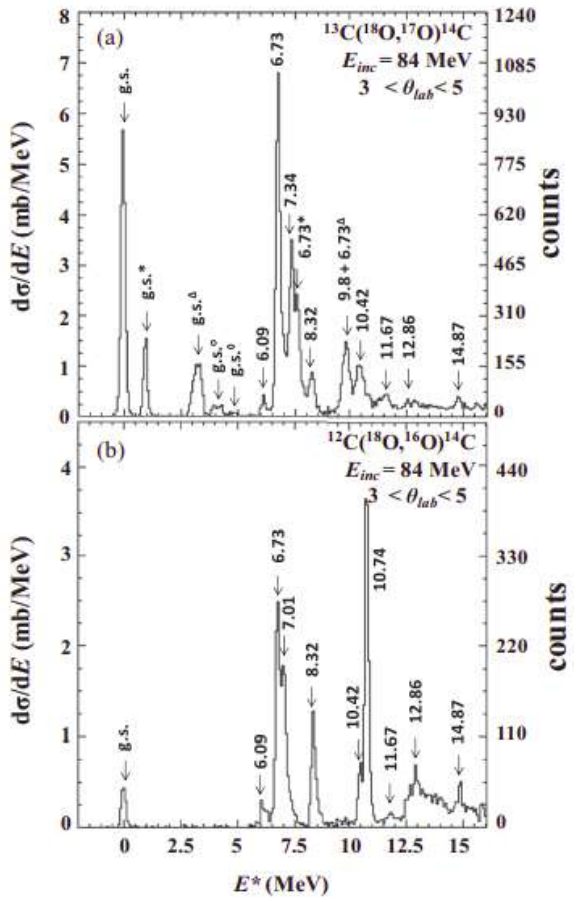

Figure 1.2: Excitation energy spectra for ^{14}C populated by the one-neutron ^{13}C(^{18}O,^{17}O), in panel a), and the two-neutron ^{12}C(^{18}O,^{16}O) reaction, in panel b). Extracted from [1].

that heavy ions. The selectivity and the role of pairing in two-proton and deuteron (proton-neutron bound system) transfer are still unclear.

This dissertation deals with the study of two-proton and deuteron transfer reactions in ^{27}Al and ^{28}Si targets induced by ^{16}O projectile at E_{lab} = 240 MeV. These target nuclei were chosen because: i) within the weak coupling, the ^{27}Al can be interpreted as a proton hole coupled to the ^{28}Si core, therefore they can be treated within the same nuclear structure model; ii) both target nuclei have the same number of neutrons and the $1d_{5/2}$ neutron sub-shell filled in their ground states. The intermediate one-nucleon transfer reactions were measured as well, in the same experimental campaign. This is important for the calculation since can be exploited to set constraints to the optical potential parameters and the model space adopted in the nuclear structure to extract the spectroscopic information, encoded in the spectroscopic amplitudes. The overall set of transfer reactions presented in this dissertation is shown in 1.3. The elastic and inelastic

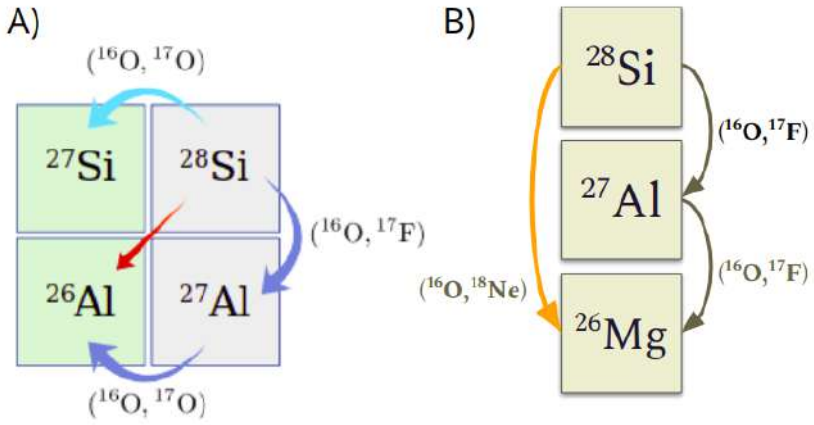

Figure 1.3: Panel a: transfer reactions studied for the deuteron transfer. Panel b: transfer reactions studied for the two-proton transfer.

scatterings for these systems have been analyzed previously in Ref. [30] and the coupled channel calculations satisfactorily reproduce the experimental data. We focus on the results of coupled reaction channels (CRC) for the one-proton and two-proton transfers to the target nuclei.

This dissertation is organized as it follows: Section 2 gives an overview of the theoretical background for this work; Section 3 introduces the experimental setup and how it acquires data; Section 4 discusses the details of the data reduction and cross-section attainment; and Section 5 presents our results and conclusions.

2 Heavy-ion transfer reaction overview

This chapter presents an overview of the theoretical framework to calculate cross-sections for direct reactions. This framework requires a consistent direct reaction model, that include other reaction channels that might be relevant, and an accurate model for the nuclear structures of the nuclei involved in the reaction.

Two methods frequently used in direct reactions are the distorted-waves and the coupled-channels. The distorted-wave approach assumes a full treatment of the elastic scattering wave function, usually by assuming an optical potential, whereas the components of nonelastic wave functions are treated in the first order in the coupling interaction. The coupled-channels methods deal with a set of coupled equations that arises from considering a model wave function with a limited number of terms. When these terms include elastic and inelastic scattering wave functions, so that all states belong to the same mass partition, it is referred to as coupled channels (CC). When it includes also states from more than one partition, as is the case in transfer reactions, it is referred to as coupled-reaction channels (CRC). A combination of CC, to treat the set of coupled equations within the same mass partition, and distorted-wave, to treat transfers to first order, can also be considered and is referred to as coupled-channels Born approximation (CCBA).

Besides a full quantum mechanical calculation is at hand, some insights about the transfer reaction induced by heavy ions can be obtained directly from a classical approach. This is handful to provide a general behavior of the transfer cross-section angular distribution and is presented in section 2.1.

2.1 A semiclassical approach for transfers: Brink's rule

Some features of heavy-ion reactions can be treated using the concepts of classical mechanics. Central to such considerations are short wavelengths, occasioned even at comparatively low energies by large reduced masses, large target-projectile Coulomb forces, and strong absorption seen at overlapping target-projectile separations. For

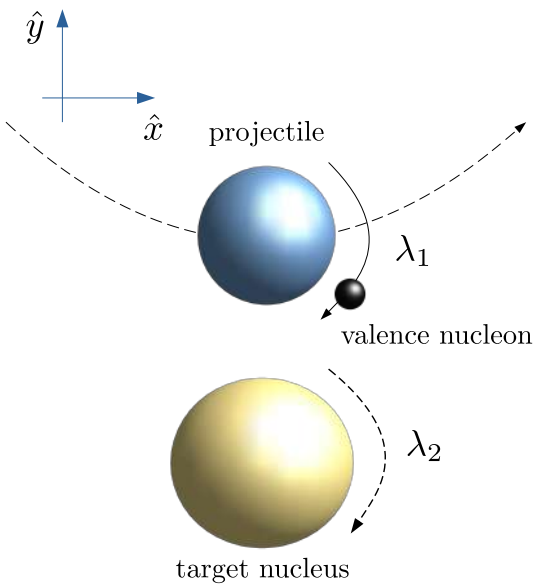

Figure 2.1: Diagram of the transfer reaction in terms of trajectories. Adapted from [31].

example, the asymptotic relative wave number k for a 240 MeV ^{16}O projectile incident in a mass-28 target is

$$k = \frac{\sqrt{2\mu E}}{\hbar} \approx 10.9 \text{ fm}^{-1}. \tag{2.1}$$

This corresponds to De Broglie wavelength of $\lambda = 2\pi/k \approx 0.6$ fm, which is small compared with the nuclear interaction radius given by

$$R = 1.25 \times \left(A_{\text{proj.}}^{1/3} + A_{\text{target}}^{1/3}\right) \text{ fm} \approx 6.9 \text{ fm}. \tag{2.2}$$

According to D. Brink [31], transfer reactions between heavy ions at energies well above the Coulomb barrier have a large cross-section only, if certain kinematical matching conditions are satisfied. These conditions are referred to as the Brink's matching conditions and are related to the Q-value of the reaction, the initial and final projections of the angular momenta and the kinematic energy. Consider the transfer process as depicted in Fig. 2.1, in which the z-axis is perpendicular to the scattering plane.

The orbital wave function of the valence nucleon in the projectile is in a single-particle state characterized by initial angular momentum ℓ_i in the λ_i projection. The conservation of angular momentum applies to the total angular momentum of the two nuclei. In the center of mass of the system, the total angular momentum is the sum of the internal

angular momentum of each nucleus - about its own center of mass - and the angular momentum of the relative motion. From a classical perspective, the angular motion of the valence particle is given by the component of the angular momentum λ and the nuclear radius. This matching condition gives

$$\Delta\ell = \lambda_f - \lambda_i + \frac{1}{2}k(R_i - R_f) + Q_{\text{eff}}\frac{R}{\hbar v} \approx 0 \tag{2.3}$$

where R_i and R_f are the radii of the two nuclei and $R = R_i + R_f$. The effective Q-value (Q_{eff}) is the reaction Q-value plus a term that takes into account the charges of the initial and final states, given by

$$Q_{\text{eff}} = Q - (Z_{f,1}Z_{f,2} - Z_{i,1}Z_{i,2})\frac{e^2}{R} \tag{2.4}$$

A second condition can be evoked, requiring that

$$\ell_1 + \lambda_1 = even; \qquad \ell_2 + \lambda_2 = even; \tag{2.5}$$

The third matching condition arises from simply requiring that the y-component of the momentum of the transferred nucleon should be *almost* conserved. For the valence nucleon before transfer, this component of the momentum is

$$p_{y,i} = mv - \frac{\hbar\lambda_i}{R_i}. \tag{2.6}$$

The term mv is the bulk motion of the projectile (in the center of mass of the total system) and the second term is due to rotation of the valence nucleon. Immediately after transfer, the y-component of the momentum is

$$p_{y,f} = \frac{\hbar\lambda_f}{R_f} \tag{2.7}$$

Finally, the matching condition for the y-component of the momentum requires that

$$\Delta k = \frac{mv}{\hbar} - \frac{\lambda_i}{R_i} - \frac{\lambda_f}{R_f} \approx 0. \tag{2.8}$$

To apply Brink's rule to the one-proton transfer reactions studied here, first the single-

reaction	Q-value (MeV)	Q_{eff} (MeV)	λ_i	λ_f ($\Delta\ell$ match.)	λ_f (Δk match.)	E_x match. (MeV)
^{28}Si(^{16}O,^{17}F)^{27}Al	-10.98	-12.02	0	2.7	2.1	2.8
^{27}Al(^{16}O,^{17}F)^{26}Mg	-7.67	-8.51	0	2.7	1.4	6.4

Table 2.1: Application of the Brink's rule to the one-proton transfer studied in this work. It is assumed that the valence proton occupies the $1d_{5/2}$ shell in the target nuclei. In both systems, the best matching is achieved assuming also $\lambda_i = 0$.

particle state of the valence proton must be assumed. A schematic proton distribution for the ^{27}Al is shown in Figure 2.2, for example purposes. In both ^{28}Si and ^{27}Al target nuclei, the last protons occupy the $1d_5/2$ shell. Therefore, $\ell_i = 2$ and there are three possible projections: $\lambda_i = -2, 0, +2$, since $\ell_1 + \lambda_1 = even$. Among these options, $\lambda_i = 0$ provides good matching conditions to populate low-lying states in the residual nuclei. This is shown in Table 2.1. For the ^{28}Si(^{16}O,^{17}F)^{27}Al reaction, $\Delta\ell$ matching condition (Eq. 2.3) is best for $\lambda_f = 2.7$. Recall that λ_f is an integer value. Therefore, the valence proton should populate a single-particle state in the f-shell at least. The Δk matching condition (Eq. 2.8) is best for $\lambda_f = 2.1$ instead. The matching between these condition is achieved when the valence proton populate states at $E_x = 2.5$ MeV in the ^{27}Al residual nucleus (see Table 2.1). For the ^{27}Al(^{16}O,^{17}F)^{26}Mg, optimized matching conditions is for transfers to states at $E_x = 6.4$ MeV.

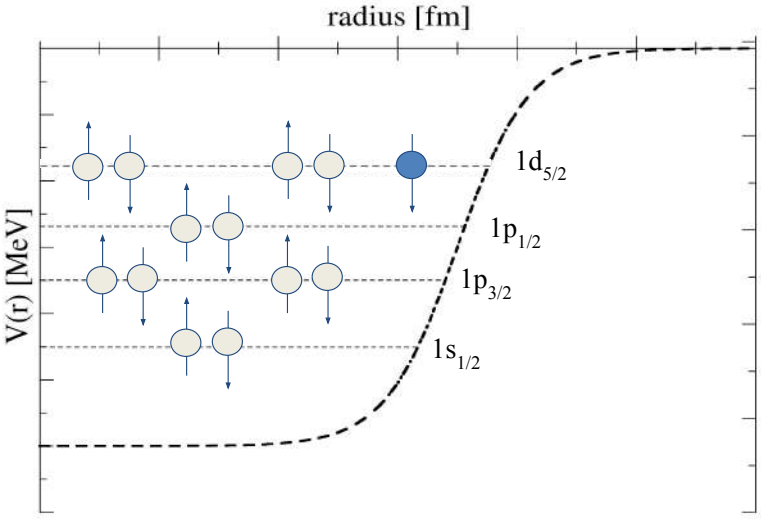

Figure 2.2: Shell model proton distribution scheme for the ^{27}Al. The separation between the levels are not in scale.

2.2 Direct reaction models

Some of the observables measured in nuclear reaction experiments are the cross-sections (differential or total) as a function of the projectile scattering angle or the projectile incidence energy. Therefore, the main objective of the theory of direct reactions is to predict these cross-sections by solving the system's equations of motion.

To standardize the language, a 2-body nuclear reaction is usually represented as $a + A \rightarrow b + B$ or, in short, $A(a, b)B$, where a and A are projectile and target cores, respectively. b and B are the ejectile (usually the detected particle) and the residual nuclei. In the specific case of elastic and inelastic scattering, $B \equiv A$ and $b \equiv a$. In the jargon of reaction theory, the systems $a+A$ and $b+B$ are called initial and exit mass partitions, respectively.

For non-relativistic energy regimes, the Schrödinger equation must be solved by introducing the necessary ingredients that describe the internal structures of both the projectile and target nuclei, and the potential that governs the interaction. The Hamiltonian of the input partition α, i.e. of the core-projectile and target system, is generically written as:

$$\mathcal{H}_\alpha = \mathcal{K}_R + \mathcal{H}_p(\varepsilon_p) + \mathcal{H}_t(\varepsilon_t) + V_\alpha(R_\alpha, \varepsilon_p, \varepsilon_t) \tag{2.9}$$

where $\mathcal{K}_R$ is the kinetic energy operator ($\equiv -\frac{\hbar^2}{2\mu}\nabla_R^2$) acting on the relative coordinate $\vec{R}$. $\mathcal{H}_p(\varepsilon_p)$ is the internal Hamiltonian that describes the state of the projectile nucleus (equivalent for the target nucleus with the term $\mathcal{H}_t(\varepsilon_t)$). $V(R, \varepsilon_p, \varepsilon_t)$ is the potential responsible for the description of the projectile-target interaction. Eventually, the ingredients for the description of the particles that result from the reaction should also be provided when they are different from the projectile and target nuclei.

In principle, one should resort to the time-dependent Schrödinger equation. Without demonstration, the time-dependent solution is equivalent to the time-independent solution that is predominantly implemented in algorithms (More details can be found in sections 4.1 and 4.2 of [32]). The wave function $\Psi(R, \varepsilon)$ is the time-independent solution of the Schrödinger equation,

$$\mathcal{H}\Psi(R, \varepsilon) = E\Psi(R, \varepsilon) \tag{2.10}$$

It is a second order differential equation whose solution must consider the appropriate boundary conditions to describe the scattering process. In the limits where the incident particle is very far from the center of the interaction potential $V_\alpha(R_\alpha, \varepsilon_p, \varepsilon_t)$, its wave function is described by a plane wave. After the reaction, several spherical waves are generated such that, in the asymptotic limit ($R \to \infty$) we have

$$\Psi^{(+)}(R, \varepsilon) \to \phi_p(\varepsilon_p)\phi_t(\varepsilon_t)e^{i\vec{K}_0\vec{R}} + \text{spherical waves} \tag{2.11}$$

The superscript "(+)" denotes the solution involving emerging spherical waves. Information relevant to the description of the various forward reactions is contained in the terms of "spherical waves" (see Chapter 8 in Ref.[33]). Thus, we can write spherical wave solutions of the type $\frac{e^{iKR}}{R}$,

$$\Psi^{(+)}(R, \varepsilon) \to \Phi_\alpha(\varepsilon_\alpha)e^{i\vec{K}_0\vec{R}} + \Phi_\alpha(\varepsilon_\alpha)f_{\alpha,\alpha}(\theta)\frac{e^{iK_\alpha R_\alpha}}{R_\alpha} + \sum_{\alpha' \neq \alpha} \Phi_{\alpha'}(\varepsilon_\alpha)f_{\alpha',\alpha}(\theta)\frac{e^{iK'_\alpha R_\alpha}}{R_\alpha} + \sum_\beta \Phi_\beta(\varepsilon_\beta)f_{\beta,\alpha}(\theta)\frac{e^{iK_\beta R_\beta}}{R_\beta} \tag{2.12}$$

where the last 3 terms describe different processes, namely: elastic scattering, inelastic scattering and processes leading to the final partition $\beta \neq \alpha$, such as nucleon transfer reactions. The $f(\theta)$ function is the scattering amplitude in a given θ direction (in the system's center of mass frame of reference).

Within quantum mechanics, the differential cross-section ($\frac{d\sigma}{d\Omega}$) is defined as the flux of particles passing through an area $dA = r^2 d\Omega$, centered on $\hat{\theta}$ direction, per incident flow unit. From this definition and exploring the concept of probability current density, it is shown that the differential cross-section for the reaction leading to the $\alpha \to \beta$ channel is completely determined by the scattering amplitude

$$\frac{d\sigma}{d\Omega}_{\alpha\to\beta} = \frac{v_\beta}{v_\alpha}|f_{\beta,\alpha}(\theta)|^2 \tag{2.13}$$

Similarly, the differential cross-section of inelastic (elastic) scattering is defined in terms of the amplitude $f_{\alpha',\alpha}(\theta)$ ($f_{\alpha,\alpha}(\theta)$). At this point, it is usual to define the transition matrix

(*T-matrix*) [32]:

$$\mathcal{T}_{\beta,\alpha}(\theta) = -\frac{2\pi\hbar^2}{\mu_\beta} f_{\beta,\alpha}(\theta) \tag{2.14}$$

such that

$$\frac{d\sigma}{d\Omega}_{\alpha\to\beta} = \frac{\mu_\alpha\mu_\beta}{(2\pi\hbar^2)^2}\left|\frac{K_\beta}{K_\alpha}\mathcal{T}_{\beta,\alpha}(\theta)\right|^2 \tag{2.15}$$

Also, for the reaction channel β, it is possible to determine an integral expression for the transition matrix $\mathcal{T}_{\beta,\alpha}(\theta)$. Exploring Green's method for solving non-homogeneous differential equations, we obtain

$$\mathcal{T}_{\beta,\alpha}(\theta) = \int\int e^{i\vec{K}_\beta\vec{R}_\beta}\Phi^*_\beta(\varepsilon_\beta)V_\beta(R_\beta,\varepsilon_\beta)\Psi^{(+)}_{K_\alpha}(R_\alpha,\varepsilon_\alpha)d\varepsilon_\beta dR_\beta \tag{2.16}$$

In summary, all the dynamics of the nuclear reaction are present in the scattering wave function $\Phi^{(+)}$ which, formally, is determined from the time-independent Schrödinger equation.

The solution of the equation in practice requires, in the first analysis, a reduction of the number of possible reaction channels (phase space) explicitly included in the function $\Phi^{(+)}$. The phase space restriction is motivated by the computational complexity of numerically treating several reaction channels and by the interest in analyzing the effects of a few channels in a comparative analysis with experimental data. Within this motivation, the Equation 2.10 equation is approximated by the following:

$$\mathcal{H}_{\text{eff}}\Psi_{\text{model}}(R,\varepsilon) = E\Psi_{\text{model}}(R,\varepsilon) \tag{2.17}$$

where $\mathcal{H}_{\text{eff}}$ is an effective Hamiltonian. It is important to point out that this effective Hamiltonian is complex, energy-dependent and non-local. Furthermore, it encompasses channel effects not explicitly considered in the Ψ_{model} scattering wave function. Therefore, the potentials that enter $\mathcal{H}_{\text{eff}}$ are usually determined phenomenologically through fitting procedures to experimental data.

Regarding the time-independent Schrödinger equation to be solved (Equation 2.17), for simplicity of presentation, we are ignoring the spins of the nuclei. This does not imply that particle spins have no effect on the scattering description. Furthermore, considering that the optical potential depends only on the relative coordinate R, it becomes convenient to

look for general solutions whose angular dependence (θ, ϕ) are described by the spherical harmonic functions $Y_{\ell,m}(\theta, \phi)$. The radial equation can also be expanded on a spherical harmonic basis. This method is known as **partial wave expansion** (see Chapter 8 in Ref. [33]). In practice, a time-independent Schrödinger equation is replaced by a sum of radial equations for each partial wave ℓ. On the other hand, the solution of each partial wave is easier to implement computationally, and usually some partial waves contribute significantly to the cross-sections.

The differential cross-section is related to the scattering amplitude (Equation 2.13) and which, within the approximations considered in the optical model, is given by:

$$f(\theta) = f_C(\theta) + \frac{1}{2iK}\sum_{\ell=0}^{\infty}(2\ell+1)e^{2i\sigma_\ell}(S_\ell - 1)P_\ell(cos\theta) \tag{2.18}$$

The first term is the scattering amplitude of pure Coulomb scattering, i.e. considering only the term $U_{\text{Coul.}}(R)$. The coefficients σ_ℓ are the phase difference in the scattering wave function introduced by the Coulomb potential for each partial wave ℓ. S_ℓ is the reflection coefficient or, more recognizably, S-matrix.

2.3 Optical model principles

In terms of phase space, the most basic approach is equivalent to considering only the ground states of the projectile and target nuclei, which effectively considers only the elastic scattering channel. In this case, the scattering wave function contains only the first two terms of Equation 2.12. The effective Hamiltonian is expressed as

$$\mathcal{H}_{\text{eff}} = \mathcal{K}_R + \mathcal{H}_\alpha(\varepsilon) + U_\alpha(R) \tag{2.19}$$

The effective interaction $U_\alpha(R)$ takes into account the effects of couplings of non-elastic reaction channels (for example, inelastic channels and transfers) on elastic scattering and, as mentioned earlier, is a complex potential, energy-dependent and non-local. The imaginary part of the potential takes into account the probability flux loss from the elastic channel to other channels. Energy dependency is usually incorporated phenomenologically by adjusting the potential parameters. The non-locality of the $U_\alpha(R)$

potential is rarely taken into account and sometimes introduced through a correction factor for local potentials, known as the Perey [34] factor. The $U_\alpha(R)$ potential that contains these features is called the **optical potential**.

The effective potential also contains the Coulomb potential ($U_{\text{Coul.}}(R)$). So the effective optical potential is

$$U_\alpha(R) = U_{\text{Coul.}}(R) + U_{\text{Nuc.}}(R) \tag{2.20}$$

where $U_{\text{Nuc.}}(R)$ is the nuclear term of the optical potential. The Coulomb term corresponds to the potential of a sphere of radius R_c with charge Ze uniformly distributed given by:

$$U_{\text{Coul.}}(R) = \begin{cases} \frac{Z_p Z_t e^2}{2R_c}\left(3 - \frac{R^2}{R_c^2}\right) & \text{se } R \leq R_c \\ \frac{Z_p Z_t e^2}{R} & \text{se } R \geq R_c \end{cases} \tag{2.21}$$

For the nuclear term, we consider a complex central potential of the type

$$U_{\text{Nuc.}}(R) = V(R) + iW(R) \tag{2.22}$$

The nuclear potential is usually described by an attractive potential, with a range slightly greater than the radius of nuclear and diffuse matter. It is common to use Woods-Saxon type functions

$$V(R) = \frac{V_r}{1 + \exp\left\{\frac{R - R_r}{a_r}\right\}} \tag{2.23}$$

where V_r, R_r and a_r are the depth, radius and diffusivity of the potential and which are generally free parameters to fit to the experimental data. The same form of function is used for the real and imaginary part of the effective nuclear potential, resulting in 6 free parameters fitted to the data. If experimental data for a given nuclear projectile scattered by several targets of mass A are simultaneously well described by the same optical potential (within small variations of the parameters), we have what is called *global optical potential*. However, the success of these types of global potentials is restricted to the scattering of light ions (p, d, ^{4}He). For heavy systems $A \geq 8$, the accuracy obtained with global potentials is very low, which favored the compilation of specific optical potentials for each energy-projectile-target combination.

An alternative to the adjusted or global potentials is the **single or double convolution**

potential obtained from the nuclear matter density distributions of one of the nuclei (single convolution) or of both nuclei (double convolution). Among the double convolution potentials, the São Paulo potential [35] is one of the most used to describe the elastic scattering of different systems and energies. In its non-local formalism, the potential of São Paulo is given by:

$$V_{SPP}(R) = V_F(R) \exp\left\{\frac{-4v^2}{c^2}\right\} \tag{2.24}$$

where c is the speed of light, v is the relative (non-relativistic) speed between the nuclei and $V_F(R)$ is the double convolution term involving the density distributions of the nuclei ($\rho_1(\vec{r}_1)$ and $\rho_2(\vec{r}_2)$) given by:

$$V_F(R) = \int \rho_1(\vec{r}_1)\rho_2(\vec{r}_2)V_0\delta(\vec{R} - \vec{r}_1 + \vec{r}_2)d\vec{r}_1 d\vec{r}_2 \tag{2.25}$$

with $V_0 = -456$ MeV.fm^3. The Dirac delta appears with the idea that the emission and absorption of the nucleon exchanged between the nuclei happens at the same point (zero range approximation), this, in practice, causes the sixfold integral to become a triple integral. When the Dirac delta function is used instead of a more refined approach for the nucleon-nucleon interaction, the size of the nucleon should be taken into account, as matter density is not the same as nucleon density. More details on this topic can be found in [35].

2.4 Coupled Channels Formalism

To describe non-elastic processes, it is necessary to solve Equation 2.16. If it is possible to consider that the non-elastic reaction channel is loosely coupled to the elastic channel, then the perturbative treatment can be adopted.

Considering the following expansion for the scattering wave function,

$$\Psi^{(+)}(R,\varepsilon) = \phi_0(\varepsilon)\chi_0(R) + \sum_{n>0}^{N} \phi_n(\varepsilon)\chi_n(R) \tag{2.26}$$

where $\phi_0(\varepsilon)$ is the wave function describing the projectile and target nuclei in their ground states. The coefficients $\chi_n(R)$ describe the relative coordinate movement within each reaction channel n. The wave function $\Psi^{(+)}(R,\varepsilon)$ must satisfy the time-independent

Schrödinger equation,

$$[E - \mathcal{H}]\, \Psi^{(+)}(R, \varepsilon) = 0 \tag{2.27}$$

Multiplying both sides of this equation by the internal functions $\phi_n^*(\varepsilon)$, and integrating over the internal coordinates ε, we obtain a set of n coupled equations of the type

$$[E - \epsilon_n - \mathcal{T}_R - V_{n,n}(R)]\, \chi_n(R) = \sum_{n' \neq n} V_{n,n'}(R) \chi_{n'}(R) \tag{2.28}$$

where ϵ_n is the eigenvalue for the inner Hamiltonian, such that $H(\varepsilon)\phi_n(\varepsilon) = \epsilon_n \phi_n(\varepsilon)$. $V_{n,n'}(R)$ are the coupling potentials between channels n and n', defined as:

$$V_{n,n'}(R) = \int d\varepsilon \phi_n^*(\varepsilon) V(\varepsilon, R) \phi_{n'}(\varepsilon) \tag{2.29}$$

The coupling potential is the main ingredient for handling non-elastic processes. For example, $V_{0,n'}(R)$ is the coupling potential responsible for the transition from the fundamental states ($n = 0$) to the states defined in the channel n'.

Some aspects should be highlighted regarding Equation 2.28

- the potential $V(\varepsilon, R)$ and the internal wave functions $\phi_{n'}(\varepsilon)$ are modeled
- the radial functions $\chi_n(R)$ must satisfy asymptotic boundary conditions ($R \to \infty$)
- depends on both the function $\chi_n(R)$ and $\chi_{n'}(R)$ and both are initially unknown. Therefore, the Equation 2.28 is also called the **set of coupled equations**.

The set of n coupled equations (Equation 2.29) must be solved iteratively, starting from the equation for the elastic channel ($n = 0$). This allows to determine the distorted wave function $\chi_0(R)$, which is inserted into the nth coupled equation and determining the solution $\chi_n(R)$ in first order. Up to this point, the iterative solution process is called the 1st-order Distorted Wave Born Approximation (*1-step* DWBA). In this order of approximation, the elastic scattering wave function is not corrected for possible coupling from non-elastic channels. In other words, this means that, in 1-step DWBA, the elastic scattering cross-section is not altered by the inclusion of non-elastic channels.

Once the function $\chi_n(R)$ is determined in the 1st iteration, one can return to the elastic

channel equation and determine the solution for $\chi_0(R)$. This process is called **2-step DWBA**. The process is self-consistent and after N iterations, the solutions tend to converge. Typically, N-step DWBA solutions are called Coupled-Channels (CC). This topic is discussed in more detail in section 2.5 of the [36] reference.

2.4.1 Coupling to inelastic channels

Inelastic reaction channels are processes in which the projectile and target nuclei preserve their identities but alter their intrinsic states. For simplicity, only situations will be considered in which one of the nuclei (projectile) undergoes the excitation of its intrinsic states. However, the method can also be applied to inelastic channels that result in target nucleus excitation and simultaneous projectile and target excitation processes.

The main ingredient is the coupling potentials between channels n and n' (Equation 2.29). It is convenient to express the internal wave functions in terms of their angular momentum and projection (in Dirac notation):

$$|\phi_i\rangle \equiv |i; I_i M_i\rangle \qquad |\phi_f\rangle \equiv |f; I_f M_f\rangle \tag{2.30}$$

The effective potential $V(\varepsilon, R)$ must consider the contributions of the Coulomb terms (Coulomb excitations) and nuclear (nuclear excitations).

It is convenient to expand the Coulomb potential in terms of the λ multipoles. Without proofs, the Coulomb potential is written as:

$$V(\varepsilon, R) = \sum_{\lambda,\mu} \frac{4\pi}{2\lambda+1} \frac{Z_t e}{R^{\lambda+1}} M(E\lambda, \mu) Y^*_{\lambda\mu}(\theta, \phi) \tag{2.31}$$

where $M(E\lambda, \mu)$ is the electric multipole operator and that depends on the internal coordinates of the projectile nucleus. In DWBA approximation, the scattering amplitude by Coulomb excitation is

$$f(\theta)_{i\to f} = -\frac{\mu Z_t e}{2\pi\hbar^2} \langle f; I_f M_f | M(E\lambda, \mu) | i; I_i M_i \rangle \, \mathcal{T}_{i,f}(K_f, K_i) \tag{2.32}$$

This equation shows that, in DWBA, the scattering amplitude is factored into 2 terms. The first, associated with the amplitude $\mathcal{T}_{i,f}(K_f, K_i)$, describes the dynamics of the

reaction. The second, $\langle f; I_f M_f | M(E\lambda,\mu) | i; I_i M_i \rangle$ called the matrix element of the electric multipole operator, contains all the information about the structure of the nucleus to be excited. Using the Wigner-Eckart theorem,

$$\langle f; I_f M_f | M(E\lambda,\mu) | i; I_i M_i \rangle = \langle I_f M_f | \lambda\mu I_i M_i \rangle \langle f; I_f || M(E\lambda,\mu) || i; I_i \rangle \tag{2.33}$$

where $\langle f; I_f || M(E\lambda,\mu) || i; I_i \rangle$ are **the reduced matrix elements of the electric operator** $E\lambda$. $\langle I_f M_f | \lambda\mu I_i M_i \rangle$ is the Clebsch-Gordan coefficient.

The reduced matrix element of the $E\lambda$ operator is related to the reduced transition probability $B(E\lambda; i \to f)$,

$$B(E\lambda; i \to f) = \frac{2I_f + 1}{2I_i + 1} \left| \langle f; I_f || M(E\lambda,\mu) || i; I_i \rangle \right|^2 \tag{2.34}$$

and that it is a quantity determined experimentally through the gamma decays of the transition of interest or from Coulomb excitation measurements.

In the case of the nuclear potential, the transitions are interpreted as deformations of the surface of the nucleus around the spherical distribution. The angular dependence of the deformed core surface can be expressed in terms of spherical harmonics,

$$r(\theta,\phi) = R_0 + \sum_{\lambda,\mu} \hat{\delta}_{\lambda\mu} Y^*_{\lambda\mu}(\theta,\phi) \tag{2.35}$$

where $\hat{\delta}_{\lambda\mu}$ is the deformation length operator. Typically, the most relevant deformations are quadrupole ($\lambda = 2$) and octupolar ($\lambda = 3$). Assuming that the nuclear interaction accompanies the deformation of the nucleus, we have

$$V(\varepsilon, R) = V(R - r(\theta,\phi)) \tag{2.36}$$

and, assuming that the deformation is small compared to the diffusivity of the potential, by Taylor expansion we have

$$V(\varepsilon, R) = V(R - R_0) - \sum_{\lambda,\mu} \hat{\delta}_{\lambda,\mu} \frac{dV(R - R_0)}{dR} Y^*_{\lambda\mu}(\theta,\phi) + ... \tag{2.37}$$

The coupling potential relevant to the DWBA formalism is

$$V(R)_{if} \equiv= \langle f; I_f M_f | V | i; I_i M_i \rangle = -\frac{dV_0(R-R_0)}{dR} \sum_{\lambda\mu} \langle f; I_f M_f | \hat{\delta}_{\lambda\mu} | i; I_i M_i \rangle \, Y^*_{\lambda\mu}(\theta, \phi) \tag{2.38}$$

where $\langle f; I_f M_f | \hat{\delta}_{\lambda\mu} | i; I_i M_i \rangle$ is the deformation operator array element. Again, applying the Wigner-Eckart theorem,

$$\langle f; I_f M_f | \hat{\delta}_{\lambda\mu} | i; I_i M_i \rangle = \langle f; I_f M_f | \lambda\mu I_i M_i \rangle \, \langle f; I_f || \hat{\delta}_{\lambda} || i; I_i \rangle \tag{2.39}$$

The deformation reduced matrix element $\langle f; I_f || \hat{\delta}_{\lambda} || i; I_i \rangle$ is the main ingredient and is related to the core deformation structure. In particular, considering the rotational model, the value of the reduced matrix element becomes proportional to the parameters β_λ and R_0 (deformation parameter and projectile nuclear radius, respectively)

$$\langle f; I_f || \hat{\delta}_{\lambda} || i; I_i \rangle = (-1)^{I_f - I_i} \, \langle I_f K \lambda 0 | I_i K \rangle \, \beta_\lambda R_0 \tag{2.40}$$

2.5 Coupled Reactions Channels

Whenever transfer of one or more particles between projectile and target nuclei are involved, the $\Psi_{\text{model}}(R, \epsilon)$ scattering wave function must include terms from two or more partitions, as indicated by Eq.(2.12). Generalization of the coupled-channel method to transfer reactions introduces some new features that must dealt with, such as the non-orthogonality of the wave functions from different mass partitions and the non-remnant terms. The non-orthogonality is easier to explain at this point. It means that the overlap between internal states in the α and β mass partitions are not zero:

$$\int \Phi^*_\alpha(\epsilon_\alpha) \Phi_\beta(\epsilon_\beta) d\vec{r}_\alpha \neq 0 \tag{2.41}$$

To keep this topic simple, let us consider the transfer of one nucleon η and only two reaction channels α, the elastic channels, and β, the transfer channels. This process can be represented as $A(a,b)B$, as previously seen, where $a = b + \eta$ and $B = A + \eta$. The coordinate system in indicated in Fig. 2.3. Consider the 2-state wave function for the

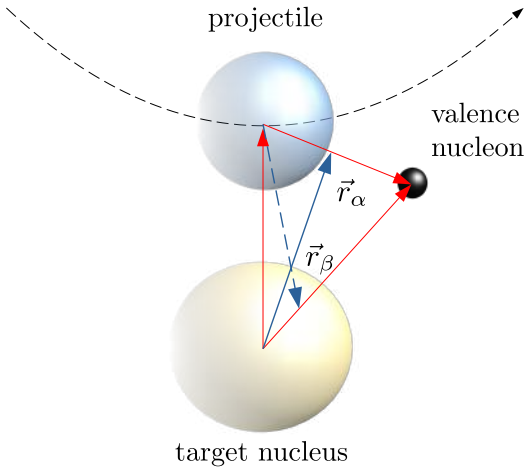

Figure 2.3: Coordinates for transfer reactions. The $\vec{r}_\alpha$ (solid blue arrow) connects the target nucleus to the center of mass of the core + nucleon system in the initial mass partition, whereas the $\vec{r}_\beta$ (dashed blue arrow) connects the core nucleus to the center of mass of the target + nucleon system in the final mass partition.

transfer reaction from α to β mass partitions,

$$\Psi^{(+)}(R_\alpha, \varepsilon_\alpha, R_\beta, \varepsilon_\beta) = \phi_\alpha(\varepsilon_\alpha)\chi_\alpha(R_\alpha) + \phi_\beta(\varepsilon_\beta)\chi_\beta(R_\beta) \tag{2.42}$$

where ϕ_α and ϕ_β are the wave functions that describe the internal nuclear states of both nuclei in the initial α and final β partitions, respectively. $\chi_\alpha(R)$ and $\chi_\beta(R)$ are the asymptotic form of the wave functions distorted by interacting potentials in the initial and final partitions.

The total Hamiltonian for the system is the sum of the internal Hamiltonian $\mathcal{H}_\alpha(\varepsilon_\alpha)$, that describes the states in the a and A nuclei, the kinetic energy of their relative motion $\mathcal{T}_\alpha(R_\alpha)$ and their interacting potential $\mathcal{V}_\alpha(R_\alpha, \varepsilon_\alpha)$. The internal Hamiltonian satisfy the following eigen-equation:

$$\mathcal{H}_\alpha(\varepsilon_\alpha)\phi_\alpha(\varepsilon_\alpha) = \epsilon_\alpha\phi_\alpha(\varepsilon_\alpha) \tag{2.43}$$

with eigenenergy ϵ_α. The kinetic energy operator depends on the reduced mass a and A (μ_α), in the α mass partition, and the radial coordinate R_α:

$$\mathcal{T}_\alpha = -\frac{\hbar^2}{2\mu_\alpha}\nabla^2_{R_\alpha}. \tag{2.44}$$

Major difficulties arise with the interacting potential $\mathcal{V}_\alpha(R_\alpha, \varepsilon_\alpha)$, since depends on both

radial R_α and the internal ε_α coordinates.

The same can be written for all mass partitions included, so that:

$$\mathcal{H} = \mathcal{H}_\alpha + \mathcal{T}_\alpha + \mathcal{V}_\alpha = \mathcal{H}_\beta + \mathcal{T}_\beta + \mathcal{V}_\beta \tag{2.45}$$

such that Equation 2.42 satisfy the time-independent Schrödinger equation:

$$\mathcal{H}\Psi^{(+)}(R,\varepsilon) = \mathcal{E}\Psi^{(+)}(R,\varepsilon), \tag{2.46}$$

in which R and ε includes information of all partitions. We can project the Schrödinger equation into states in the α and β partitions. To indicate this, we adopt, again, the Dirac notation,

$$\langle\phi_\alpha|\left(\mathcal{H}-\mathcal{E}\right)\left|\Psi^{(+)}\right\rangle = 0 \qquad \langle\phi_\beta|\left(\mathcal{H}-\mathcal{E}\right)\left|\Psi^{(+)}\right\rangle = 0 \tag{2.47}$$

These two projections give a pair of the following coupled-reaction-channel equations

$$\left[(\varepsilon_\alpha - \mathcal{E}) + K_\alpha + \langle\phi_\alpha|\,\mathcal{V}_\alpha\,|\phi_\alpha\rangle\right]\chi_\alpha(R_\alpha) = \langle\phi_\alpha|\left(\mathcal{E}-\mathcal{H}\right)|\phi_\beta\chi_\beta\rangle \tag{2.48}$$

$$\left[(\varepsilon_\beta - \mathcal{E}) + K_\beta + \langle\phi_\beta|\,\mathcal{V}_\beta\,|\phi_\beta\rangle\right]\chi_\beta(R_\beta) = \langle\phi_\beta|\left(\mathcal{E}-\mathcal{H}\right)|\phi_\alpha\chi_\alpha\rangle \tag{2.49}$$

The terms on the right represent integro-differential given by

$$\langle\phi_\alpha|\left(\mathcal{E}-\mathcal{H}\right)|\phi_\beta\chi_\beta\rangle = \int d\vec{R}_\beta K_{\alpha\beta}(\vec{R}_\alpha,\vec{R}_\beta)\chi_\beta(\vec{R}_\beta) \tag{2.50}$$

where $K_{\alpha\beta}(\vec{R}_\alpha,\vec{R}_\beta)$ is known as the kernel, that involves the radial coordinates in the α and β mass partitions. An equivalent expression is obtained for the $K_{\beta\alpha}(\vec{R}_\beta,\vec{R}_\alpha)$. To calculates these kernels, one have the freedom to choose a particular definition for the $\mathcal{H}$. If these operator is defined in terms of the operators of the α partition, this is referred as the *prior* representation. In the other case, using operators defined in the β partition, it is called *post* representation. Usually this choice is guided by some level of confidence on the interacting potential. For instance, the prior representation it is adopted throughout this work since the interaction potential also describe the elastic and inelastic scatterings

of the initial mass partition.

At the end of the day, an equivalent transition matrix $\mathcal{T}_{\beta,\alpha}(\theta)$ (see Eq.2.51) must be defined and solved to obtain the transfer cross-sections. In the prior representation, this is now defined as

$$\mathcal{T}_{\alpha,\beta}(\theta) = \int\int \chi^*_\alpha(\vec{K}_\alpha, \vec{R}_\alpha)\phi^*_\alpha(\varepsilon_\alpha)\ \mathcal{V}_\alpha\ \chi_\beta(\vec{K}_\beta, \vec{R}_\beta)\phi_\beta(\varepsilon_\beta)d\varepsilon_\alpha dR_\alpha \tag{2.51}$$

The transition matrix requires the evaluation of the following integral:

$$\int d\varepsilon_\alpha \phi^*_\alpha(\varepsilon_\alpha, \vec{R}_\alpha)\phi_\beta(\varepsilon_\beta) \equiv \langle\phi_\alpha|\phi_\beta\rangle \tag{2.52}$$

that is known as the **overlap integral**. This is evaluated using the parentage decomposition of the composite nucleus B, which is described as a nuclear core A + particle:

$$\phi_\alpha(\varepsilon_\alpha, \vec{R}_\alpha) = \mathcal{S}^{\ell,j}\phi_\beta(\varepsilon_\beta)\psi^{\ell,j}_{n,A}(\vec{r}) \tag{2.53}$$

where $\psi^{\ell,j}_{n,A}(\vec{r})$ is the single-particle wave function, with orbital angular momentum ℓ and total angular momentum j, describing the motion of the n particle with respect to the nuclear core A. In some case, more than one single-particle component might be required to a full description. The $\mathcal{S}^{\ell,j}$ is the **spectroscopic amplitude**, which measures the single-particle content of a given state of the composite nucleus B when describe as $A+n$ system.

Usually these single-particle component are determined from a time-independent Schrödinger equation solved for a phenomenological potential such as the Wood-Saxon potential. This is usually referred to as the binding potential (or form factor) and the depth is adjusted to obtain an eigenenergies that reproduce the binding energy of the particle n to its core A. Examples of the radial component of these single-particle states are shown in Fig. 2.4

2.6 Key ingredients and codes used for calculations

In this dissertation, all calculations were performed using the code FRESCO (English acronym for *Finite Range with Exact Strong COuplings*) version 3.2 [38].

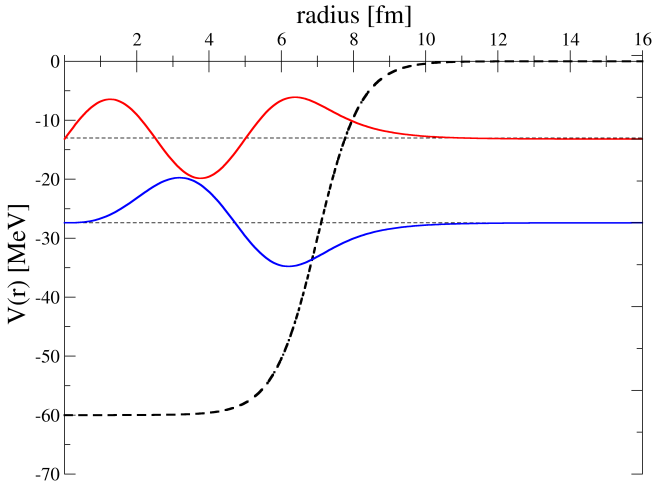

Figure 2.4: Examples of radial single-particle wave functions with main quantum number $n = 1$ (blue curve) and $n = 2$ (red curve) obtained assuming a Wood-Saxon binding potential (dashed curve). Adapted from [37].

For the effective nuclear potential, present in Equation 2.19, the São Paulo potential (Equation 2.24) will be used as *bare* potential for the optical potential in the form

$$U_{\text{Nuc.}}(r) = (N_r + i.N_i)\, V_{SPP}(r) \tag{2.54}$$

where N_r and N_i are the normalization factor of the real and imaginary terms of the potential. Based on a systematic description of elastic scattering in several systems, the average values of these parameters are $N_r = 1.0$ and $N_i = 0.78$ [39]. In this dissertation, the normalization of the real term is fixed at 1.0 while the imaginary factor will be adjusted to the experimental data.

Couplings with inelastic channels will be included through the Reduced electromagnetic transition probability $B(E\lambda; i \to f)$ (Equation 2.34), for the deformation of the Coulomb potential, and parameters β_λ and R_0 (present in Equation 2.40) for nuclear deformation. In all calculations, partial wave contributions were considered, at least, up to $\ell = 500\hbar$, which is sufficient for the convergence of theoretical calculations.

Spectroscopic amplitudes for the overlap functions in the CRC calculations were obtained from shell models, using the NuShellX code.

3 Experimental setup and data acquisition

The experimental data analyzed in this dissertation has been obtained at *Istituto Nazionale di Fisica Nucleare - Laboratori del Sud* (INFN-LNS) in Catania, Italy, in 2016. These measurements consisted of a 240-MeV ^{16}O beam, produced in the K800 Superconducting Cyclotron, impinging on ^{28}Si and ^{27}Al self-supported targets. After such beam-target interaction, ejectiles at very forward angles, emerging from the target, are momentum analyzed by the MAGNEX spectrometer, which performs particle identification when combined with the Focal Plane Detector (FPD).

In this chapter, we will give an overview on the experimental setup and data acquisition for the experimental data presented in this work. The results for the elastic and inelastic scattering for this experimental campaign have been published in 2019 [3].

3.1 Beam extraction and acceleration

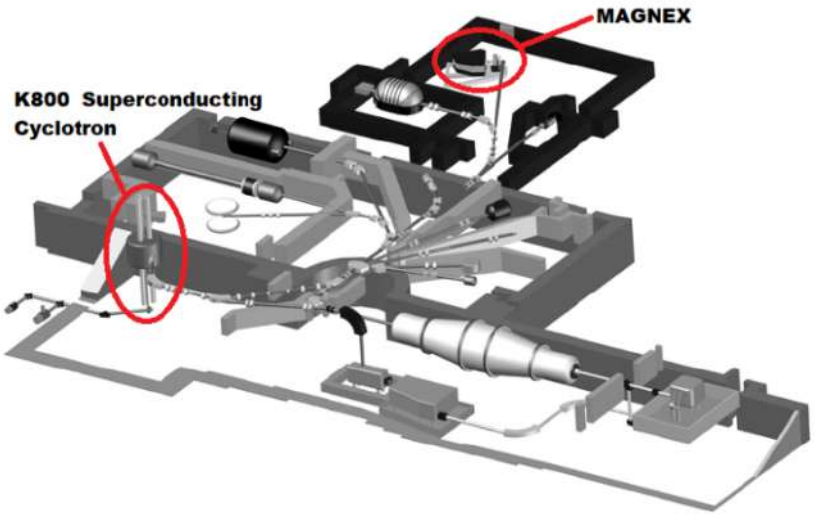

Figure 3.1: INFN-LNS facility scheme. The location of K800 Superconducting Cyclotron and MAGNEX are marked in red ellipses and identified. Modified from [40].

A diagram scheme of the INFN-LNS facility is reproduced in Fig. 3.1. For the K800 Superconducting Cyclotron, ions are produced by a plasma-based ion source feeding particle accelerators with highly charged ions. The ions are extracted from a high density and high temperature plasma ($n_e \sim 10^{10} - 10^{13}$ cm^{-3}, $T \sim$ 0.1 – 100 keV) generated

by means of the electron cyclotron resonance heating. The plasma is excited inside a cylindrical metallic chamber by microwaves and confined by magnetic fields.

The ^{16}O beam is vertically injected into the K800 Superconductor Cyclotron (SC). Due to the magnetic fields generated by the superconductors, the particles go through a descending spiral path, being accelerated when it passes through the gaps, called dees, due to the presence of a high-frequency oscillating electric field. The spiral trajectory goes outwards and, when reaching the selected energy, the particles are found in the maximum radius orbit and are extracted using an electrostatic deflector, applying a transverse electric field to deflect the beam to the extraction line.

Since all measurements were performed at very forward angles ($\theta_{\text{lab}} < 15°$), cross-sections for the elastic scattering are relatively higher compared with the transfer channels. Therefore, the data acquisition demanded low beam intensity, usually between 1 and 5 nA. The beam was directed to the MAGNEX experimental room, indicated in Fig. 3.1.

3.2 The MAGNEX experimental room

The experimental setup consists of the scattering chamber, a set of quadrupole and dipole magnets and a focal plane detector. Photographs of the MAGNEX experimental room are shown in Fig. 3.2. Magnetic spectrometers are a good option for accurate energy measurements and to detect reaction products at very forward angles, including zero degree. Different layouts have been developed to optimize detection of light or heavy particles.

Before entering the spectrometer, the ^{16}O beam interacts with the targets, ^{28}Si and ^{27}Al, that were loaded on a 5-position target holder, inside the scattering chamber. Target positioning relative to the beam axis is controlled by a PC board, which allows moving the target holder without venting the scattering chamber. The thickness of each target used in this experimental campaign were 89 $\mu g/cm^2$, for the ^{27}Al foil, and 148 $\mu g/cm^2$, for the ^{28}Si foil. The ejectiles were then momentum analyzed by the spectrometer.

The MAGNEX is a large acceptance magnetic spectrometer, in which the magnetic fields generated by its magnetic elements deflect the incoming beam to different positions in the Focal Plane Detector, corresponding to the magnetic rigidity, momentum, position

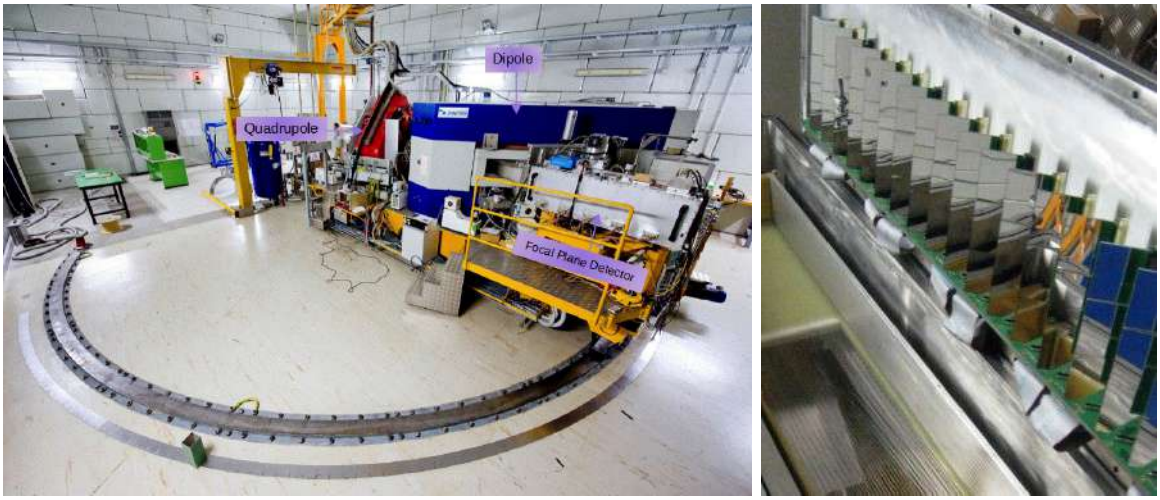

Figure 3.2: Photographs from the MAGNEX experimental room. Left: Overall view of the MAGNEX spectrometer; the Quadrupole, Dipole and Focal Plane Detector are visible and identified with the lilac boxes. Right: View from the interior of the Focal Plane Detector, where the silicon detector wall is visible. Modified from [41].

and incident angle of the incoming particle. The spectrometer is composed of a pair of magnetic elements, a dipole and a quadrupole, and a detection system. The success of large acceptance spectrometers relies on advanced algorithms to study the transport of the ions through the magnetic elements and proper description of magnetic aberrations. To achieve this goal, a detailed measurement of the magnetic field was performed during the assembly of the magnets to set the highly non-linear differential equations [42].

In Figure 3.3, the dipole and quadrupole are indicated. Both elements are responsible for affecting the ejectile beam in different directions. For instance, the quadrupole magnet focuses the beam in the vertical direction, perpendicular to both Z and X axis indicated in the figure. The dipole, though, not only focuses the beam in the horizontal direction - the plane created by Z and X axis - yet, it disperses the beam according to its magnetic rigidity, momentum and charge. The horizontal focus is also improved by the inclination of both the entrance and exit dipole boundaries and the use of surface coils between the dipole poles and the vacuum vessel. The accepted magnetic rigidities range from $B.\rho \sim 0.2$ T.m to ~ 1.8 T.m, corresponding to energies of the detected ions ranging from E$\sim$ 0.2 MeV/A to E$\sim$ 40 MeV/A, depending on their mass and charge. In terms of the target's reference system, this spectrometer allows measuring scattering angles between $\sim -5°$ to $\sim +5°$ around its optical axis.

For the measurements used in this dissertation, the optical axis of MAGNEX was

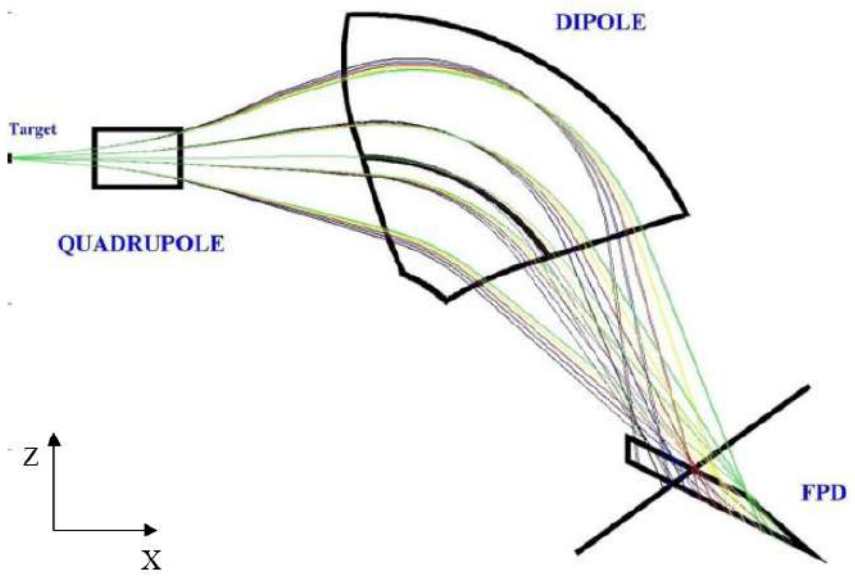

Figure 3.3: Top view of a MAGNEX spectrometer trajectory simulation. Particles with distinct momentum are represented with colored lines. Quadrupole, Dipole and FPD physical borders are represented in the figure. Modified from [42].

positioned at $\theta_{\rm lab}^{\rm opt} = 3°$ and $8°$. This allows to scan scattering angles between $0° < \theta_{lab} <\sim 12°$ in the target's reference system.

The simulated horizontal beam envelope through the spectrometer is shown in Fig. 3.3. A number of trajectories with initial conditions distributed through the phase space accepted by the spectrometer are indicated. Rays with different colors have different momentum. For instance, the green rays depict particle's trajectories scattered at different angles at the target position. Note that these rays practically hits the same region at the focal plane detector with distinct incident angles (see FPD in Fig. 3.3). This means that the focal plane detector must measure all kinematic parameters of the incident particle.

3.3 Focal Plane Detector (FPD)

The Focal Plane Detector (FPD) is a hybrid detector, composed of a gaseous section and a wall of 60 silicon particle detectors. It combines E-ΔE technique, for particle identification, with measurements of position and incident angles of the incident particles. The FPD is installed with the entrance surface rotated of $\theta_{\rm tilt} = 59.2°$, with respect to the central trajectory, in order to reduce the effect of chromatic aberrations of the magnets.

The FPD active is manufactured in stainless steel vessel with a unique aperture at the front housing a thin Mylar window. Typical thickness of the Mylar is between 1.5 μm to 6.0 μm, depending on requirements of the particle to be detected. The FPD gas used in the experiment is N35 isobutane (99.95% pure) at 15 mbar.

When entering the FPD, a particle ionizes the gas between the cathode and the Frisch Grid, creating electrons that are drifted upwards due to a uniform electric field in this region, as represented in Figure 3.4-a. Drift Counters (DC1-4) and Proportional Counters (PC) wires are used for measuring the energy lost in the gas. Between the grid and the wires, the electrons are now accelerated towards the DC and PC wires thanks to a non-uniform electric field, creating an avalanche of electrons that will produce a signal proportional to the energy lost by the particle in that gaseous section (ΔE).

DC wires signal also measure the particle's horizontal and vertical positions. The horizontal position X of a particle is obtained by measuring the induced charge distribution on the induction pads for each DC wire, also caused by the previous avalanche of electrons. Besides, its vertical position Y is measured by the electron drift time from the gas ionization to a DC wire, more precisely by obtaining the delay between the signal obtained in the silicon detector and the wire.

Measurements are also be obtained referring to the optical axis of the spectrometer, by combining the position measurements in each DC wire and resulting in the X and Y positions of the particle in relation to it, namely X_{foc} and Y_{foc}. Additionally, such relative X_{foc} and Y_{foc} positions allow the extraction of the incident angles θ_{foc} and ϕ_{foc} of the ion trajectory at the spectrometer focal plane (check Figure 3.4). Also, the energy lost by the particle in the gaseous section of the FPD requires a slight correction due to the path difference of particles with different incident angles, yielding the ΔE_{corr} parameter. Finally, the charged particle is stopped when reaching the silicon detector wall, yielding the measurement of the residual energy of a particle (E_{res}).

In summary, for each ion that arrives in the detection system, more than fourteen parameters are stored by the electronic and including ΔE_{corr}, E_{res}, X_{foc}, Y_{foc}, θ_{foc} and ϕ_{foc}, essential to the particle identification and trajectory reconstruction.

The trajectory reconstruction means that the initial kinematics parameters are calculated

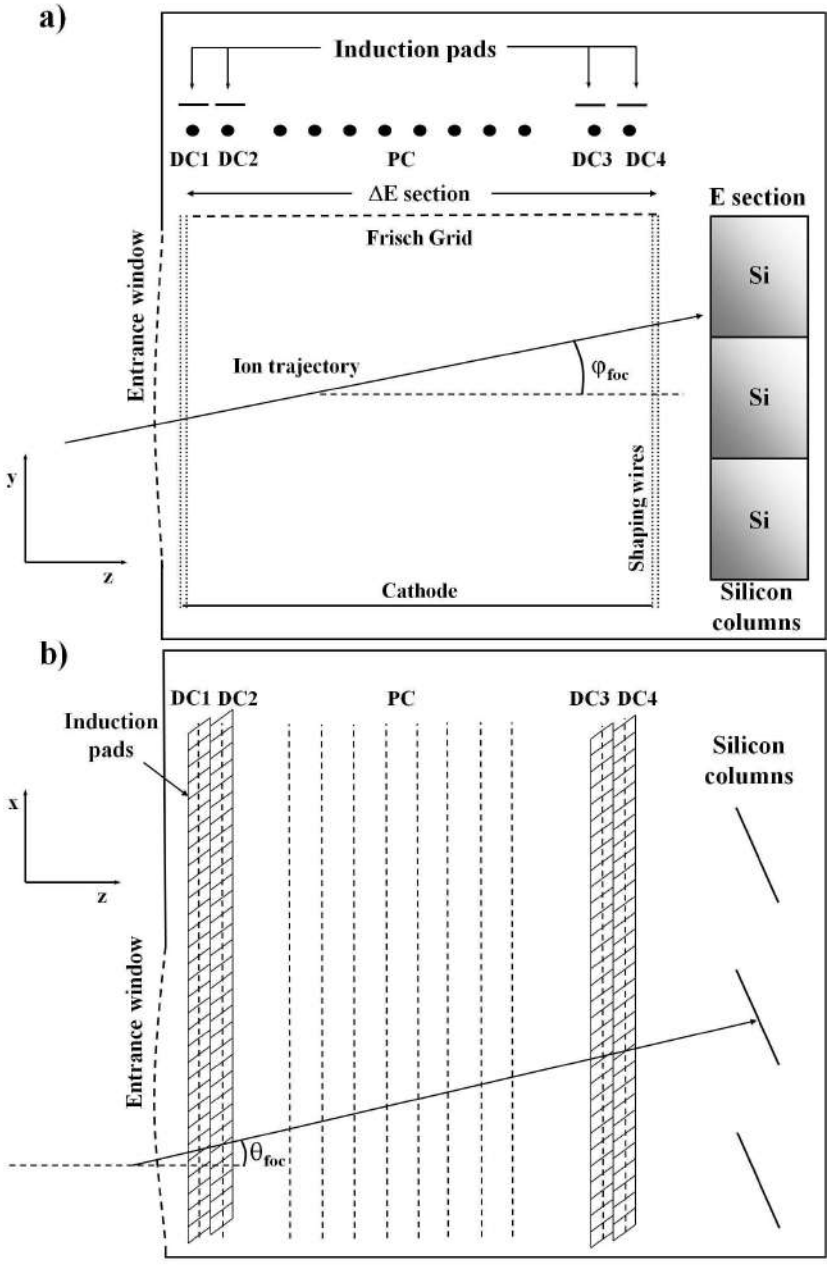

Figure 3.4: Schematic view of the Focal Plane Detector. a) - Side view. b) - Top view. Drift Counters (DC1-4) and Proportional Counters (PC) wires are used for measuring the energy lost in the gas. DC wires signal also measure the particle's horizontal and vertical positions. From [43]

.

from the final parameters, detected at the focal plane, and the magnetic fields. The motion of a charged particle beam under the action of a magnetic force can be represented as a general phase space mapping:

$$F : P_i(X_i, Y_i, \theta_i, \phi_i, d_i, \delta_i) \rightarrow P_{foc}(X_{foc}, Y_{foc}, \theta_{foc}, \phi_{foc}, d_{foc}, \delta_{foc}) \tag{3.1}$$

where the two last parameters are the trajectory length (d) and the fractional momentum (δ) relative to a reference momentum - taken as the central trajectory. In order to get the parameters at the target position, it is necessary to invert the previous equation, which formally corresponds to

$$F^{-1} : P_{foc}(X_{foc}, Y_{foc}, \theta_{foc}, \phi_{foc}, d_{foc}, \delta_{foc}) \rightarrow P_i(X_i, Y_i, \theta_i, \phi_i, d_i, \delta_i) \tag{3.2}$$

The central element in the trajectory reconstruction is to generate the high order direct and inverse transport matrix that connects $P_i \rightarrow P_{foc}$. This job is performed using the COSY INFINITY code [44, 45]. One of the key requirements of this technique is to achieve an appropriate description of the magnetic field for the purposes of the algebraic trajectory reconstruction. Our approach is to compare the measured parameters at the focal plane with the simulated ones, which represent a model of the spectrometer response. The first field model is produced based on values measured by Hall probes inside the quadrupole and dipole. Small adjustments performed to account for residual discrepancies between the real spectrometer and its model, as the known variation of the magnetic field geometry as a function of its strength, or the effect of slight misalignment of the real elements. Details about this procedure are presented in the next chapter.

This briefly shows that data volume to be processed in the analysis is significantly high. Additional information about the MAGNEX spectrometer and Focal Plane Detector can be found in abundance in literature, such as in [42, 43].

4 Data reduction

The success of the MAGNEX facility trustworthy measurements is strongly related to the use of a high acceptance spectrometer and a multiparameter detection, the MAGNEX itself and the FPD. In this section, an overview of the particle identification process and parameters correlation will be presented, followed by an outline of both simulation and reconstruction processes. Lastly, the obtained energy spectrum will be discussed, and integrated cross-sections will be presented for all reactions studied in this work, presented in Table 4.1.

Reactions	Central angle $\theta_{\text{lab}}^{\text{opt}}$
^{28}Si(^{16}O,^{17}F)^{27}Al	3°, 8°
^{27}Al(^{16}O,^{17}F)^{26}Mg	3°, 8°
^{28}Si(^{16}O,^{18}Ne)^{26}Mg	3°
^{27}Al(^{16}O,^{17}O)^{26}Al	8°
^{28}Si(^{16}O,^{18}F)^{26}Al	3°, 8°

Table 4.1: Datasets studied in this work, divided by reactions and central angle measured.

4.1 Identification

The process of ejectile identification consists in using two techniques: the standard ΔE-E, for atomic number (Z) identification, and a mass (A) identification technique for isotope separation.

The ΔE-E technique is a well-known procedure that explores the energy loss of heavy ions, based on the Bethe-Bloch formula [46]. Since the energy loss is proportional to the charge of the particle, and inversely proportional to its energy, it becomes possible to differentiate incident particles, initially by charge, then by Z, because it is assumed that all ejectiles are stripped of its electrons during the acceleration process in the MAGNEX facility. Particularly, the parameters observed in this analysis were E_{res}, the residual energy measured by the solid part of the FPD, and ΔE_{corr}, the energy lost by the ion in the gaseous part of the FPD, with a correction for the different incident angles in the focal plane. An illustrating plot can be found in Figure 4.1, left side.

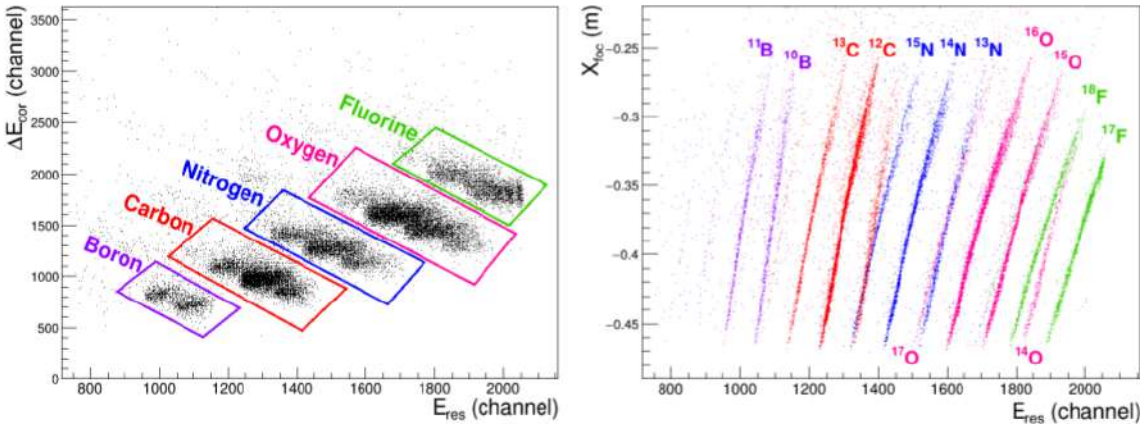

Figure 4.1: Two-dimensional plots for ^{16}O + ^{28}Si reaction for a single silicon detector. Left: $E_{res} \times \Delta E_{corr}$ plot with graphical selections indicating its respective atomic number, from Boron (Z=5) to Fluorine (Z=9). Right: $E_{res} \times X_{foc}$ plot indicating the different isotopes of Boron, Carbon, Nitrogen, Oxygen and Fluorine identified in this detector.

To perform a complete identification of the ejectiles, it was necessary to differentiate between isotopes of a single atomic number. For that, a mass identification technique for large acceptance spectrometers was introduced in [47]. This technique explores the movement of a charged particle in a magnetic field perpendicular to its momentum, and, considering a non-relativistic case, the momentum of the particle can be related to the residual energy E_{res} and the radius of the helical trajectory of the particle can be related to the position at the focal plane X_{foc}. This gives us an approximate relation between X_{foc} and E_{res}, shown in Equation 4.1. An example for the isotope differentiation is illustrated on Figure 4.1, right side.

$$x_{foc} \propto \frac{\sqrt{m}}{q}\sqrt{e_{resid}} \tag{4.1}$$

in which m and q are the mass and charge of the ejectile particle, respectively. Therefore, the identification process is done by plotting X_{foc} and E_{res}, as illustrated in Figure 4.1, and graphically selecting the isotope of interest corresponding data points.

Figures 4.2 and 4.3 exemplifies the typical identification process for a single detector. In Figure 4.2, the neutron transfer reaction in the ^{27}Al target was identified by selecting the corresponding ejectile for this process, ^{17}O. Usually, the selection starts at plotting $E_{res} \times \Delta E_{corr}$ and visually identifying the structure that corresponds to oxygen, since ^{16}O was the beam used in this experiment and, therefore, should be the most abundant in this

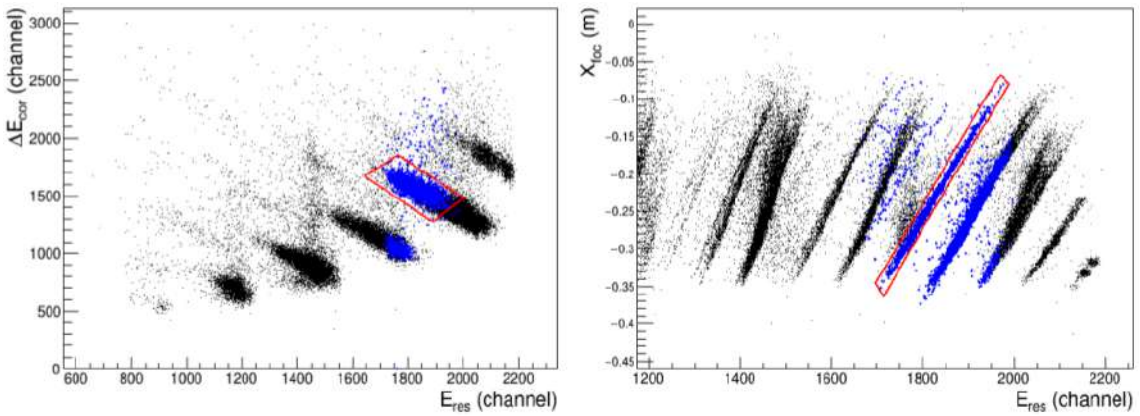

Figure 4.2: Typical two-dimensional plots for ^{16}O + ^{27}Al for a single silicon detector. Left: $E_{res} \times \Delta E_{corr}$ plot with a graphical cut (red rectangle) selecting events corresponding to the one-neutron transfer, and events in blue are the ones graphically selected in the right plot. Right: $E_{res} \times X_{foc}$ plot with a graphical cut (red rectangle) selecting events corresponding to the one-neutron transfer, and events in blue are the ones graphically selected in the left plot.

plot. This also makes the identification of other nuclei trivial, since the next structure parallel to the oxygen (Z=8) should correspond to a nucleus with Z=9, i.e. Fluorine, and so on. Once identified, the oxygen structure is graphically selected (red rectangle, left image, Figure 4.2) and $E_{res} \times X_{foc}$ is plotted with the previous graphical cut as condition, showing the selected events (in blue, right image, Figure 4.2) in $E_{res} \times X_{foc}$ plot. Then, one must identify ^{17}O amongst other oxygen isotopes by using Equation 4.1 to check the relative position of other isotopes in regarding the most abundant structure, which should be ^{16}O, and graphically selecting the correct one (red rectangle, right image, Figure 4.2). To guarantee a clean selection of events, the selection in E_{res} vs ΔE_{corr} plot is adjusted to constrain the events, using the selection in $E_{res} \times X_{foc}$ (in blue, left image, Figure 4.2). This whole process is then repeated for each of the sixty silicon detectors that contains the events of interest, individually, and repeated for each reaction one wishes to identify.

As part of a multiparameter analysis, other correlations between parameters can be checked to state the quality of the particle identification and the data set itself. Figure 4.4 shows typical plots, after particle identification, that need such inspection, for example. The right-side of Figure 4.4 shows an $X_{fit} \times Y_{fit}$ plot, and it indicates how the horizontal and vertical trajectories are focused according to the ions' momentum. The left-side of Figure 4.4 shows an $X_{fit} \times \theta_{foc}$ plot, in which the events correlated to the ^{17}F populated states are visible (curved structures where counts are more concentrated). X_{fit} is obtained

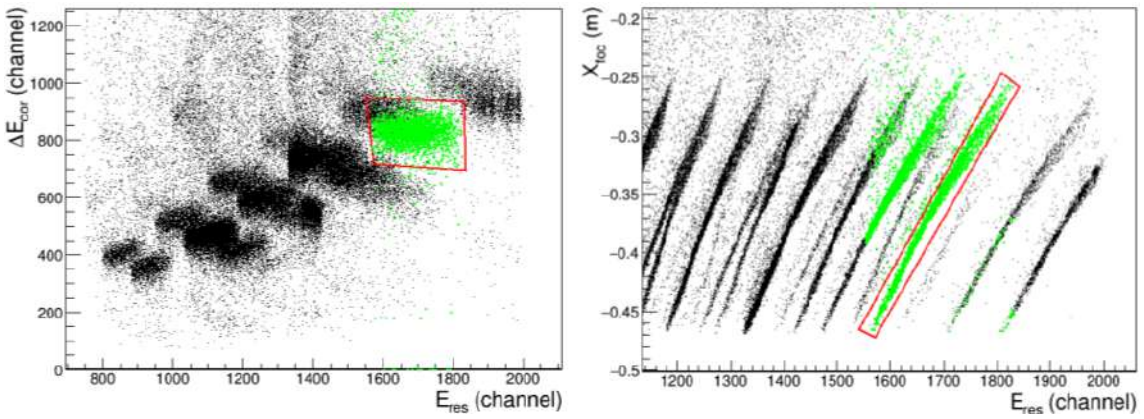

Figure 4.3: Typical two-dimensional plots for ^{16}O + ^{28}Si for a single silicon detector. Left: $E_{res} \times \Delta E_{corr}$ plot with a graphical cut (red rectangle) selecting events corresponding to the one-proton transfer, and events in green are the ones graphically selected in the right plot. Right: $E_{res} \times X_{foc}$ plot with a graphical cut (red rectangle) selecting events corresponding to the one-proton transfer, and events in green are the ones graphically selected in the left plot.

by fitting all four horizontal positions measured in each of the four DC wires (check Subsection 3.3) and its difference from the usual X_{foc} parameter is a slight translation in the x-axis, showing the same behavior as X_{fit}. The farthest structure to the right on this plot corresponds to the one-proton transfer in ^{28}Si that populates the ground state of ^{17}F and ^{27}Al, while the structures to its left correspond to the population of its excited states. Since the FPD has a 59.2° (1.033 rad) inclination with respect to the particle trajectory, θ_{foc} events will be distributed around this value. Also in this plot, kinematical effects and aberrations due to the nature of large acceptance spectrometry are evident. More details of such effects can be found in [48] and [49].

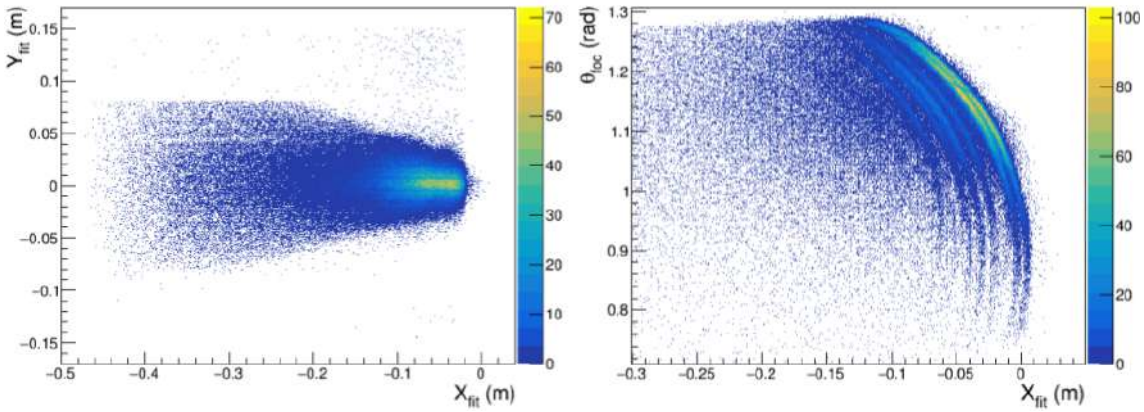

Figure 4.4: Typical two-dimensional plots for ^{28}Si(^{16}O,^{17}F)^{27}Al reaction, with the number of counts indicated by the color gradient shown. Left-side: $X_{fit} \times Y_{fit}$ plot. Right-side: $X_{fit} \times \theta_{foc}$ plot.

4.2 Simulation and trajectory reconstruction

Due to the presence of large optical elements in the large acceptance spectrometer, beam aberrations are inevitable. However, the approach of the MAGNEX was not to minimize such aberrations, but instead solve the equation of motion for the detected ions [48]. This was only possible due to the advances in mathematical techniques that allows the calculation of the transport map, which describes the evolution of the measured parameters from one frame of reference to the other[50]. Such technique allows obtaining the transport map up to high orders without requiring sophisticated ray-tracing methods. To become reality, information on the magnetic field distribution in the region between the target and the FPD is necessary, in addition to the boundary conditions at the focus, i.e. the measurements provided by the FPD.

Information on the magnetic field distribution is obtained through simulations of the transported particles, which require a defined transport map. The transport map not only includes information on the description of the magnetic field point-to-point and its aberrations, but also the geometric characteristics of the MAGNEX and FPD. The software COSY INFINITY [44] is used to obtain such transport map by making a geometric interpolation of the point-to-point magnetic field. In its input, the dipole and quadrupole magnetic strengths are defined, using the central probe measurement during the experiment as starting point. In addition, the dipole's boundaries were parametrized, and together with the magnetic rigidity Bρ, are the parameters modified to tune the simulation with the experimental data.

To check the transport map quality, a simulation of the events of interest is done using Monte Carlo routines [51]. This process is performed for each interested reaction, and inputting recoil and/or ejectile states to better tune the experimental data with the simulated data.

Another required parameter to perform the simulation is the ^{16}O beam energy input value. Because the thickness of the target is not negligible, both projectile and ejectile lose energy when going through it, and this simulation does not take into consideration such energy loss. In order to qualitatively add this effect, an estimation of the average effective beam energy is performed using the programs CATKIN [52] and SRIM-2013

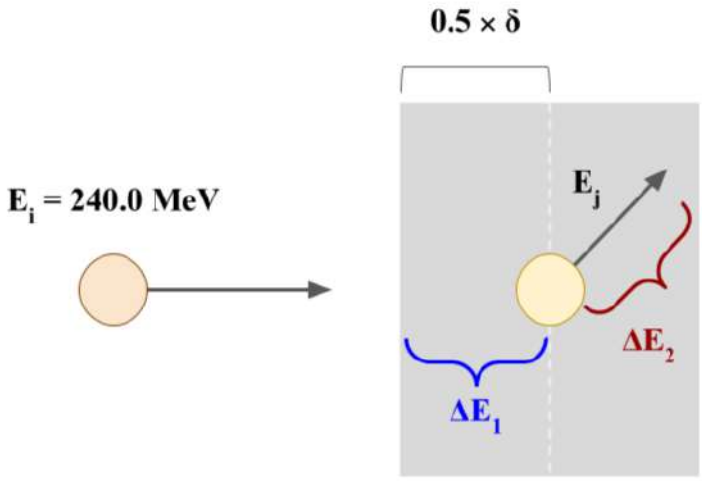

Figure 4.5: Average energy calculation scheme. E_i is the beam energy and E_f is the ejectile energy. ΔE_1 and ΔE_2 are the particle's energy losses before and after the reaction, respectively. δ is the target's thickness.

[53]. In this estimation, we consider that the reaction occurs in the middle of the target, as illustrated in Figure 4.5. Therefore, the energy loss of the projectile when entering the target is given by $\Delta E_1 = 0.5 \cdot \delta \cdot S_p(E_i)$, where δ is the target thickness reported in Subsection 3.2. The stopping power $S_p(E_i)$ was calculated by interpolating stopping power values ranged from 100-300 MeV obtained from the SRIM code for the $E_i = 240$ MeV. The ejectile energy is then obtained by simply subtracting $E_j = E_i - \Delta E_1$, which is used to calculate the energy loss of the ejectile, ΔE_2. After the reaction has occurred, it is assumed that the ejectile was scattered at the central angle θ_{lab}^{opt}, and ΔE_2 is obtained analogously using $\Delta E_2 = 0.5 \cdot \delta \cdot S_p(E_j) \cdot \sec\theta_{lab}^{opt}$. The stopping power $S_p(E_j$ is obtained using the same method previously explained, but interpolated for E(j). Finally, the final average effective beam energy, considering such energy loss, was obtained by finding the beam energy entry in the CATKIN software that matches $E_j - \Delta E_2$ at θ_{lab}^{opt}.

Reactions	Average energy (MeV)	
	3°	8°
^{28}Si(^{16}O,^{17}F)^{27}Al	239.70	239.70
^{27}Al(^{16}O,^{17}F)^{26}Mg	239.83	-
^{28}Si(^{16}O,^{18}Ne)^{26}Mg	239.65	-
^{27}Al(^{16}O,^{17}O)^{26}Al	239.85	239.85
^{28}Si(^{16}O,^{18}F)^{26}Al	239.69	239.70

Table 4.2: Effective average energy values obtained for the reactions studied in this work.

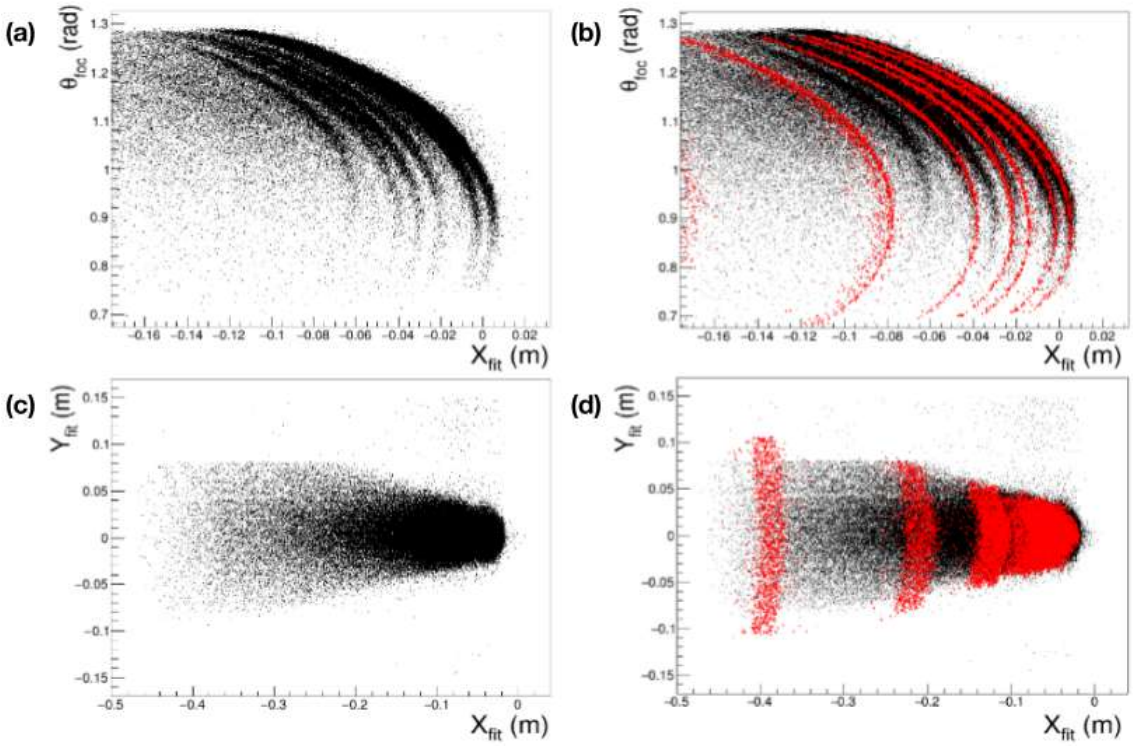

Figure 4.6: Comparison between experimental data and simulated events in ^{28}Si(^{16}O,^{17}F)^{27}Al reaction. Figures (a) and (b) are $X_{fit} \times Y_{fit}$ plots. Figures (c) and (d) are $X_{fit} \times \theta_{foc}$ plots. The simulated events are represented by the red points in the left-side images (Figures (b) and (d)).

Although a considerable number of parameters are used to fine tune the simulations with the experimental data, one distinct feature in this data analysis is the use of the same magnetic model to describe the experimental data of many reactions, exploring a large space of the FPD response. These groups were analyzed by central angle and region in the X_{fit} axis. For each central angle (3° and 8°), all reaction channels used the same values for the Bρ and quadrupole field. Datasets that were measured in the same region on the focal plane were described using the same dipole boundary profiles. The consistent use of a reduced number of parameters to describe all datasets makes this analysis more trustworthy.

Qualitatively, the reconstruction process should rebuild the trajectory of the particles point by point from the detector to the target. However, the trajectory reconstruction is based on the calculation of high order transport maps, and this process is mathematically equivalent to change the frame of reference. That said, the COSY INFINITY allows inverting the transport matrices in order to obtain the coordinates in the target's reference frame from the final measured parameters, and without the necessity to minimize

aberrations, because they are taken into account in the calculation. The parameters obtained after the reconstruction are the vertical and horizontal angles at the target point ϕ_i and θ_i, vertical and horizontal positions at the target point X_i and Y_i, scattered angle in the laboratory frame θ_{lab}, and the excitation energy E_x. These parameters will lead to the physical quantities of interest for this analysis. One important aspect for the

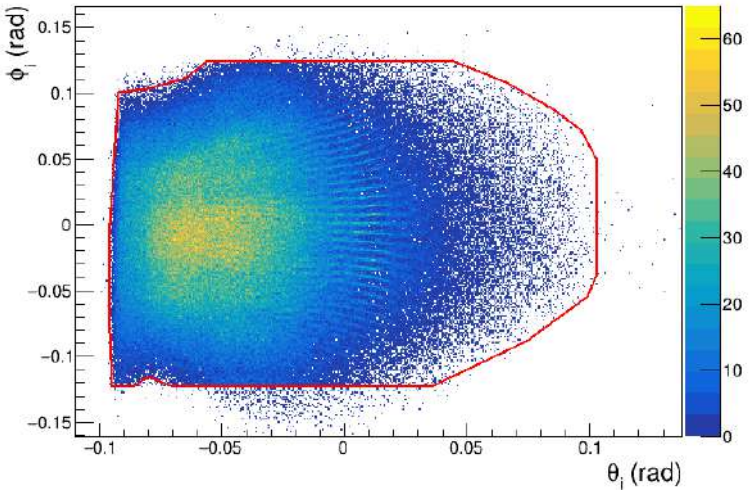

Figure 4.7: Typical plot with reconstructed parameters ϕ_i and θ_i for the ^{28}Si(^{16}O,^{17}F) reaction, with the number of counts indicated by the color gradient shown. The red line contour in the events represents the spectrometer solid angle full acceptance.

trajectory reconstruction is that the program will not always successfully reconstruct all events, resulting in the discard of events that should have been valid. This efficiency loss [54] is considered when extracting the cross-sections, which will be detailed further.

In Figures 4.7 and 4.8 reconstructed events are shown for the proton transfer in ^{28}Si target dataset at $\theta_{lab}^{opt} = 3°$. Figure 4.7 shows the vertical and horizontal angles at the target point, $\phi_i \times \theta_i$, which will be used to obtain the solid angles in further sections. Figure 4.8 shows the scattered angle in the laboratory frame and the excitation energy, $\theta_{lab} \times E_x$. The almost vertical structures show states of the ejectile and/or recoil nuclei.

However, this inclination on the events may result in an erroneous spectrum when an angular selection in $\theta_{lab}$is made, and the counts are projected onto E_x, in order to obtain excitation energy spectra. This inclination can be better perceived in Figure 4.8-b, when the plot is zoomed in, and it was due to a poor measurement of ϕ_i. An empirical correction was then performed using a polynomial function of ϕ_i to adjust E_x in the $\phi_i \times E_x$ plot, and the results are shown in Figure 4.9. Figure 4.9-a shows the plot without any correction,

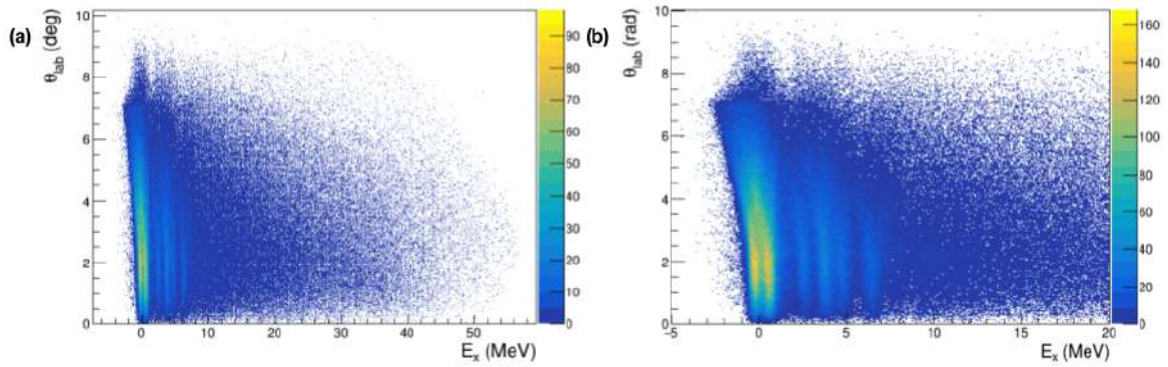

Figure 4.8: Typical plot with reconstructed parameters θ_{lab} and E_x for the ^{28}Si(^{16}O,^{17}F)^{27}Al reaction, with the number of counts indicated by the color gradient shown. The left-side image is the same as the left-side one, but with the x-axis zoomed in for better visualization.

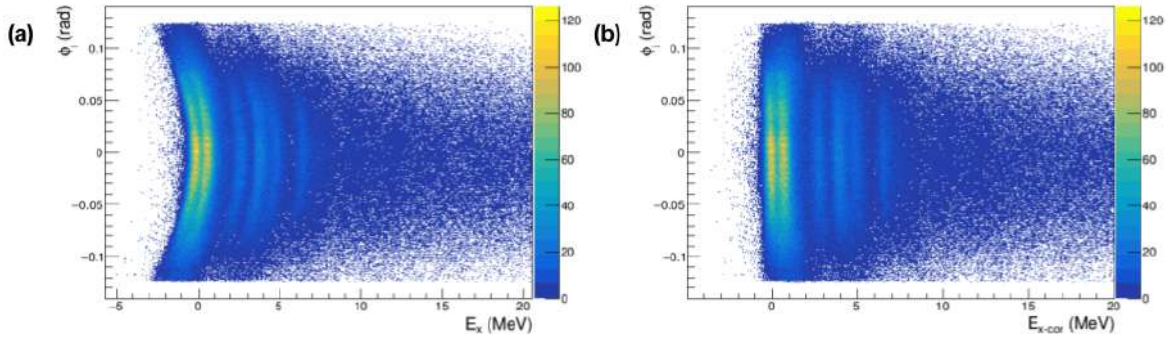

Figure 4.9: Typical plot with reconstructed parameters ϕ_i and excitation energy for the ^{28}Si(^{16}O,^{17}F)^{27}Al reaction, with the number of counts indicated by the color gradient shown, before and after correction. The right-side image shows the plot for the corrected excitation energy $E_{\text{x-corr}}$

in which the almost parabolic curvature can be seen in the events. Figure 4.9-b shows the same plot, but as function of the corrected excitation energy, in which the correlated events that correspond to states of ejectiles and recoil nuclei, ^{17}F and ^{27}Al in this dataset, showing the expected linear relation between ϕ_i and $E_{\text{x-corr}}$. This results in the corrected plots for θ_{lab} and $E_{\text{x-corr}}$ shown in Figure 4.10, which were used to generate excitation energy spectra, shown in Figure 4.11.

The identification and reconstruction procedures were then applied to all data sets analyzed in this work, shown in Table 4.1. Typical spectra for the ^{28}Si(^{16}O,^{17}F)^{27}Al, ^{27}Al(^{16}O,^{17}F)^{26}Mg and ^{27}Al(^{16}O,^{17}Ne)^{26}Mg reactions are shown in Figure 4.11, with its corresponding angular selection indicated in each panel. The full width at half-maximum for each histogram is also indicated, and were obtained by fitting a sum of Gaussians representing states of both recoil and ejectile nucleus for each process. This shows that

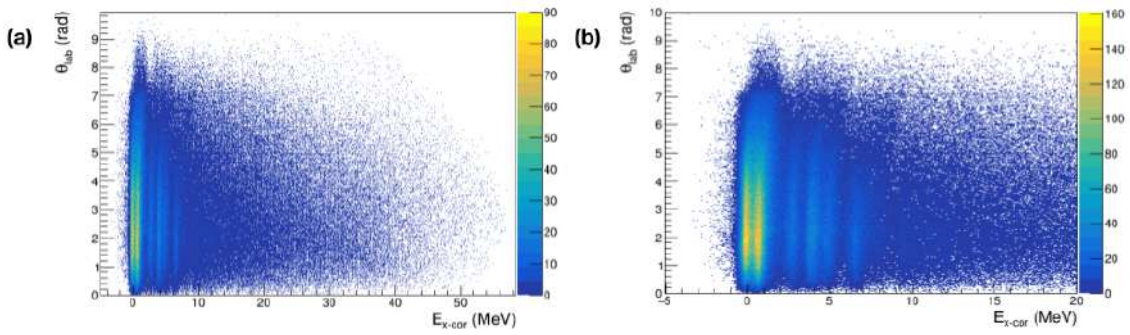

Figure 4.10: Typical plot with reconstructed parameters θ_{lab} and $\mathrm{E_x}$, with an excitation energy correction, for the ^{28}Si(^{16}O,^{17}F)^{27}Al reaction, with the number of counts indicated by the color gradient shown. The left-side image is the same as the left-side one, but with the x-axis zoomed in for better visualization.

an energy resolution of about 0.7 MeV was achieved in this work. The adjusting is further discussed in the next section.

4.3 Integrated cross-section

For a better comparison, the excitation energy spectrum are presented as integrated cross-sections as function of excitation energy. The integrated cross-section was obtained by calculating the cross-section bin by bin in each energy spectrum and then integrating for the corresponding angular range. Generally, the experimental cross-section for each process is defined as:

$$\frac{d\sigma}{d\Omega}(\theta) = \frac{N_{\mathrm{counts}}(\theta)}{N_{\mathrm{beam}}\, N_{\mathrm{target}}\, \Delta\Omega(\theta)\, t_{\mathrm{live}}\, \epsilon} \tag{4.2}$$

where N_{counts} is the number of counts at an angle θ, N_{beam} is the number of incident particles, N_{target} is the number of target nuclei per surface area, $\Delta\Omega$ is the solid angle associated with the detection system, t_{live} is the live time of the detector and ϵ is an efficiency factor.

The number of counts at an angle θ is stored in each bin, and, therefore, the cross-section is calculated for each bin. N_{beam} is obtained through the measurement of the total integrated charge $\mathrm{Q_{raw}}$ by a Faraday cup during the experiment. The beam energy in these measurements was high enough that the ^{16}O ions detected in the FPD are stripped of its electrons. Then, N_{beam} is obtained through the relation $N_{\mathrm{beam}} = \mathrm{Q_{raw}}/\mathrm{Z_{ej}}\, e$, where $\mathrm{Z_{ej}}$

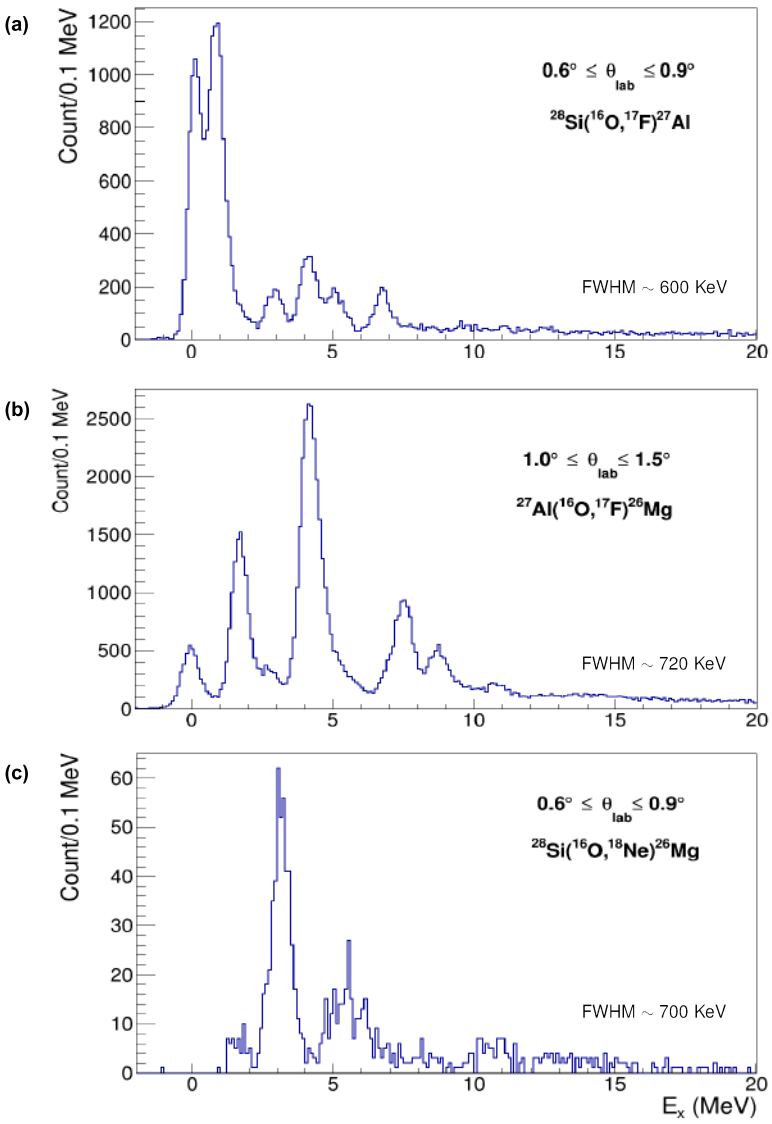

Figure 4.11: Typical angular excitation spectrum for the p-transfer in ^{28}Si (panel a), the p-transfer in ^{27}Al (panel b) and the 2p-transfer in ^{28}Si (panel c), all with $\theta_{\mathrm{lab}}^{\mathrm{opt}} = 3°$. The full width at half maximum for each histogram is shown.

is the atomic number of the ejectile, and e is the elementary charge. N_{target} is calculated from the known target density and thickness, mentioned in Section 3. The live time t_{live} is calculated by the ratio between the number of events processed by the FPD ($\mathrm{FPD_{live}}$), and the total events acquired by the FPD ($\mathrm{FPD_{raw}}$), including the ones that triggered the electronic and could not be processed. Both $\mathrm{FPD_{live}}$ and $\mathrm{FPD_{raw}}$ are measured during the data acquisition.

The solid angle was determined geometrically by calculating the area defined by the interval θ_{lab}, $\theta_{\mathrm{lab}} + \Delta\theta_{\mathrm{lab}}$ in the $\phi_{\mathrm{i}} \times \theta_{\mathrm{i}}$ plot, exemplified in Fig. 4.7. Figure 4.12 illustrates the procedure for this calculation. The hatched region in Fig. 4.12 corresponds to the

Target	$\mathbf{N_{target}}$ (10^{18}cm^{-2})	$\theta_{\text{lab}}^{\text{opt}}$	**Integrated charge** (μ**C**)	t_{live} (%)
^{28}Si	3.18	3°	136.00	68.8
		8°	8.24	83.7
^{27}Al	1.98	3°	35.30	63.3
		8°	9.14	83.4

Table 4.3: Obtained values for the integrated charge collected by the Faraday cup, the number of nuclei in the target per surface area and the percentage of live time for the detector in each dataset evaluated in this work.

selected angular bin, which area will be the solid angle for a defined angular interval. This procedure results in obtaining the solid angles with approximately 2% uncertainty, which was estimated by varying 0.2° in θ_{lab}, recalculating the solid angle, and comparing with the results for the intended θ_{lab}.

The efficiency factor ϵ takes into account the detection efficiency and loss of events due to a bad reconstruction of events. The FPD efficiency is estimated around ∼90% and the reconstruction efficiency was obtained as the ratio of the well reconstructed events and the total events for each process and each chosen angular interval.

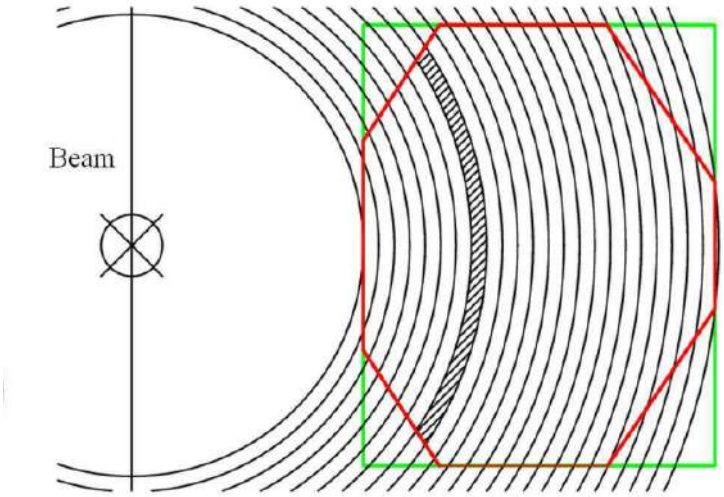

Figure 4.12: Solid Angle calculation scheme representing ϕ_{i} and θ_{i} contour in space. The effective spectrometer angular acceptance is indicated by the red solid line, and the spectrometer diaphragm aperture is indicated by the green solid line. The solid angle is obtained by calculating the area of the hatched region, which is defined by the interception between the circular ring θ_{lab}, $\theta_{\text{lab}} + \Delta\theta_{\text{lab}}$ interval and the effective spectrometer aperture. Modified from [43]

Finally, after obtaining the cross-section for each defined energy bin and angular bin, the

cross-sections were summed for a chosen angular range in order to obtain the integrated cross-sections as function of the excitation energy. The results of this procedure for each process listed in Table 4.1 are shown in Figs.4.13, 4.14 and 4.15. For each presented spectrum, a set of Gaussian curves were fitted to the experimental data, in order to reproduce target-like and projectile-like well-known states. The width of all Gaussian curves were set to be adjusted between an interval that reproduces the experimental resolution. The amplitude of the Gaussian curves were set as an adjustable parameter with the only restriction of being positive. The sum of such curves is represented as a red solid curve in each spectrum. The most populated individual states in the adjustment are labeled in each figure.

Figure 4.13 presents the results for the neutron pickup for the ^{27}Al target (panel a) and the deuteron pickup for the ^{28}Si target (panels b and c). Fig. 4.13-a shows that the low-lying states for the n-transfer reaction are well populated. Also, it shows that the ground-to-ground one-neutron transfer is predominant. In this fitting model, the predominant excited states are ^{26}Al states (green dotted lines) and only the 0.871 MeV ^{17}O state is visible (cyan dashed line). Fig. 4.13-b and Fig. 4.13-c shows the deuteron transfer data, and, although both n-transfer and d-transfer result in the same ^{26}Al nucleus, their spectra are not alike. The ground state for this process is clearly highly suppressed for both angular regions shown in this work. It is also noticeable that the deuteron transfer populates predominantly excited states between 1.100 and 2.100 MeV of ^{18}F and ^{26}Al, which are detailed in Table 4.4, according to the labels in Fig. 4.13.

In Figure 4.14, the results for the proton pickup in the ^{27}Al (panel a) and ^{28}Si (panel b) targets with central angle 8° are shown. These spectra show that the one proton transfer favors the population of low-lying nuclear states of both target-like and projectile-like nuclei, also seen in the one neutron transfer in Fig. 4.13-a. Considering the description of the deuteron transfer (Fig. 4.13 b and c) as a sequential transfer of one proton (Fig. 4.14-b) followed by one neutron (Fig. 4.13-a), as discussed in Section 1, the one-nucleon processes seem to populate the ground-to-ground transfer, while the two-nucleon (deuteron) transfer does not favor the population of the ground states of ^{18}F and ^{26}Al. Quantitatively, the estimated integrated cross-section for the ground state in the ^{28}Si(^{16}O,^{17}F)^{27}Al reaction is 1.46(15) mb and in the ^{27}Al(^{16}O,^{17}O)^{26}Al reaction

Peak label	Nuclei	Excitation energy (keV)[55]	J^{π}[55]
0.228	^{26}Al	228.31	0^+
0.416	^{26}Al	416.85	3^+
0.871	^{17}O	870.76	$1/2^+$
1.057	^{26}Al	1057.74	1^+
1.121	^{18}F	1121.36	5^+
1.700	^{18}F	1700.81	1^+
1.850	^{26}Al	1850.62	1^+
2.069	^{26}Al	2068.86	4^+
2.069	^{26}Al	2069.47	2^+
2.069	^{26}Al	2071.64	1^+
2.100	^{18}F	2100.61	2^-
2.660	^{26}Al	2660.92	2^+

Table 4.4: List of nuclear states in ^{18}F, ^{26}Al and ^{17}O states observed in n-pickup reaction with ^{27}Al target and d-pickup reaction with ^{28}Si target. The peaks as labeled are shown in Figure 4.13.

is 1.03(10) mb, while the estimated integrated cross-section for the ground state in the ^{28}Si(^{16}O,^{18}F)^{26}Al reaction is 5 μb for $4.0^\circ \leq \theta_{\rm lab} \leq 8.0^\circ$ and 10 μb for $0.0^\circ \leq \theta_{\rm lab} \leq 6.0^\circ$.

In Figure 4.15 the results for the one-proton pickup in the ^{28}Si (panel a) and ^{27}Al (panel b) targets, and the two-proton pickup in the ^{28}Si target (panel c) are presented. For both p-transfer reactions (panels a and b), the low-lying states of ^{17}F, ^{27}Al and ^{26}Mg are decently populated. Results for the same processes measured at $\theta_{\rm lab}^{\rm opt} = 8^\circ$ have been shown in Figure 4.14, and the same characteristics are seen in both measurements with different central angle. Figs. 4.15-a and 4.14-b present the results for the ^{28}Si(^{16}O,^{17}F)^{27}Al reaction, which also populates low-lying states. In both spectra, the ground-to-ground state is the most populated and the same excited states (see Table 4.5) are populated in both datasets, according to the utilized fitting model. In Figs. 4.15-b and 4.14-a, the ^{27}Al(^{16}O,^{17}F)^{26}Mg populates mostly ^{26}Mg states (green dotted lines), which is expected since the density of nuclear states per energy in this nucleus is large for the energy range considered in this Gaussian fitting model. In both spectra, the 1.809 and 2.938 ^{26}Mg states are prominent, as well as the ground-to-ground state and a considerable number

of states with $E_x \geq 3.0$ MeV, as labeled in the figures and detailed in Table 4.5.

Finally, Fig. 4.15-c presents the results for the two-proton pickup in the ^{28}Si target. Firstly, it is important to notice that this integrated cross-section is reported in μb, while all other results were reported in mb, showing the discrepancy in the cross-sections value for this process. Secondly, the two proton transfer does not favor the population of the ground-to-ground transfer process, similar to what the deuteron transfer has shown. For this fitting model, the most prominent state is the 3.376 ^{18}Ne state (cyan dashed line), while a few states of ^{26}Mg can also be seen (green dotted lines).

The one-proton transfer results presented in 4.15-b and 4.14-a lead to the same final nucleus as the two-proton transfer, ^{26}Mg, however their spectra are not alike. Considering the description of the two-proton transfer (Fig. 4.15-c) as a sequential transfer of one proton leading to ^{27}Al (Fig. 4.15-a) followed by another proton transfer, now leading to ^{26}Mg (Fig. 4.15-b), as discussed in Section 1, both one-proton processes seem to favor the population of the ground-to-ground transfer and both target-like and projectile-like nuclear states, while the two-proton transfer does not favor the population of the ground states of ^{18}Ne and ^{26}Mg. This conclusion is very similar to that of the deuteron transfer and its sequential one-nucleon transfers. Quantitatively, the estimated integrated cross-section for the ground state in the ^{28}Si(^{16}O,^{17}F)^{27}Al reaction is 2.06(21) mb, for $0.0^\circ \leq \theta_{\text{lab}} \leq 5.1^\circ$, and in the ^{27}Al(^{16}O,^{17}F)^{26}Al reaction is 1.26(13) mb, for $0.0^\circ \leq \theta_{\text{lab}} \leq 7.0^\circ$, while the estimated integrated cross-section for the ground state in the ^{28}Si(^{16}O,^{18}Ne)^{26}Mg reaction is 0.06 μb for $0.0^\circ \leq \theta_{\text{lab}} \leq 4.2^\circ$. For the 1.809 ^{26}Mg state, the estimated integrated cross-section in the ^{27}Al(^{16}O,^{17}F)^{26}Al reaction is 3.11(31) mb, for $0.0^\circ \leq \theta_{\text{lab}} \leq 7.0^\circ$, and in the ^{28}Si(^{16}O,^{18}Ne)^{26}Mg reaction is 5 μb for $0.0^\circ \leq \theta_{\text{lab}} \leq 4.2^\circ$.

In sum, for the processes analyzed in this work, the one-nucleon transfers favor the population of ground-to-ground transfer reactions and contrasts with the results of the two-nucleon transfers, which does not favor the ground state population at all. Also, the excited states for processes leading to the same final nucleus are not equally populated in these processes. These arguments lead to the conclusion that the two-nucleon transfers selectively populate a few states, differently than its one-nucleon counterparts. Therefore, an investigation of the nuclear structure nature of these states and reaction mechanisms is required to obtain trustworthy conclusions, in special through the comparison of

Peak label	Nuclei	Excitation energy (keV)[55]	J^{π}[55]
0.495	^{17}F	495.33	$1/2^+$
0.844	^{27}Al	843.76	$1/2^+$
1.015	^{27}Al	1014.56	$3/2^+$
1.339	$^{17}F_{1/2^+} + {}^{27}Al_{1/2^+}$	495.33 + 843.76	-
1.510	$^{17}F_{1/2^+} + {}^{27}Al_{3/2^+}$	495.33 + 1014.56	-
1.808	^{26}Mg	1808.74	2^+
2.303	$^{17}F_{1/2^+} + {}^{26}Mg_{2^+}$	495.33 + 1808.74	-
2.735	^{27}Al	2734.90	$5/2^+$
2.938	^{26}Mg	2938.33	2^+
2.982	^{27}Al	2982.00	$3/2^+$
3.376	^{18}Ne	3376.20	4^+
3.857	^{17}F	3857.00	$5/2^-$
3.942	^{26}Mg	3941.57	3^+
4.319	^{26}Mg	4318.89	4^+
4.333	^{26}Mg	4332.52	2^+
4.350	^{26}Mg	4350.09	3^+
5.000	^{17}F	5000.00	$3/2^+$

Table 4.5: List of nuclear states in ^{17}F, ^{27}Al, ^{26}Mg and ^{18}Ne states observed in p-pickup reaction with ^{27}Al ^{28}Si targets and 2p-pickup reaction with ^{28}Si. The peaks as labeled are shown in Figure 4.15 and Figure 4.14.

experimental data and theoretical calculations. Theoretical descriptions of the one- and two-proton reactions are presented in Section 5.

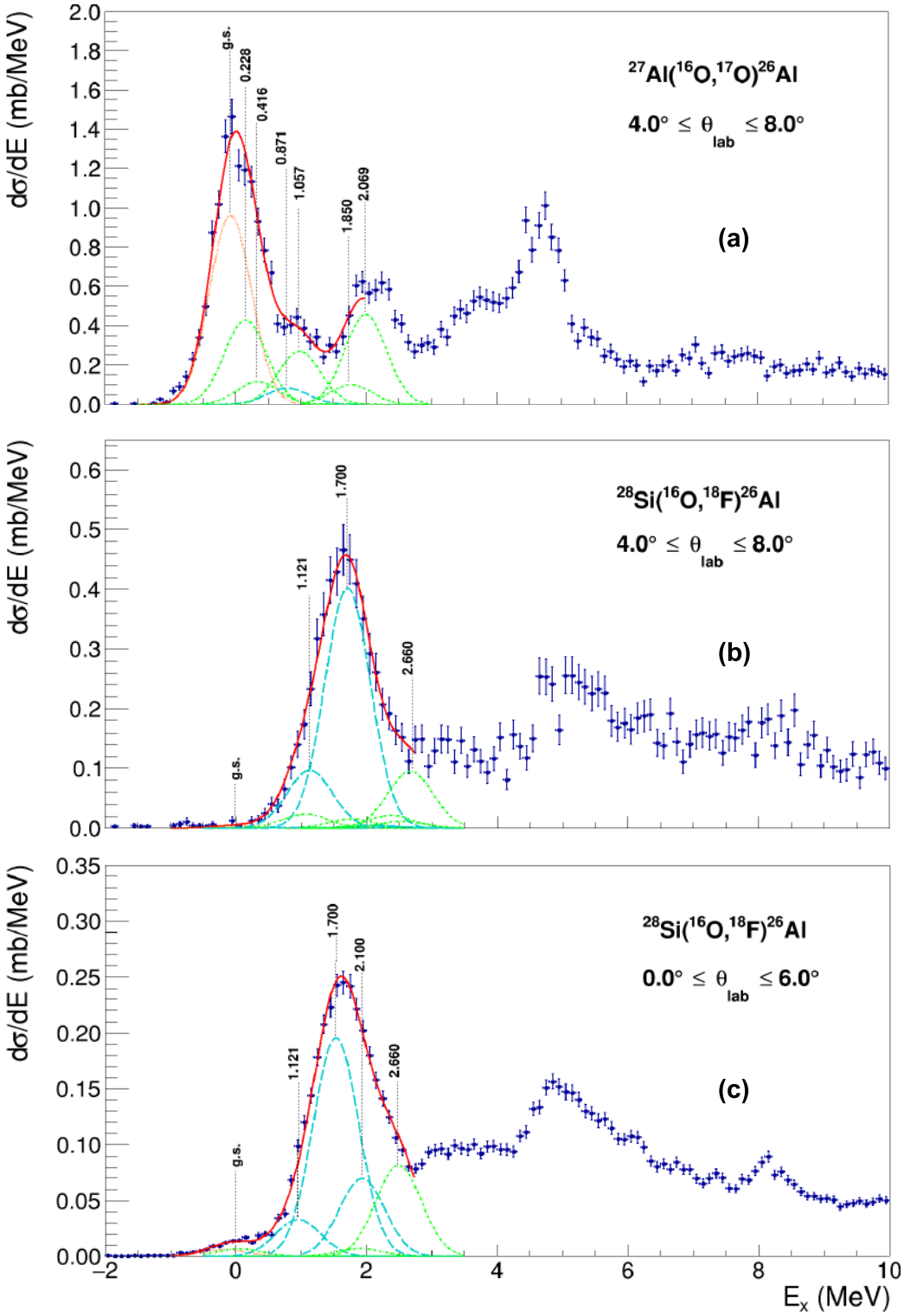

Figure 4.13: Integrated cross-section as a function of excitation energy for the n-transfer in ^{27}Al (panel a), the d-transfer in ^{27}Al (panel b), both with $\theta_{\text{lab}}^{\text{opt}} = 3°$, and the d-transfer in ^{28}Si with $\theta_{\text{lab}}^{\text{opt}} = 8°$ (panel c). Energy spectra are reproduced by adjusted Gaussian curves that reproduce nuclear states. Orange dotted lines represent both ejectile and recoil nucleus in their ground state, cyan dashed lines represent states of the ejectile nucleus, green dotted lines represent states of the recoil nucleus, and the red solid line represents the sum of shown states. The most prominent states in these Gaussian fits are labeled according to Table 4.4.

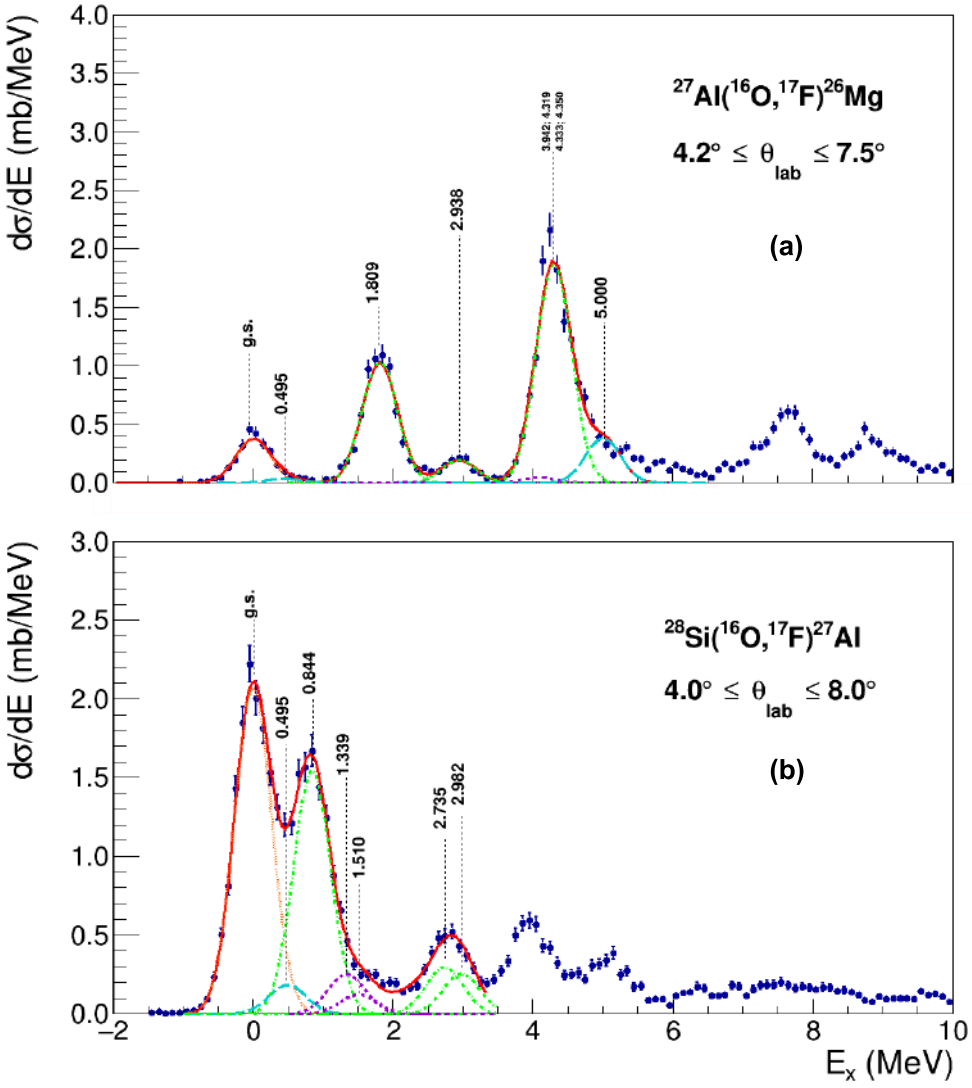

Figure 4.14: Integrated cross-section as a function of excitation energy for the p-transfer in ^{27}Al (panel a), and the p-transfer in ^{28}Si (panel b), all with $\theta_{\text{lab}}^{\text{opt}} = 8°$. Energy spectra are reproduced by adjusted Gaussian curves that reproduce nuclear states. Orange dotted lines represent both ejectile and recoil nucleus in their ground state, cyan dashed lines represent states of the ejectile nucleus, green dotted lines represent states of the recoil nucleus, purple dashed lines represent states where both ejectile and recoil nuclei are excited, and the red solid line represents the sum of shown states. The most prominent states in these Gaussian fits are labeled according to Table 4.5.

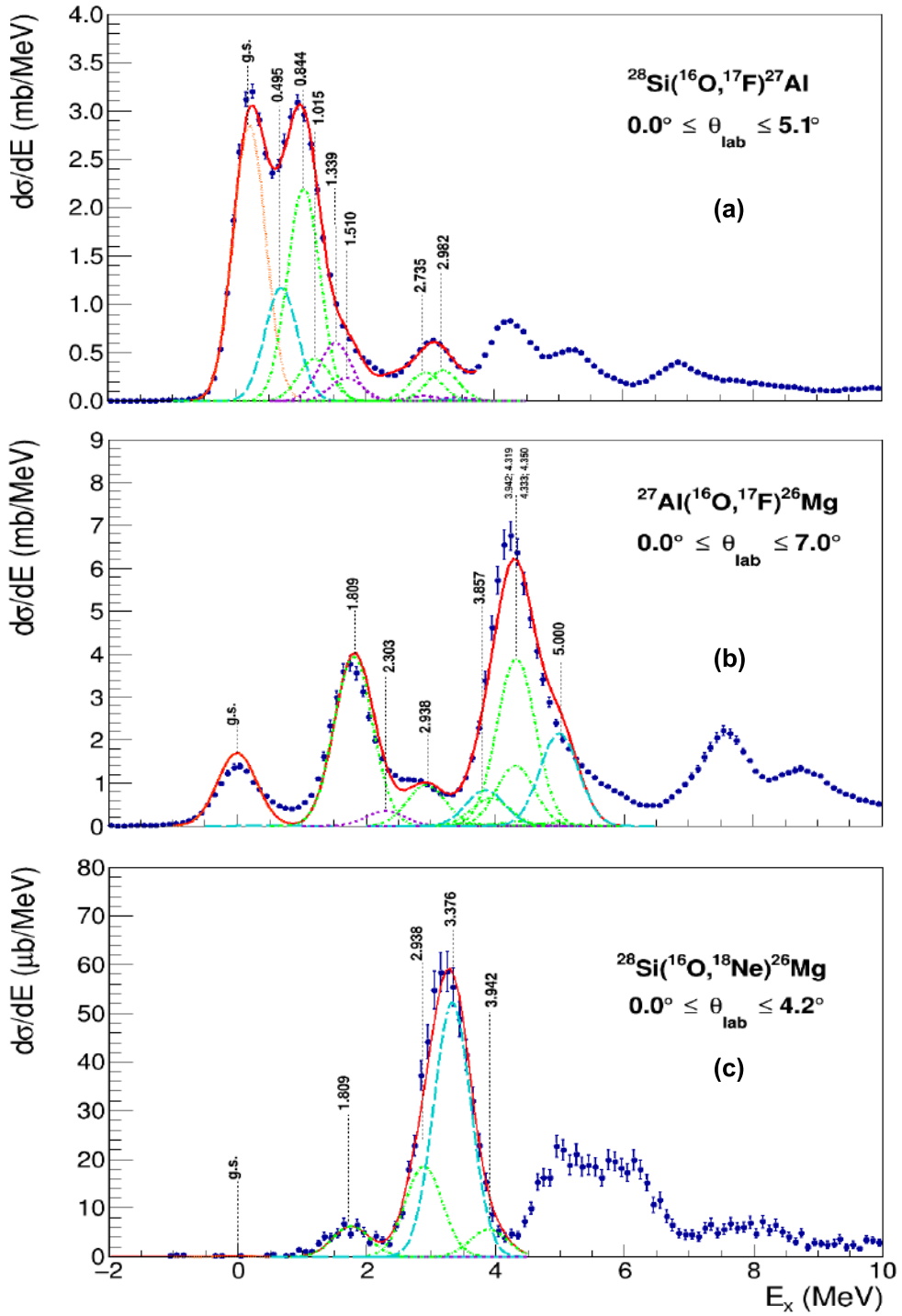

Figure 4.15: Integrated cross-section as a function of excitation energy for the p-transfer in ^{28}Si (panel a), the p-transfer in ^{27}Al (panel b), and the 2p-transfer in ^{28}Si (panel c), all with $\theta_{\text{lab}}^{\text{opt}} = 3°$. Energy spectra are reproduced by adjusted gaussian curves that reproduce nuclear states. Orange dotted lines represent both ejectile and recoil nucleus in their ground state, cyan dashed lines represent states of the ejectile nucleus, green dotted lines represent states of the recoil nucleus, purple dashed lines represent states where both ejectile and recoil nuclei are excited, and the red solid line represents the sum of shown states. The most prominent states in these gaussian fits are labeled according to Table 4.5.

5 Results and discussion

In this section, we present the results for the angular distribution of the cross-sections for the one-proton transfer in the ^{27}Al and ^{28}Si targets, and the two-proton transfer in the ^{28}Si target. For a consistent theoretical interpretation of the data, it is of paramount importance to revisit the elastic scattering. Also, additional reaction channels, observed in the same experimental campaign, provide some guidance on the shell model to be adopted to describe the residual nuclei.

Therefore, in this chapter, I start revisiting the elastic scattering and the one-neutron transfer reactions. The results for the elastic scattering were published in [3] and the one-neutron stripping in the ^{27}Al and ^{28}Si targets have been accepted in Phys. Rev. C [56]. Both previous contributions were crucial for the success of this analysis, providing parameters used in the calculations presented in this work.

5.1 Elastic channel within the CRC calculations

The methodology followed by the theoretical calculations have been discussed in Section 2. CRC calculations require a few ingredients that can be adjusted for the experimental data presented, such as the optical potential (both in the initial and final mass partitions), the binding potential and the spectroscopic amplitudes. Nevertheless, to keep the spirit of a systematic analysis, we explore an experimental-based multichannel approach, in which many reaction channels set constraints to the calculations. Some of these ingredients were extracted from the elastic scattering and neutron stripping measured in this same campaign.

For the optical potential, we used the São Paulo Potential, detailed in Subsection 2.3. The SPP uses matter densities described as two-parameter Fermi distributions with matter radius defined as $R_m = 1.31A^{1/3} - 0.84$ fm, and matter diffuseness equal to $a_m = 0.56$ fm. These values were obtained in a systematic study of many nuclei [35]. In the analysis of the elastic and inelastic scattering data for the ^{27}Al + ^{16}O and the ^{28}Si + ^{16}O systems [3], it has been shown that the best agreement with CRC calculations and experimental data requires:

- increasing the matter diffuseness to $a_m = 0.62$ fm in the double-folding São Paulo potential for both ^{27}Al and ^{28}Si nuclei
- the imaginary term was set to $N_i = 0.6$, for the ^{27}Al + ^{16}O, and $N_i = 0.7$, for the ^{28}Si + ^{16}O systems

The larger matter diffuseness is an effective procedure to take into account the static deformation exhibited by these nuclei in their ground state. The smaller strength of the imaginary term of the optical potential is anticipated since the systematic value $N_i = 0.78$, obtained in a systematic optical model calculation [35], does not include inelastic channels explicitly.

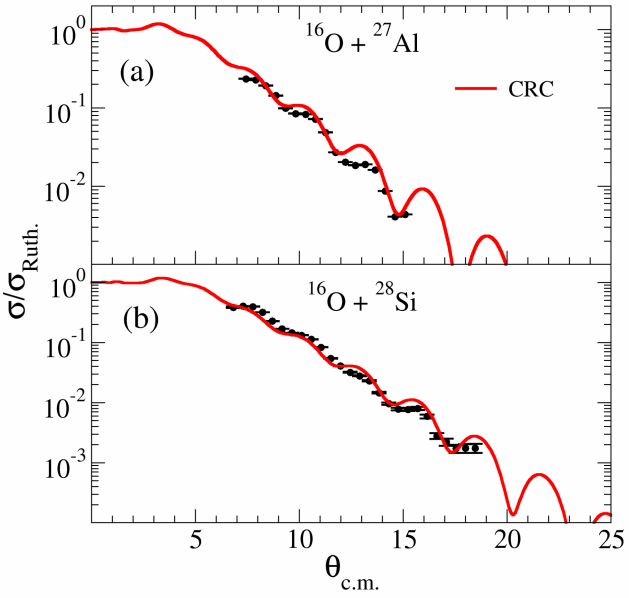

Figure 5.1: Experimental data for the elastic scattering in the ^{27}Al + ^{16}O (panel a) and the ^{28}Si + ^{16}O (panel b) systems. CRC calculations (red line) with the SPP potential and $N_i = 0.6$ for the ^{27}Al + ^{16}O and $N_i = 0.7$ for the ^{28}Si + ^{16}O, with matter diffuseness set to $a_m = 0.62$ fm for both systems. Experimental data from [3]. Figure from [56].

The elastic scattering data is presented in Figure 5.1, in which the red lines are CRC calculations with optimized values for N_r, N_i and a_m. Couplings to inelastic channels were included through the deformation of the optical potential (both real and imaginary terms) in which the nuclear deformation matrix elements for these transitions were calculated from the experimental reduced transition probabilities B(E2). Both B(E2) and nuclear deformation matrix elements values are presented in Table 5.1, and also the coupled excited states for both ^{27}Al and ^{28}Si. This CRC calculation is slightly different from

what is presented in [3], as it includes couplings with transfer channels and the explicit inclusion of channels should affect the elastic channel calculation, as the imaginary part of the optical potential should be reduced in order to reproduce the data.

For consistency, in this dissertation we used the same N_r, N_i, real and imaginary terms, and a_m value as presented in [56], adopting the standard SPP otherwise.

Initial (J^π)	Final (J^π)	B(E2)(e^2fm^4)	β_2	δ_2	*strength*
		^{27}Al states			
0.84 ($1/2^+$)	g.s. ($5/2^+$)	37.8	0.254	0.805	0.882
1.01 ($3/2^+$)	g.s. ($5/2^+$)	37.5	-0.273	-0.867	1.243
2.21 ($7/2^+$)	g.s. ($5/2^+$)	72.2	0.454	1.442	-2.437
2.73 ($5/2^+$)	1.01 ($3/2^+$)	41.9	0.353	-1.121	-1.608
3.00 ($9/2^+$)	g.s. ($5/2^+$)	34.2	0.590	1.875	1.875
		^{28}Si states			
0.00 (0^+)	1.79 (2^+)	326	0.563	1.809	1.809
1.79 (2^+)	4.62 (4^+)	80	0.279	0.896	2.004
1.79 (2^+)	4.98 (0^+)	50	0.220	0.709	1.585

Table 5.1: Deformation parameters for the nuclear potential deformation for the ^{27}Al e ^{28}Si nuclei, for the inelastic channels coupling in this work. First and second columns show the initial and final states considered in the inelastic couplings and its spin-parity J^π. B(E2) are the quadrupole transition probabilities, β_2 are the deformation parameters and δ_2 are the deformation lengths?. The last column, labeled *strength*, presents the values for the nuclear deformation matrix elements. From [57].

5.2 Assessing the nuclear structure models with one-neutron transfers

In our paper submitted to the PRC this year [56], we present an analysis for the ^{27}Al(^{16}O,^{15}O)^{28}Al and ^{28}Si(^{16}O,^{15}O)^{29}Si reactions measured in the same experimental campaign as the results presented in this dissertation. This contribution compares spectroscopic amplitudes, obtained with different shell model interactions for the target-like nuclei, with the experimental data in order to better reproduce them. The results are presented in Figure 5.2, and the regions of interest (ROIs) shown in the figure are detailed in Table 5.2.

In both works, the spectroscopic factors, detailed in Subsection 2.5, were obtained using the NuShellX code [58]. In the one-neutron stripping contribution, the calculations

Table 5.2: Details of the regions of interest adopted in the excitation energy spectra for the target-like ^{28}Al and ^{29}Si nuclei.

residual nucleus	ROI-	Energy range (MeV)	states J^π (MeV)
^{28}Al	1	$[-0.6; +0.5]$	3^+_1 (g.s.), 2^+_1 (0.03)
	2	$[+0.6; +1.7]$	0^+_1 (0.97), 3^+_2 (1.01), 1^+_1 (1.37), 1^+_2 (1.620), 2^+_2 (1.623)
^{29}Si	1	$[-0.6; +0.5]$	$1/2^+_1$ (g.s.)
	2	$[+0.6; +2.6]$	$3/2^+_1$ (1.27), $5/2^+_1$ (2.03), $3/2^+_2$ (2.43)
	3	$[+2.7; +4.2]$	$5/2^+_2$ (3.07), $7/2^-_1$ (3.62), $7/2^+_1$ (4.08)

were performed using the PSDMOD interaction [59] for the ^{15,16}O. And for the ^{27,28}Al and ^{28,29}Si nuclei, three interactions were considered: the PSDMOD interaction, the PSDMWKPN interaction [60–62] and the SPDF-U interaction [63, 64].

Both PSDMOD and PSDMWKPN assumes the same model space: a ^{4}He core with valence nucleons in the $1p_{3/2}$, $1p_{1/2}$, $1d_{5/2}$, $1d_{3/2}$ and $2s_{1/2}$. The SPDF-U interaction assumes a ^{16}O core and $1d_{5/2}$, $1d_{3/2}$, $2s_{1/2}$, $1f_{7/2}$, $1f_{5/2}$, $2p_{3/2}$ and $2p_{1/2}$. Comparison between experimental data and CRC calculations for one-neutrons transfer, Figure 5.2, shows a reasonable good agreement and that the SDPF-U spectroscopic amplitudes give an overall good description, specially in the ROI-3 for the ^{28}Si(^{16}O,^{15}O)^{29}Si (Figure 5.2e).

For the ^{28}Si(^{16}O,^{17}F)^{27}Al, ^{27}Al(^{16}O,^{17}F)^{26}Mg and ^{28}Si(^{16}O,^{18}Ne)^{26}Mg results presented here, we adopted the SDPF-U interaction to maintain a consistent methodology throughout this work. The spectroscopic amplitudes used in the calculations for this work can be found in the Appendix (Table A1.1 and Table A1.2).

The single-particle wave functions were calculated assuming the valence proton bound to a core, represented by an effective binding potential with the Woods-Saxon shape. The depth of this binding potential is changed to reproduce the binding energies for each state. The reduced radius and diffuseness of the binding potential are set to 1.20 fm and 0.60 fm, respectively, to obtain the overlap function between ^{17}F and ^{16}O. These values have been adopted in previous works on transfer reactions induced by heavy ions [25, 26, 65, 66]. For the ^{27}Al and the ^{28}Si target-like nuclei, we are adopting slightly higher values, 1.26 fm and 0.70 fm for the reduced radius and diffuseness, respectively. These values are suitable to describe the transfer cross-section in ^{19}F and ^{29,30}Si [26, 67]. The methodology described and parameter values were also adopted for the one-neutron stripping results.

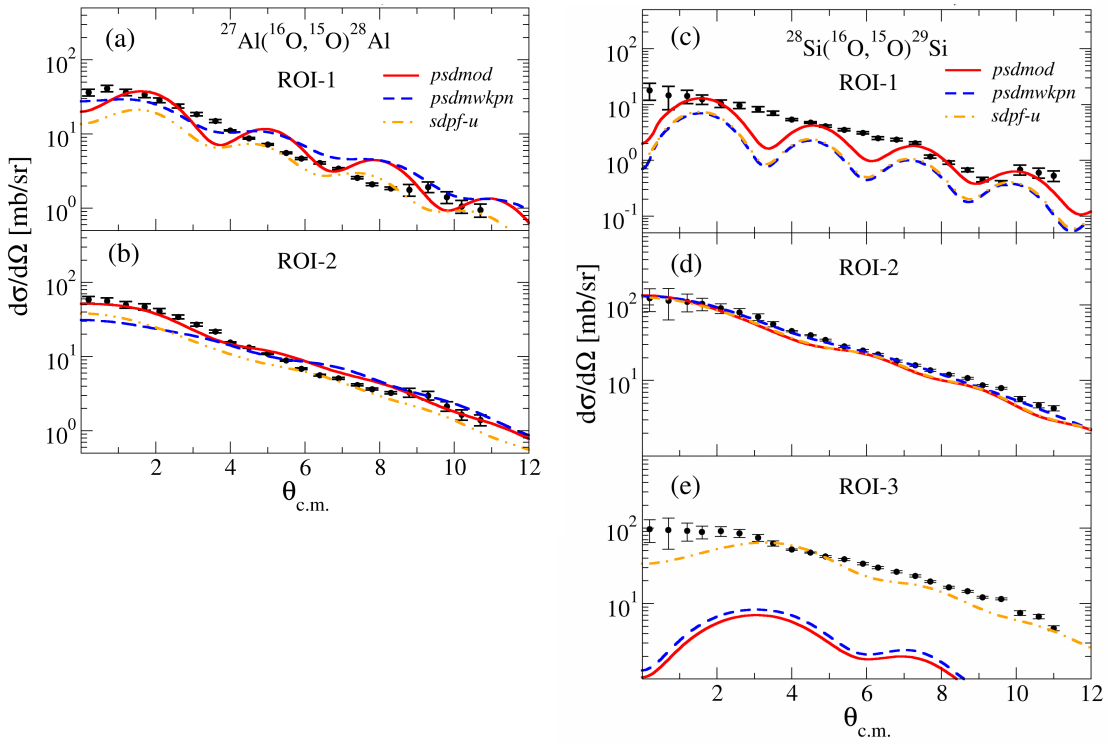

Figure 5.2: Angular distributions for the one-neutron stripping for the ^{27}Al(^{16}O,^{15}O)^{28}Al (left-side) and ^{28}Si(^{16}O,^{15}O)^{29}Si (right-side). For the ^{27}Al(^{16}O,^{15}O)^{28}Al reaction, the ROI-1 is shown in panel (a) left-side and the ROI-2 is shown in panel (b) left-side. For the ^{28}Si(^{16}O,^{15}O)^{29}Si reaction, the ROI-1 is shown in panel (c) right-side, the ROI-2 is shown in panel (d) right-side and the ROI-3 is shown in panel (e) right-side. More details on the Regions Of Interest (ROI) can be found in the text. CRC calculations are presented using spectroscopic factors from PSDMOD (solid red), PSDMWKPN (dashed blue) and SDPF-U (dot-dashed orange) shell model interactions. From [56].

5.3 Regions of interest in the energy spectra

In most cases, the experimental resolution cannot distinguish successive nuclear states. In Figure 5.3, the energy spectra for the one-proton transfer in ^{27}Al (panel a) and ^{28}Si (panel b) and the two-proton transfer in ^{28}Si (panel c). In these spectra, the colored gaussian curves represent individual states of the final nuclei. Orange dotted lines represent both ejectile and recoil nucleus in their ground state, cyan dashed lines represent states of the ejectile nucleus, green dotted lines represent states of the recoil nucleus, purple dashed lines represent states where both ejectile and recoil nuclei are excited. The red solid line represents the sum of states, which reproduce these spectra. Therefore, we obtained the angular distribution cross-sections according to the defined regions of interest (ROIs), detailed in Table 5.3.

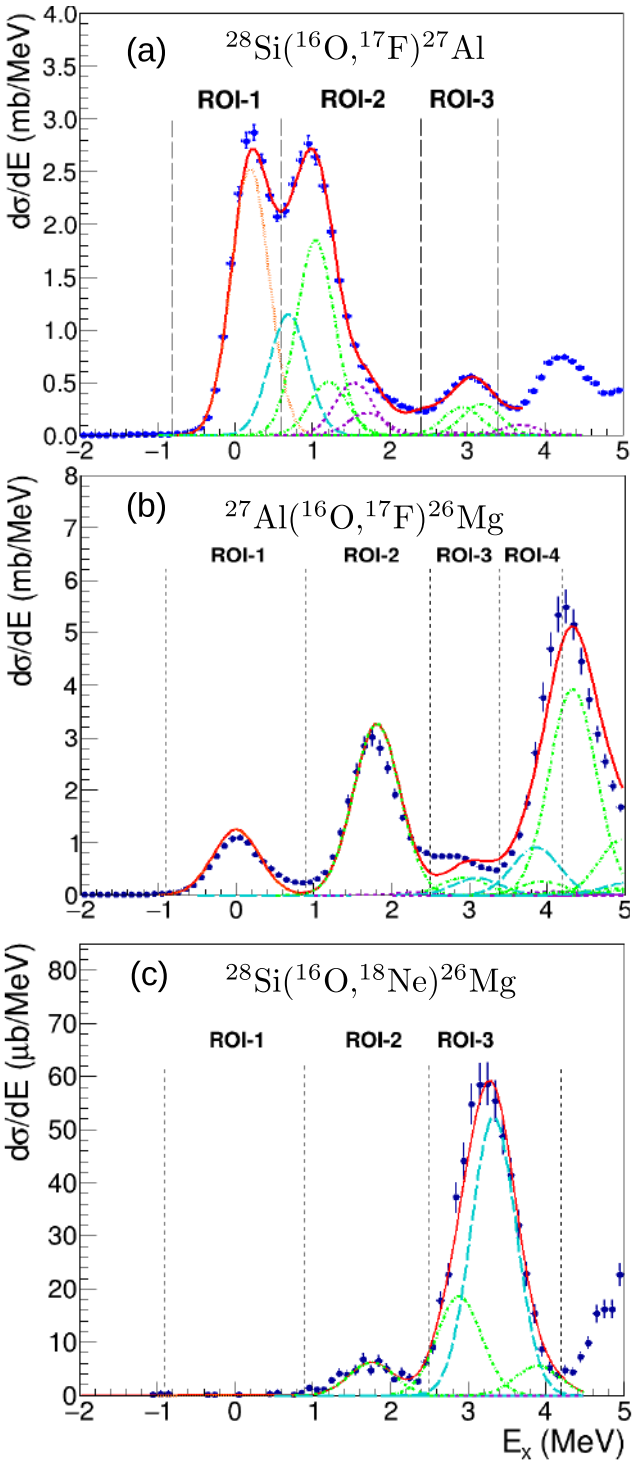

Figure 5.3: Excitation energy spectra for the ^{28}Si(^{16}O,^{17}F)^{27}Al (panel a), ^{27}Al(^{16}O,^{17}F)^{26}Mg (panel b), and ^{28}Si(^{16}O,^{18}Ne)^{26}Mg (panel c) reactions, integrated over $0.0° \leq \theta_{\text{lab}} \leq 4.2°$, $0.0° \leq \theta_{\text{lab}} \leq 4.0°$ and $0.0° \leq \theta_{\text{lab}} \leq 4.2°$, respectively. Colored gaussian curves represent contributions of target-like and projectile-like states, whereas the solid red curves correspond to the sum of such states. The experimental angular distribution cross-sections are determined for each region of interest (ROI) indicated in each spectrum.

Table 5.3: Regions of interest in the 1p-transfer for ^{28}Si and ^{27}Al targets.

residual nucleus	ROI-	Energy range (MeV)	states J^{π} (MeV)
^{27}Al	1	$[-0.7; +0.6]$	$5/2^{+}$ (g.s.)
	2	$]+0.6; +2.4]$	$1/2^{+}$ (0.84); $3/2^{+}$ (1.02); $7/2^{+}$ (2.21);
	3	$]+2.4; +3.4]$	$5/2^{+}$ (2.74); $9/2^{+}$ (3.00);
^{26}Mg	1	$[-0.9; +0.9]$	0^{+} (g.s.);
	2	$]+0.9; +2.5]$	2^{+} (1.81);
	3	$]+2.5; +3.4]$	2^{+} (2.94);
	4	$]+3.4; +4.2]$	0^{+} (3.58); 3^{+} (3.94)

In these regions, the obtained cross-section represents one or more states, in which the most populated ones were included in the calculations coupling scheme. The regions of interest for the two-proton transfer are the same as the one-proton transfer in the ^{16}O + ^{27}Al, since they both lead to the same final nucleus, ^{26}Mg. The third region of interest (ROI-3) in the two-proton transfer is equivalent to the third and fourth regions of the one-proton transfer in the ^{16}O + ^{27}Al, i.e. have an energy range of $]+2.5; +4.2]$ MeV.

5.4 Results for one-proton transfers

Based on our results from the one-neutron transfer reactions, we have adopted the SDPF-U interaction within the shell model to produce relevant spectroscopic factors for the one-proton transfers on ^{28}Si and ^{27}Al. Also, the same binding potential parameters were adopted from the one-neutron stripping analysis [56]. Both contributions used the optical potential parameters obtained in the elastic and inelastic scattering analysis [3].

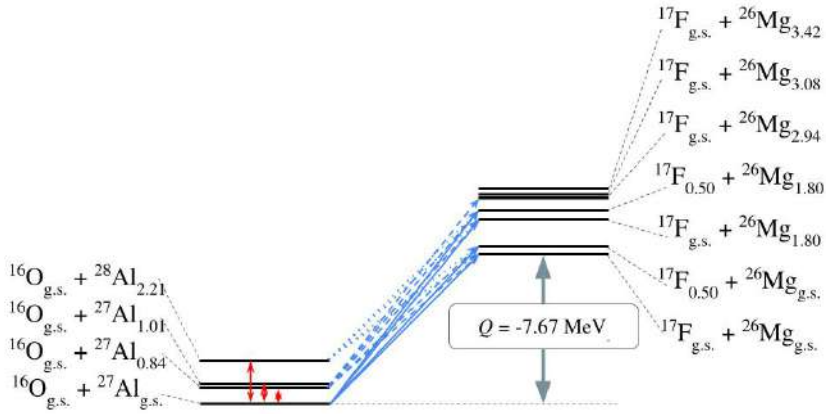

Figure 5.4: Coupling scheme for the CRC calculation performed for the ^{27}Al(^{16}O,^{17}F)^{26}Mg reaction, showing the states included in the entry and exiting partition.

Firstly, we present the results for the one-proton transfer in the $^{16}O + ^{27}Al$ in Figure 5.5. The states considered for the couplings are detailed in Figure 5.4. In general, these calculations reasonably well describe our experimental data, underestimating the cross-sections in the more forward angles. As expected, the calculations that consider the sum of the states included in that region of interest (solid lines) are the best fit for our data for all four regions of interest.

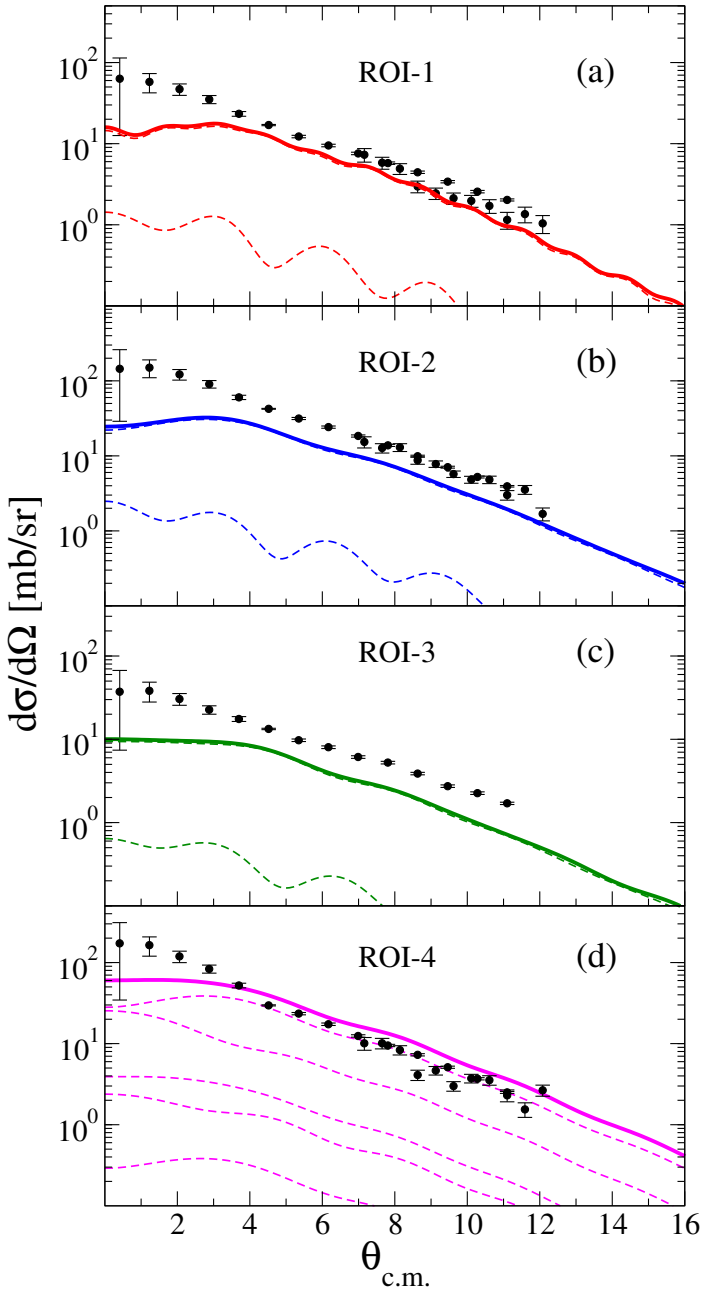

Figure 5.5: Angular distribution cross-sections for the $^{27}Al(^{16}O,^{17}F)^{26}Mg$ reaction compared with CRC calculations (solid lines) summed for the considered coupled states (Figure 5.4). Dashed lines indicate the individual nuclear states contributions.

Secondly, the results for the one-proton transfer in the $^{16}O + ^{28}Si$ in Figure 5.7. The coupling scheme considered for the presented CRC calculations is shown in Figure 5.6. The CRC calculations that consider the sum of the individual states in the regions of interest describe reasonably the angular distributions presented. Though for ROI-1 and ROI-3 the shape description is not the best, the calculations still estimated fairly enough the magnitude of the experimental cross-sections.

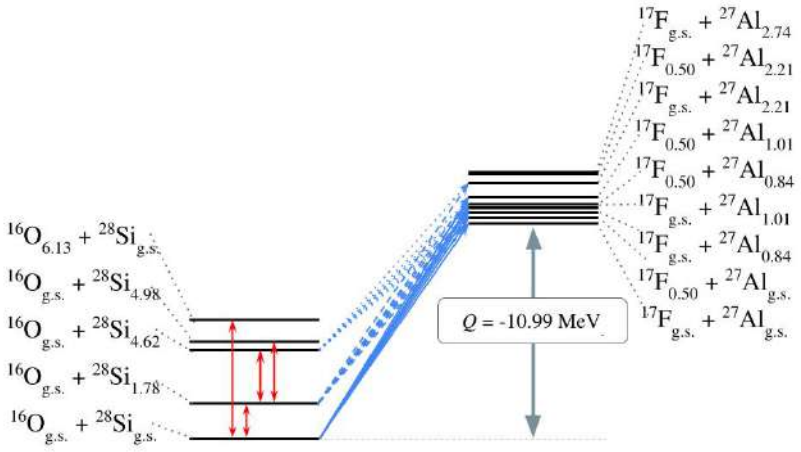

Figure 5.6: Coupling scheme for the CRC calculation performed for the $^{28}Si(^{16}O,^{17}F)^{27}Al$ reaction, showing the states included in the entry and exiting partition.

Since the CRC results for the one-proton transfer in both ^{27}Al and ^{28}Si shows a fairly good description of the experimental data, we can conclude that the consistent methodology adopted works well.

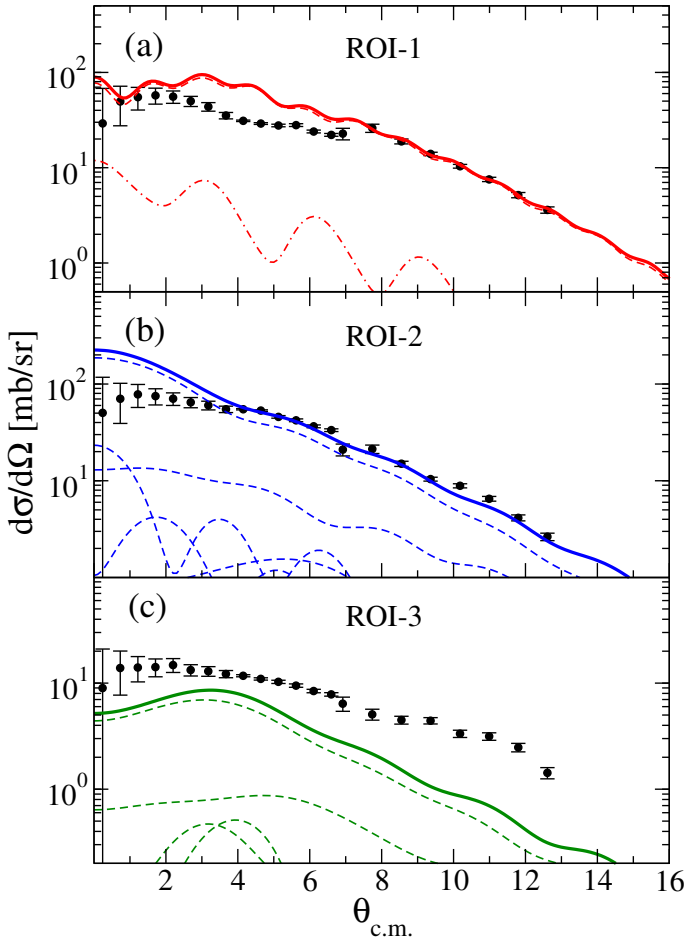

Figure 5.7: Angular distribution cross-sections for the ^{28}Si(^{16}O,^{17}F)^{27}Al reaction compared with CRC calculations (solid lines) summed for the considered coupled states (Figure 5.6). Dashed lines indicate the individual nuclear states contributions.

5.5 The two-proton transfer and the role of pairing

Finally, we present the angular distribution cross-sections for the two-proton transfer in ^{16}O + ^{28}Si system, shown in Figure 5.9. One of the objectives of this analysis is to infer upon the reaction mechanism in which the two-protons are transferred, i.e. the proton are transferred simultaneously or are transferred sequentially, forming ^{27}Al in between the process. For this experimental data, three distinct CRC have been performed in order to allow this discussion.

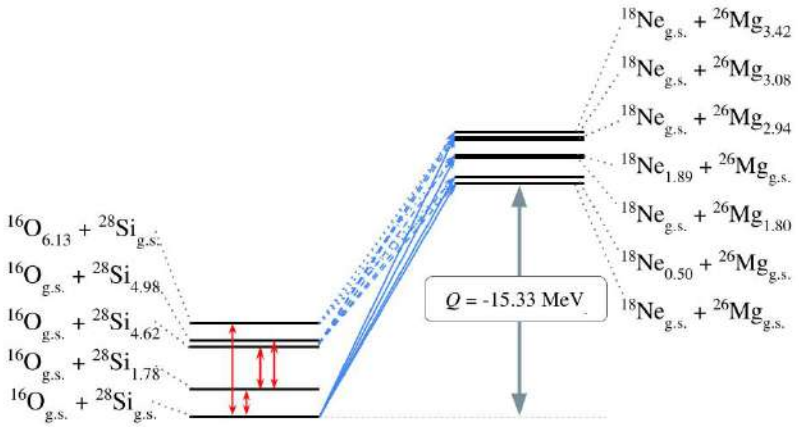

Figure 5.8: Coupling scheme for the CRC calculation performed for the ^{28}Si(^{16}O,^{18}Ne)^{26}Mg reaction, considering a simultaneous transfer mechanism for the two protons, showing the states included in the entry and exiting partition.

The green dotted lines in Figure 5.9 consist of a CRC calculation in which the two-protons are simultaneously transferred, but not as an inert structure and considering relative coordinates between these two transferred protons. This is briefly what the independent coordinates (IC) formalism adopted considers, and more information can be found in [68] and Section 17.3 of [36]. The pink dashed lines consist of a CRC calculation considering the sequential transfer of the two-protons, in which one proton is transferred forming ^{27}Al followed by another proton transfer, forming ^{26}Mg. Although this is a sequential process, the timescale of the reaction does not characterize it as a compound nucleus reaction, and it is treated as a direct process.

The blue solid lines consist of a CRC calculation considering the coherent sum of both sequential and simultaneous processes. This sum can be seen as a new calculation because it considers the interference between the different scattering amplitudes, which is not the same as summing the cross-section values directly.

From the comparison between calculation and experimental results, one can conclude that the ROI-1 (Fig. 5.9 - panel a), which is only the ground-to-ground transfer process, leaves inconclusive which model best reproduces the data. All three models reproduce statistically the experimental cross-sections, leading to the conclusion that both simultaneous and sequential processes are relevant for the description of this region. The second region of interest (Fig. 5.9 - panel b) shows a better agreement between the data and the blue solid line than the other two curves. This indicates that there is a

competition between sequential and simultaneous mechanisms for the two-proton transfer leading to the 1st excited state of ^{26}Mg. Panel c from Fig. 5.9 shows the ROI-3, in which the sequential process (pink dashed line) is heavily suppressed and the simultaneous only process (green dotted line) is the best description for these experimental data. This shows that for states above 3.7 MeV populated by the two-proton transfer are transferred in a simultaneous manner. This indicates that the pairing correlation between the two transferred protons must be relevant for the description of the transfer reaction in this region of interest.

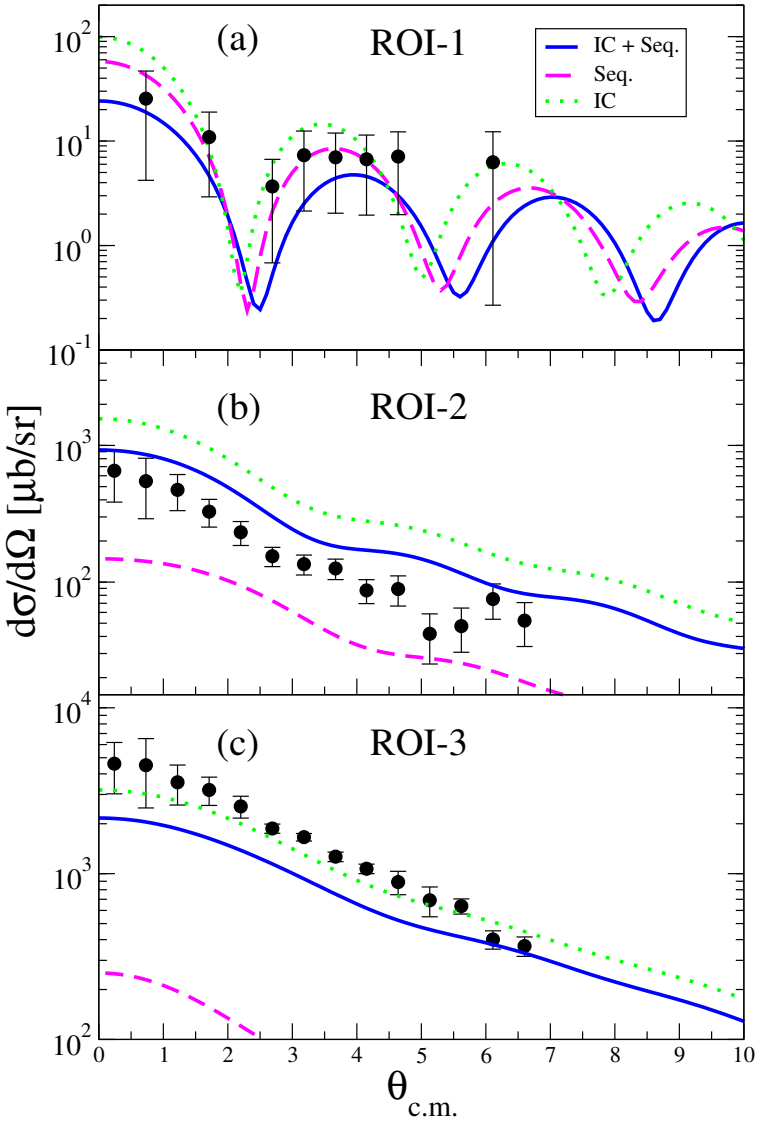

Figure 5.9: Angular distribution cross-sections for the ^{28}Al(^{16}O,^{18}Ne)^{26}Mg reaction compared with CRC calculations. The green dotted line represents the CRC calculations considering the simultaneous transfer of the two-protons, using the independent coordinates (IC) formalism. The pink dashed line stands for the CRC calculations in which the two-protons are transferred sequentially. The blue solid line represents the CRC calculations considering a coherent sum between simultaneous and sequential processes.

6 Conclusion

Atomic nuclei exhibit a rich and fascinating array of properties that shape the physical materials around us. One prominent phenomenon is the phenomenon of pairing, which makes paired nuclei tend to have higher binding energies than would be expected based on a simple sum of the individual nucleon energies. Most experimental evidence has been obtained through measurements of nuclear energy levels, excitation spectra, and nuclear decay patterns.

The origin of pairing lies in the fundamental properties of the nuclear interaction between nucleons. In a first approach, the nucleon-nucleon (nn) interaction is assumed to be isospin independent, in the sense that n-n, p-p, and p-n feel the same pairing strength. However, this aspect of the nn interaction is difficult to assess because of the relevant spin dependence, responsible for the deuteron being the only A=2 nuclear bound system, and the coulomb repulsion in the p-p pair. Two-nucleon transfer reactions are a potential source of information on the pairing interaction. Pairing strength manifests itself in a dominance of simultaneous two-nucleon transfer over the sequential mechanism. The two-neutron transfer has been explored in many reactions induced by light projectiles, such as (t,p) and (p,t), and even heavier projectiles, such as ^{18}O,^{16}O. Very few data are available for two-proton transfer.

In this dissertation, I studied two-proton transfer in ^{28}Si(^{16}O,^{18}Ne)^{26}Mg at E_{lab}=240 MeV. To assess the contribution from the sequential transfer, I also analyzed one-proton transfer in ^{28}Si(^{16}O,^{17}F)^{27}Al and ^{27}Al(^{16}O,^{17}F)^{26}Mg in the same experimental campaign. It is important to highlight that this not only provides important experimental information to set constraints on the direct reaction models but also minimizes systematic uncertainties in the absolute cross sections.

State-of-the-art calculations were performed adopting a consistent methodology to reproduce elastic, inelastic, and one-neutron channels. The parameters of the optical potential and the deformation, necessary to provide the strength of the coupling potentials in coupled-channels, were determined from the analysis of elastic and inelastic scatterings. These parameters were also checked in the analysis of the one-neutron transfer (not presented fully in detail in this dissertation). The one-neutron transfer data have also

been explored to assess the shell model interaction and model space. From this study, we determined that spectroscopic amplitudes from the SPDF-U interaction provide the best result when compared to experimental data.

For the data presented in this dissertation, comparisons of the excitation energy spectra for the one- and two-proton transfer populating the ^{26}Mg residual nucleus show clear differences. The ground state is highly suppressed, whereas states at approximately 3.4 MeV are well populated in the two-proton channel. This is an indication that pairing plays an important role in the two-proton transfer.

Angular distributions for the one-proton transfers are reasonable well reproduced by the coupled-reaction channels calculations. This is a good indication that both nuclear structure and direct reaction models are in place. For the two-proton transfer, three type of reaction calculations have been performed to reproduce the sequential only, the simultaneous only and the sequential + simultaneous mechanisms. The latter takes into account the relative phase between scattering amplitudes obtained from the sequential only and the simultaneous only. Calculation nicely reproduces the experimental data indicating that:

- a competition between sequential and simultaneous transfer for the low-lying states
- a dominance of simultaneous over sequential for states lying around 3.4 MeV.

To summarize, we show that simultaneous transfer of two-proton prevails in heavy-ion reaction and can be explored as a tool to study the fundamental properties of the nn interaction. Howver, further developments in the theory are required to extract the pairing strength from the two-nucleon transfer.

References

1. Cavallaro, M. *et al.* Quantitative analysis of two-neutron correlations in the ^{12}C(^{18}O,^{16}O)^{14}C reaction. *Phys. Rev. C* **88,** 054601 (5 Nov. 2013).
2. Cardozo, E. N. *et al.* Competition between direct and sequential two-neutron transfers in the ^{18}O +^{28} Si collision at 84 MeV. *Phys. Rev. C* **97,** 064611 (6 July 2018).
3. Fonseca, L. *et al.* Elastic and inelastic scattering of ^{16}O on ^{27}Al and ^{28}Si at 240 MeV. *Physical Review C* **100,** 014604 (2019).
4. Erler, J. *et al.* The limits of the nuclear landscape. *Nature* **486,** 509–512 (2012).
5. Epelbaum, E., Hammer, H.-W. & Meißner, U.-G. Modern theory of nuclear forces. *Rev. Mod. Phys.* **81,** 1773–1825. https://link.aps.org/doi/10.1103/RevModPhys.81.1773 (4 Dec. 2009).
6. Machleidt, R. High-precision, charge-dependent Bonn nucleon-nucleon potential. *Phys. Rev. C* **63,** 024001. https://link.aps.org/doi/10.1103/PhysRevC.63.024001 (2 Jan. 2001).
7. Wiringa, R. B., Stoks, V. G. J. & Schiavilla, R. Accurate nucleon-nucleon potential with charge-independence breaking. *Phys. Rev. C* **51,** 38–51. https://link.aps.org/doi/10.1103/PhysRevC.51.38 (1 Jan. 1995).
8. Burgess, C. An Introduction to Effective Field Theory. *Annual Review of Nuclear and Particle Science* **57,** 329–362. eprint: https://doi.org/10.1146/annurev.nucl.56.080805.140508. https://doi.org/10.1146/annurev.nucl.56.080805.140508 (2007).
9. Uhler, H. S. On Moseley's Law for X-Ray Spectra. *Proceedings of the National Academy of Sciences of the United States of America* **3,** 88–90. ISSN: 00278424. http://www.jstor.org/stable/83748 (2023) (1917).
10. Krane, K. S. *Introductory nuclear physics* (John Wiley & Sons, 1991).
11. Cooper, L. N. Bound Electron Pairs in a Degenerate Fermi Gas. *Phys. Rev.* **104,** 1189–1190. https://link.aps.org/doi/10.1103/PhysRev.104.1189 (4 Nov. 1956).
12. Mukhamedzhanov, A. M. & Nunes, F. M. Combined method to extract spectroscopic information. *Phys. Rev. C* **72,** 017602. https://link.aps.org/doi/10.1103/PhysRevC.72.017602 (1 July 2005).

13. Pang, D. Y., Nunes, F. M. & Mukhamedzhanov, A. M. Are spectroscopic factors from transfer reactions consistent with asymptotic normalization coefficients? *Phys. Rev. C* **75,** 024601. https://link.aps.org/doi/10.1103/PhysRevC.75.024601 (2 Feb. 2007).

14. Nunes, F. M., Deltuva, A. & Hong, J. Improved description of ^{34,36,46}Ar(p, d) transfer reactions. *Phys. Rev. C* **83,** 034610. https://link.aps.org/doi/10.1103/PhysRevC.83.034610 (3 Mar. 2011).

15. Gómez-Ramos, M. & Moro, A. M. Interplay of projectile breakup and target excitation in reactions induced by weakly bound nuclei. *Phys. Rev. C* **95,** 034609. https://link.aps.org/doi/10.1103/PhysRevC.95.034609 (3 Mar. 2017).

16. Timofeyuk, N. K. & Johnson, R. C. Nonlocality in Deuteron Stripping Reactions. *Phys. Rev. Lett.* **110,** 112501. https://link.aps.org/doi/10.1103/PhysRevLett.110.112501 (11 Mar. 2013).

17. Tsang, M. B., Lee, J. & Lynch, W. G. Survey of Ground State Neutron Spectroscopic Factors from Li to Cr Isotopes. *Phys. Rev. Lett.* **95,** 222501. https://link.aps.org/doi/10.1103/PhysRevLett.95.222501 (22 Nov. 2005).

18. Timofeyuk, N. & Johnson, R. Theory of deuteron stripping and pick-up reactions for nuclear structure studies. *Progress in Particle and Nuclear Physics* **111,** 103738. ISSN: 0146-6410. https://www.sciencedirect.com/science/article/pii/S0146641019300730 (2020).

19. Zhukov, M. *et al.* Bound state properties of Borromean halo nuclei: ^{6}He and ^{11}Li. *Physics Reports* **231,** 151–199. ISSN: 0370-1573. https://www.sciencedirect.com/science/article/pii/037015739390141Y (1993).

20. Hagino, K., Takahashi, N. & Sagawa, H. Strong dineutron correlation in ^{8}He and ^{18}C. *Phys. Rev. C* **77,** 054317. https://link.aps.org/doi/10.1103/PhysRevC.77.054317 (5 May 2008).

21. Duer, M. *et al.* Observation of a correlated free four-neutron system. *Nature* **606,** 678–682. https://www.nature.com/articles/s41586-022-04827-6 (2022).

22. Von Oertzen, W. & Vitturi, A. Pairing correlations of nucleons and multi-nucleon transfer between heavy nuclei. *Reports on Progress in Physics* **64,** 1247. https://dx.doi.org/10.1088/0034-4885/64/10/202 (Sept. 2001).

23. Hagino, K. & Scamps, G. Enhancement factor for two-neutron transfer reactions with a schematic coupled-channels model. *Phys. Rev. C* **92,** 064602. https://link.aps.org/doi/10.1103/PhysRevC.92.064602 (6 Dec. 2015).
24. Potel, G., Idini, A., Barranco, F., Vigezzi, E. & Broglia, R. A. Cooper pair transfer in nuclei. *Reports on Progress in Physics* **76,** 106301. https://dx.doi.org/10.1088/0034-4885/76/10/106301 (Oct. 2013).
25. Linares, R. *et al.* Analysis of the one-neutron transfer to ^{16}O, ^{28}Si, and ^{64}Ni induced by the (^{18}O, ^{17}O) reaction at 84 MeV. *Physical Review C* **98,** 054615 (2018).
26. Sgouros, O. *et al.* One-proton transfer reaction for the ^{18}O + ^{48}Ti system at 275 MeV. *Physical Review C* **104,** 034617 (2021).
27. Calabrese, S. *et al.* ^{18}O-induced single-nucleon transfer reactions on ^{40}Ca at 15.3 A MeV within a multichannel analysis. *Physical Review C* **104,** 064609 (2021).
28. Carbone, D. *et al.* Analysis of two-nucleon transfer reactions in the ^{20}Ne + ^{116}Cd system at 306 MeV. *Physical Review C* **102,** 044606 (2020).
29. Ferreira, J. *et al.* Analysis of two-proton transfer in the ^{40}Ca (^{18}O, ^{20}Ne) ^{38}Ar reaction at 270 MeV incident energy. *Physical Review C* **103,** 054604 (2021).
30. Fonseca, L. M. *et al.* Elastic and inelastic scattering of ^{16}O on ^{27}Al and ^{28}Si at 240 MeV. *Phys. Rev. C* **100,** 014604 (1 July 2019).
31. Brink, D. Kinematical effects in heavy-ion reactions. *Physics Letters B* **40,** 37–40. ISSN: 0370-2693 (1972).
32. Fröbrich, P. & Lipperheide, R. *Theory of nuclear reactions* (Courier Corporation, 1996).
33. Gottfried, K. & Yan, T.-M. *Quantum mechanics: fundamentals* (Springer Science & Business Media, 2013).
34. Titus, L. J. & Nunes, F. M. Testing the Perey effect. *Phys. Rev. C* **89,** 034609. https://link.aps.org/doi/10.1103/PhysRevC.89.034609 (3 Mar. 2014).
35. Chamon, L. C. *et al.* Toward a global description of the nucleus-nucleus interaction. *Phys. Rev. C* **66,** 014610. https://link.aps.org/doi/10.1103/PhysRevC.66.014610 (1 July 2002).
36. Satchler, G. & Satchler, G. *Direct Nuclear Reactions* ISBN: 9780198512691 (Clarendon Press, 1983).
37. Linares, R. Internal Communication. June 29, 2023.

38. Thompson, I. J. *Comput. Phys. Rep.* **7,** 167 (1988).

39. Alvarez, M. *et al.* A parameter-free optical potential for the heavy-ion elastic scattering process. *Nuclear Physics A* **723,** 93–103. ISSN: 0375-9474. http://www.sciencedirect.com/science/article/pii/S0375947403011588 (2003).

40. Rifuggiato, D. *et al.* Operational experience with the Excyt facility. *Proc. HIAT09,* 5 (2009).

41. *MAGNEX Spectrometer* (accessed in Nov, 2022) (). https://web.infn.it/NUMEN/index.php/it/experiment/the-experiment-2.

42. Cappuzzello, F., Agodi, C., Carbone, D. & Cavallaro, M. The MAGNEX spectrometer: Results and perspectives. *The European Physical Journal A* **52,** 1–44 (2016).

43. Carbone, D. First experimental evidence of the Giant Pairing Vibration in atomic nuclei (2013).

44. Berz, M., Makino, K. & INFINITY, C. Department of Physics and Astronomy and NSCL. *Michigan State University, East Lansing, USA* (2001).

45. Makino, K. & Berz, M. COSY INFINITY Version 9. *Nuclear Instruments and Methods in Physics Research Section A: Accelerators, Spectrometers, Detectors and Associated Equipment* **558.** Proceedings of the 8th International Computational Accelerator Physics Conference, 346–350. ISSN: 0168-9002. https://www.sciencedirect.com/science/article/pii/S0168900205021522 (2006).

46. Leo, W. R. *Techniques for nuclear and particle physics experiments: a how-to approach* (Springer Science & Business Media, 2012).

47. Cappuzzello, F. *et al.* A particle identification technique for large acceptance spectrometers. *Nuclear Instruments and Methods in Physics Research Section A: Accelerators, Spectrometers, Detectors and Associated Equipment* **621,** 419–423 (2010).

48. Cunsolo, A. *et al.* Ion optics for large-acceptance magnetic spectrometers: application to the MAGNEX spectrometer. *Nuclear Instruments and Methods in Physics Research Section A: Accelerators, Spectrometers, Detectors and Associated Equipment* **484,** 56–83 (2002).

49. Cappuzzello, F., Carbone, D., Cavallaro, M. & Cunsolo, A. MAGNEX: an innovative large acceptance spectrometer for nuclear reaction studies in: Magnets: Types, Uses and Safety. *Nova, New York,* 1–63 (2011).
50. Berz, M. *Modern map methods in particle beam physics* (Academic Press, 1999).
51. Lazzaro, A. *The large acceptance and high resolution ray-tracing magnetic spectrometer MAGNEX* PhD thesis (Ph. D. Thesis, University of Catania, 2002).
52. Catford, W. *Catkin - The kinematics programme in Excel* (). http://personal.ph.surrey.ac.uk/~phs1wc/kinematics/.
53. Ziegler, J., Biersack, J. & Littmark, U. The stopping and ranges of ions in solids, Vol. 1. *The Stopping and Ranges of Ions in Matter* (1985).
54. Cavallaro, M. *et al.* Transport efficiency in large acceptance spectrometers. *Nuclear Instruments and Methods in Physics Research Section A: Accelerators, Spectrometers, Detectors and Associated Equipment* **637,** 77–87 (2011).
55. NNDC & BNL. *Nudat 3 - Interactive Chart of Nuclides and Nuclear Structure and Decay Search* https://www.nndc.bnl.gov/nudat3 [Accessed: 2023-06-12].
56. Linares, R. *et al.* One-neutron transfer from ^{16}O to ^{27}Al and ^{28}Si targets at $E_{\mathrm{lab}} = 240\,\mathrm{MeV}$. *Phys. Rev. C* **108,** 014619. https://link.aps.org/doi/10.1103/PhysRevC.108.014619 (1 July 2023).
57. Fonseca, L. M. d. *Influências de deformação nuclear no espalhamento de ^{16}O por ^{27}Al e ^{28}Si a Elab. = 240 MeV* Tese (Doutorado em Física) (Universidade Federal Fluminense, Niterói-RJ, 2021).
58. Rae, W. D. M. *http://www.garsington.eclipse.co.uk.* http://www.garsington.eclipse.co.uk (2008).
59. Utsuno, Y. & Chiba, S. *Phys. Rev. C* **83,** 021301 (2011).
60. Wildenthal, B. Empirical strengths of spin operators in nuclei. *Progress in Particle and Nuclear Physics* **11,** 5–51. ISSN: 0146-6410. http://www.sciencedirect.com/science/article/pii/0146641084900115 (1984).
61. Millener, D. & Kurath, D. The particle-hole interaction and the beta decay of ^{14}B. *Nuclear Physics A* **255,** 315–338. ISSN: 0375-9474. http://www.sciencedirect.com/science/article/pii/0375947475906831 (1975).

62. Cohen, S. & Kurath, D. Effective interactions for the 1p shell. *Nuclear Physics* **73,** 1–24. ISSN: 0029-5582. http://www.sciencedirect.com/science/article/pii/0029558265901483 (1965).

63. Nummela, S. *et al.* Spectroscopy of ^{34,35}Si by β decay: $sd-fp$ shell gap and single-particle states. *Phys. Rev. C* **63,** 044316. https://link.aps.org/doi/10.1103/PhysRevC.63.044316 (4 Mar. 2001).

64. Nowacki, F. & Poves, A. New effective interaction for $0\hbar\omega$ shell-model calculations in the $sd-pf$ valence space. *Phys. Rev. C* **79,** 014310. https://link.aps.org/doi/10.1103/PhysRevC.79.014310 (1 Jan. 2009).

65. Linares, R. *et al.* Investigation of the one-neutron transfer in ^{13}C$+^{28}$Si at $E_{\mathrm{lab}} = 30$ and 34 MeV. *Phys. Rev. C* **101,** 014611. https://link.aps.org/doi/10.1103/PhysRevC.101.014611 (1 Jan. 2020).

66. Ciraldo, I. *et al.* Analysis of the one-neutron transfer reaction in ^{18}O$+^{76}$Se collisions at 275 MeV. *Phys. Rev. C* **105,** 044607. https://link.aps.org/doi/10.1103/PhysRevC.105.044607 (4 Apr. 2022).

67. Cardozo, E. N. *et al.* Competition between direct and sequential two-neutron transfers in the ^{18}O $+^{28}$ Si collision at 84 MeV. *Phys. Rev. C* **97,** 064611. https://link.aps.org/doi/10.1103/PhysRevC.97.064611 (6 June 2018).

68. Thompson, I. J. Coupled reaction channels calculations in nuclear physics. *Computer Physics Reports* **7,** 167–212 (1988).

Appendix

A1 Spectroscopic amplitude tables

26Mg nucleus		27Al nucleus			Spec. Ampl. S
state (MeV)	J^π	state (MeV)	J^π	$n\ell_j$	SDPF-U
g.s.	0^+	g.s.	$5/2^+$	$1d_{5/2}$	-0.511
		0.84	$1/2^+$	$2s_{1/2}$	-0.619
		1.01	$3/2^+$	$1d_{3/2}$	-0.203
		2.74	$5/2^+$	$1d_{5/2}$	0.107
1.81	2^+	g.s.	$5/2^+$	$2s_{1/2}$	-0.110
		g.s.	$5/2^+$	$1d_{3/2}$	0.000
		g.s.	$5/2^+$	$1d_{5/2}$	0.827
		0.84	$1/2^+$	$1d_{3/2}$	-0.123
		0.84	$1/2^+$	$1d_{5/2}$	0.261
		1.01	$3/2^+$	$2s_{1/2}$	0.527
		1.01	$3/2^+$	$1d_{3/2}$	-0.106
		1.01	$3/2^+$	$1d_{5/2}$	-0.232
		2.21	$7/2^+$	$1d_{3/2}$	0.088
		2.21	$7/2^+$	$1d_{5/2}$	-0.499
		2.74	$5/2^+$	$2s_{1/2}$	-0.513
		2.74	$5/2^+$	$1d_{3/2}$	-0.330
		2.74	$5/2^+$	$1d_{5/2}$	0.229
2.94	2^+	g.s.	$5/2^+$	$2s_{1/2}$	-0.189
		g.s.	$5/2^+$	$1d_{3/2}$	0.184
		g.s.	$5/2^+$	$1d_{5/2}$	-0.355
		0.84	$1/2^+$	$1d_{3/2}$	0.385
		0.84	$1/2^+$	$1d_{5/2}$	-0.526
		1.01	$3/2^+$	$2s_{1/2}$	-0.367
		1.01	$3/2^+$	$1d_{3/2}$	-0.189
		1.01	$3/2^+$	$1d_{5/2}$	-0.641
		2.21	$7/2^+$	$1d_{3/2}$	0.181
		2.21	$7/2^+$	$1d_{5/2}$	-0.064
		2.74	$5/2^+$	$2s_{1/2}$	-0.063
		2.74	$5/2^+$	$1d_{3/2}$	-0.046
		2.74	$5/2^+$	$1d_{5/2}$	-0.070
3.59	0^+	g.s.	$5/2^+$	$1d_{5/2}$	0.089
		0.84	$1/2^+$	$2s_{1/2}$	0.252
		1.01	$3/2^+$	$1d_{3/2}$	0.040
		2.74	$5/2^+$	$1d_{5/2}$	0.033
3.94	3^+	g.s.	$5/2^+$	$2s_{1/2}$	-0.094
		g.s.	$5/2^+$	$1d_{3/2}$	0.164
		g.s.	$5/2^+$	$1d_{3/2}$	-0.030

26Mg nucleus		27Al nucleus			Spec. Ampl. S
state (MeV)	J^π	state (MeV)	J^π	$n\ell_j$	SDPF-U
		0.84	$1/2^+$	$1d_{5/2}$	0.226
		1.01	$3/2^+$	$1d_{3/2}$	-0.024
		1.01	$3/2^+$	$1d_{5/2}$	0.059
		2.21	$7/2^+$	$2s_{1/2}$	-0.150
		2.21	$7/2^+$	$1d_{3/2}$	0.113
		2.21	$7/2^+$	$1d_{5/2}$	-0.046
		2.74	$5/2^+$	$2s_{1/2}$	0.083
		2.74	$5/2^+$	$1d_{3/2}$	0.028
		2.74	$5/2^+$	$1d_{5/2}$	0.067
4.32	4^+	g.s.	$5/2^+$	$1d_{3/2}$	0.145
		g.s.	$5/2^+$	$1d_{5/2}$	0.984
		1.01	$3/2^+$	$1d_{5/2}$	0.229
		2.21	$7/2^+$	$2s_{1/2}$	0.591
		2.21	$7/2^+$	$1d_{3/2}$	0.062
		2.21	$7/2^+$	$1d_{5/2}$	-0.545
		2.74	$5/2^+$	$1d_{3/2}$	0.141
		2.74	$5/2^+$	$1d_{5/2}$	-0.142
4.33	2^+	g.s.	$5/2^+$	$2s_{1/2}$	-0.097
		g.s.	$5/2^+$	$1d_{3/2}$	-0.041
		g.s.	$5/2^+$	$1d_{3/2}$	0.280
		0.84	$1/2^+$	$1d_{3/2}$	-0.189
		0.84	$1/2^+$	$1d_{5/2}$	-0.115
		1.01	$3/2^+$	$2s_{1/2}$	0.219
		1.01	$3/2^+$	$1d_{3/2}$	-0.004
		1.01	$3/2^+$	$1d_{5/2}$	0.045
		2.21	$7/2^+$	$1d_{3/2}$	-0.020
		2.21	$7/2^+$	$1d_{5/2}$	-0.006
		2.74	$5/2^+$	$2s_{1/2}$	-0.063
		2.74	$5/2^+$	$1d_{3/2}$	-0.160
		2.74	$5/2^+$	$1d_{5/2}$	0.033
4.35	3^+	g.s.	$5/2^+$	$2s_{1/2}$	-0.287
		g.s.	$5/2^+$	$1d_{3/2}$	0.198
		g.s.	$5/2^+$	$1d_{5/2}$	-0.086
		0.84	$1/2^+$	$1d_{5/2}$	0.665
		1.01	$3/2^+$	$1d_{3/2}$	0.169
		1.01	$3/2^+$	$1d_{5/2}$	0.524
		2.21	$7/2^+$	$2s_{1/2}$	0.237
		2.21	$7/2^+$	$1d_{3/2}$	0.055
		2.21	$7/2^+$	$1d_{5/2}$	0.217

Table A1.1: Spectroscopic amplitudes adopted for the ^{26}Mg and ^{27}Al.

27Al nucleus		28Si nucleus			Spec. Ampl. S
state (MeV)	J^π	state (MeV)	J^π	$n\ell_j$	SDPF-U
g.s.	$5/2^+$	g.s.	0^+	$1d_{5/2}$	1.781
		1.78	2^+	$2s_{1/2}$	0.624
		1.78	2^+	$1d_{3/2}$	0.323
		1.78	2^+	$1d_{5/2}$	-0.174
		4.62	4^+	$1d_{3/2}$	-0.445
		4.62	4^+	$1d_{5/2}$	0.048
0.84	$1/2^+$	g.s.	0^+	$2s_{1/2}$	-0.901
		1.78	2^+	$1d_{3/2}$	-0.192
		1.78	2^+	$1d_{5/2}$	-0.445
		4.98	0^+	$2s_{1/2}$	0.563
1.01	$3/2^+$	g.s.	0^+	$1d_{3/2}$	0.644
		1.78	2^+	$2s_{1/2}$	0.202
		1.78	2^+	$1d_{3/2}$	0.443
		1.78	2^+	$1d_{5/2}$	-0.749
		4.62	4^+	$1d_{5/2}$	0.112
2.21	$7/2^+$	1.78	2^+	$1d_{3/2}$	-0.264
		1.78	2^+	$1d_{5/2}$	-1.030
		4.62	4^+	$2s_{1/2}$	0.244
		4.62	4^+	$1d_{3/2}$	0.490
		4.62	4^+	$1d_{5/2}$	-0.149
2.74	$5/2^+$	g.s.	0^+	$1d_{5/2}$	-0.627
		1.78	2^+	$2s_{1/2}$	0.473
		1.78	2^+	$1d_{3/2}$	-0.418
		1.78	2^+	$1d_{5/2}$	-0.639
		4.62	4^+	$1d_{3/2}$	-0.013
		4.62	4^+	$1d_{3/2}$	-0.445
		4.98	0^+	$1d_{5/2}$	0.343
3.00	$9/2^+$	1.78	2^+	$1d_{5/2}$	-0.867
		4.62	4^+	$2s_{1/2}$	0.595
		4.62	4^+	$1d_{3/2}$	0.284
		4.62	4^+	$1d_{5/2}$	0.002

Table A1.2: Spectroscopic amplitudes adopted for the ^{27}Al and ^{28}Si.